Proton Compton Scattering
With Polarized γ Rays

by

Xi-jun Zhao

Dissertation submitted to the Faculty of the
Virginia Polytechnic Institute and State University
in partial fulfillment of the requirements for the degree of
DOCTOR OF PHILOSOPHY
in
Physics

APPROVED:

Marvin Blecher
Marvin Blecher, Chairman

Andrew Sandorfi
Andrew Sandorfi

D. Roper
David Roper

Leo Piilonen
Leo Piilonen

Lay Nam Chang
Lay Nam Chang

John R. Ficenec
John R. Ficenec

December, 1993
Blacksburg, Virginia

Proton Compton Scattering

With Polarized γ Rays

by

Xi-jun Zhao

Committee Chairman: Marvin Blecher

Physics

(ABSTRACT)

Proton Compton scattering has been studied from 220 to 330 MeV at 90 degree center of mass scattering angle with the polarized photon beam at LEGS. Compton scattering is an important probe of the nucleon structure and its excited states. Polarization degrees of freedom reveal more information than unpolarized observables. This experiment measured, for the first time, the polarized cross sections of proton Compton scattering up to the Δ resonance. The parallel and perpendicular cross sections were measured at the same time. All the photons were tagged so that the energy dependent systematic errors are small. The measured unpolarized cross section is above the lower bound from unitary at all energies. The cross section asymmetry is obtained as a function of energy for the first time. The unpolarized cross section is compared with previous data and with calculations from the fixed-t dispersion model, the isobar model and the finite energy dispersion model. Although all these calculations agree fairly well with unpolarized cross section data, the photon asymmetry data show that the isobar model contains serious defects. The ratio of polarized cross sections, $\frac{d\sigma_{\parallel}}{d\sigma_{\perp}}$, is compared with a model independent result. The results from the present experiment can be used in the calculation of the $E2/M1$ ratio in the $N-\Delta$ transition, which is an important signature of the tensor interaction between quarks.

Acknowledgements

First, I would like to thank my advisor, Dr. Marvin Blecher, for his constant support and encouragement throughout my graduate career. I am grateful to him for introducing me to the field of experimental physics and his much help through the years.

I have benefited tremendously from my work at the LEGS group where I gained many skills in all experimental aspects, including software and hardware. I am fortunate to work with the friendly and helpful people at LEGS, whose team work resulted in the successful completion of this important experiment on which my thesis is based. Special thanks to Dr. Andy Sandorfi for his help and much advice throughout the years. He is always available for help although he often has a busy schedule. I am grateful to Dr. Craig Thorn for his help and patient explanations of many difficult experimental aspects to me. Thanks to Dr. Ott Kistner for his help, and especially the troubles in providing me many nice graphs in my thesis. I would like to thanks Dr. Sam Hoblit, Dr. Mahbub Khandaker, and Dr. April Tam for their much help and suggestions in the data analysis, from whom I learned many computational skills. I also appreciate the help from Lino Miceli about the laser. My thanks to Tony Kuczewski, Tony Caracappa and Frank Linchln for their help when I was working in the electronic and machine shop.

I would like to thank my graduation committee members, Dr. Marvin Blecher, Dr. Andy Sandorfi, Dr. David Roper, Dr. Leo Piilonen, Dr. John R. Ficenec and Dr. Lay Nam Chang for their careful reviewing of my thesis and their many good suggestions. My thanks to Ms.

Chris Thomas of the Physics Department, Virginia Tech. She provided me with much good advice concerning international students and excellent service.

Special thanks to Dr. Steve Whisnant for his much help to me when I first came to BNL. At my beginning year at LEGS, I also enjoyed to to be with the people from RPI, Dr. Kameron Vaziri, and the fellow graduate students Dave Tedeski, Chris Ruth, Bill Clayton, and Keith Mize from University of South Carolina. I appreciate their help to me.

I am also fortunate to work with Dr. Dominique Rebreyend from France, with whom I enjoyed many interesting discussions, and Dr. Hans Stroeher from Germany. I appreciated the help and encouragement from them.

I will always be in debt to my loving parents, who have sacrificed so much and done whatever they could to support me throughout my studies and my life. Special thanks to Parke and Jan Rohrer, whose kindness made me feel at home when staying at BNL.

Finally, I would like to dedicate this work to my dear wife, Wei Li, whose love and help have given me strength in my work and happiness in my life.

Contents

List of Figures

List of Tables

Chapter 1

Introduction

1.1 The Quest for Knowledge

One distinctive characteristic of human beings is the desire and ability to discover and understand the world around them. For thousands of years, people had wondered why the world is so colorful and diverse, about what this wonderful world is made up of. Although there were many attempts in the course of history to answer this question, it was not until the last century that people found the world is made of atoms and molecules. This great discovery began a new era in man's understanding of nature and opened up a totally new microscopic world.

Later the enormous variety of molecules were found to be composed of only about one hundred elements. After Mendeleev discovered regularity in the elements, people found that even 'atoms' had a substructure. After much effort early in this century, atoms were found to consist of electrons and a nucleus, which in turn was found to consist of protons and neutrons. These discoveries brought people to a new frontier — the subatomic world. Many have probed this new world. For over half a century many tools for experimentation such as sophisticated accelerators and detectors, have been built. New particles and unexpected

phenomena were discovered. Theories to explain the microscopic world were proposed, tested, discarded or refined .

Today, we already have good understanding in many fields of the microscopic world. People can 'design' and 'manufacture' specific molecules to meet their needs. The atomic world has been well explored and quantum mechanics explains almost all the phenomena there. In one of the sub-atomic worlds, particle physics, people discovered some regularity in the many particles discovered, just like the case in elements. To explain this regularity the Quark Model was proposed, according to which all the hadrons, like the proton and neutron, are composed of quarks. After much effort, a theory called Quantum Chromodynamics(QCD) were constructed to describe the interactions between quarks [1]. It has been quite successful in describing the phenomena in the high energy kingdom. A wave of discoveries has followed this theory and supported and enriched it. In recent years, the Standard Model(SM), based on QCD and electroweak unification, can explain almost all phenomena in particle physics [2].

1.2 The Unique Role of the Proton

1.2.1 The difficulty facing nuclear physics

In the past few decades, while particle physics advanced with amazing pace, nuclear physics lagged behind in constructing a consistent theoretical framework. QCD cannot be used in nuclear physics, since the main calculation scheme in QCD is based on perturbation theory. Calculations become practical only when the coupling constant, or the interaction strength, is small and high order terms in the expansion can be neglected. The coupling constant between quarks decreases as the interaction distance between quarks decreases [1]. This phenomenon, called 'Asymptotic Freedom', makes the SM and QCD very successful in explaining and predicting phenomena with small interaction distance between quarks or with high momentum transfer.

But in the realm of nuclear physics the situation is different. There 'asymptotic freedom' is no longer valid. The interaction energy between particles is not as high and the coupling constant is large, and thus the perturbation method in QCD is not useful. Although some phenomenological models have been proposed which are very successful in explaining some types of reactions and nuclear structure, the situation is not as good as in particle physics.

1.2.2 The unique role of the proton

The proton is one of the basic building blocks of the world, indispensible in building up every atom. In broadening our knowledge and bridging the gap between nuclear and particle physics the proton plays a unique role. It is the lightest baryon, as well as the smallest nucleus.

The proton, composed of three quarks, is the simplest stable object made up of quarks. It has spin $\frac{1}{2}$, isospin $\frac{1}{2}$ and positive parity. In quantum theory the proton can be completely described by its wave function. To determine the wave function the interaction between quarks is needed. So far we still do not know the wavefunction completely. Previously, the proton was described as a spherical object, but recently it is believed that there is a D-wave component in it. The interaction between quarks is not well known in the low-energy range, although at high energy it is very well known. The study of proton structure may help to expand our knowledge of the $q - q$ interaction from the high energy to the intermediate and low energy domain.

At present, in order to quantitatively describe the proton, one developes models with assumptions about the $q - q$ interaction. There are many models available[3], such as the MIT bag model, constituent quark model, chiral bag model, skyrmion model, etc. Each model is successful in explaining only some of the proton properties. The experiment of proton Compton scattering can help unravel more about the $q - q$ interaction at low energy and the wave function of proton, especially the small D2 component. From the comparison of

our results with theoretical predictions we can decide which model is closer to reality. Since the proton is a building block of the nucleus, understanding the proton is an important step to the understanding of more complicated nuclei.

1.2.3 Ways to probe the proton with photons

In experiments with deuterium a quadrupole moment is measured, which implies a D-wave component in the deuterium wavefunction. However, unlike deuterium, the quadrupole and higher moments of the proton are zero. Even if the proton has a D-wave component, it will not result in a quadrupole moment and thus can not be experimentally measured. This can be easily seen from the Wigner-Eckart theorem[4]:

$$< \alpha', j'm'|T_q^{(k)}|\alpha, jm >=< jk; mq|jk; j'm' > \frac{< \alpha' j'||T^{(k)}||\alpha j >}{\sqrt{2j+1}} \qquad (1.1)$$

where j and m are the usual angular momentum quantum number and its projection, and α denotes all other quantum numbers for the initial system. The primed symbols are for the final system. $T_q^{(k)}$ is the qth component of a tensor of rank k, which describes an interaction. For dipole and quadrupole moments, $T_q^{(k)}$ is a tensor of rank 1 or 2, *i.e.* $k = 1$ and $k = 2$, respectively. The first term on the right hand side is a Clebsch-Gordan (C-G) coefficient for adding j and k to get j'. Since $j' = j = \frac{1}{2}$, k has to be 0 or 1 for a non-vanishing C-G coefficient. This means the highest non-vanishing moment is the dipole moment. For higher moments, even if the reduced matrix elements in Equation 1.1 are not zero, the C-G coefficients will make the moments to be zero.

However, the nucleon has excited states. The Δ, being the first exited state of nucleon, can be studied through the $N - \Delta$ transition. The Δ has spin $\frac{3}{2}$ and, from the Wigner-Eckart theorem, the transition matrix is non-vanishing. The transition amplitude can be expanded in terms of multipole amplitudes. From conservation of angular momentum the only allowed photon angular momenta are 1 or 2. Both the proton and Δ have positive

parity. From parity conservation only the M1 and E2 transitions are allowed, since both of them have positive parity.

At LEGS three reactions can be used to induce $N - \Delta$ transitions with photons:

- π^+ photoproduction: $\gamma + p \longrightarrow \pi^+ + n$
- π^0 photoproduction: $\gamma + p \longrightarrow \pi^0 + p$
- proton Compton scattering: $\gamma + p \longrightarrow \gamma + p$

The schematics of these transitions are shown in Figure 1-1. In these reactions, there is a pronounced peak in the cross section due to the delta resonance. One advantage of studing the Δ resonance is that it is the clearest nucleon resonance, well separated from other higher energy resonances. The π^+ photoproduction has large non-resonant backgrounds due to the Born Term. We need to determine the resonance part of the reaction in order to get the D state component of the delta. Neutral pion photoproduction has a much smaller non-resonant background, partly because it is neutral (Figure 1-2) [5]. However, in both π^+ and π^0 photoproduction there are final state interactions between the final state proton and pion. This introduce some uncertainty in the interpretation of the experiment, since the final state interactions are not very well understood. Another useful channel to study the delta structure is the proton Compton scattering.

Compton scattering obeys two body kinematics, a useful signature for experiments. Since there is only a photon and a proton in the final state there is no final state interaction. Another important feature is that it has the same initial and final state, so all the complex intermediate hadronic processes must finally yield the simple initial state, neatly hiding all the hadronic violence and yet containing its full implications on the observables. Based on the above reasons, proton Compton scattering has been chosen in this experiment to study the proton.

1.3 Difficulties of Proton Compton Scattering and Previous Data

Although Compton scattering is a good tool to study proton structure, there are very few data for it in the Δ region at present. There are several difficulties in performing this experiment. First, the cross section for proton Compton scattering is very small compared to other nuclear reactions, being of the order of 0.2 $\mu b/sr$ at the Δ resonance. Secondly, neutral pion production and the subsequent decay of the π^0 to two photons provides a huge background. The protons from π^0 production are similar in energy to the Compton protons, and the subsequent forward-backward decay of the π^0 will create a photon whose energy is close to that of the Compton scattered photons. This makes it hard to separate the Compton events from the π^0 events.

Figure 1-3 shows previous Compton scattering data from the 1960's, the Bonn data from 1976, and the SAL data which were published very recently in 1993. The old data from De Wire *et al.* [6], Nagashima [7], and Gray *et al.* [8] have large statistical errors and poor energy resolution. Each data set covered only one or two energies. The Bonn data [9] were the best available data for many years before the newly published data from a Saskatchewan Accelerator Laboratory (SAL) group. The Bonn data covered a wide energy range and had improved statistics. However, the Bonn data have poor energy resolution ($\pm$11 MeV). The new SAL data [10] have good energy resolution, but the highest incident photon energy only goes up to 290 MeV and is below the Δ resonance peak. At the resonance peak previous data are widely scattered and smaller than the unitary bound, thus conflicting with theory (see Section 6-3).

All the previous cross sections were measured with unpolarized photons. There is only one datum available for the photon polarization asymmetry, measured by a Italian group in 1967 [11]. This datum has a relatively poor statistical error. Different theories (Chapter 6) can not be unambiguously tested by this single datum (Figure 1-3). In the present experment,

polarized cross sections are measured from 225 MeV up to the Δ resonance peak around 325 MeV. The polarization asymmetries were obtained as a function of photon energy with much improved statistics. The characteristics of scattering with polarized beams are given in the next section.

1.4 The Polarization Degrees of Freedom

1.4.1 The polarization cross section

The photon polarization plane is defined as the plane in which its electric field oscillates. Linearly polarized photons have a unique polarization plane. The cross section measured with a polarized beam can reveal the information associated with the polarization degrees of freedom. Such information is a necessity in studying the subtle structures of the nucleon. Conventional Bremsstrahlung γ-rays are unpolarized. The cross section from an unpolarized photon beam is an average of orthogonal polarization directions and information is lost in the averaging process.

The differential cross section for scattering a linearly polarized beam, with polarization angle Φ from the reaction plane (Figure 1-4), can generally be separated into polarization independent and dependent parts:

$$\frac{d\sigma}{d\Omega}(\theta, \Phi) = I_0(\theta) + P I_1(\theta) \cos 2\Phi \tag{1.2}$$

where P is the degree of polarization, ranging from 0 to 1, and θ is the scattering angle. The first term, $I_0(\theta)$, is independent of the beam polarization angle Φ, but the second term has a polarization angle dependence.

The photon polarization has two degrees of freedom. Two polarization directions perpendicular with each other are chosen here. Parallel polarization ($\|$) is defined as the polarization

direction parallel to the reaction plane, and perpendicular polarization($\perp$) is defined as that perpendicular to the reaction plane. With a linearly polarized beam, there are two independent cross sections: $\frac{d\sigma_{\parallel}}{d\Omega}(\theta)$ and $\frac{d\sigma_{\perp}}{d\Omega}(\theta)$. The polarization independent part, $I_0(\theta)$, and the polarization dependent part, $I_1(\theta)$, can be expressed in terms of $\frac{d\sigma_{\parallel}}{d\Omega}(\theta)$ and $\frac{d\sigma_{\perp}}{d\Omega}(\theta)$:

$$I_0(\theta) = \frac{1}{2} \left(\frac{d\sigma_{\parallel}}{d\Omega}(\theta) + \frac{d\sigma_{\perp}}{d\Omega}(\theta) \right) \tag{1.3}$$

$$I_1(\theta) = \frac{1}{2} \left(\frac{d\sigma_{\parallel}}{d\Omega}(\theta) - \frac{d\sigma_{\perp}}{d\Omega}(\theta) \right). \tag{1.4}$$

$I_0(\theta)$ is the unpolarized Compton scattering cross section, since the polarization dependent part yields zero when summed over all polarization directions.

1.4.2 The asymmetry and the $E2/M1$ mixing ratio

A polarized beam can provide a more stringent test for models than an unpolarized beam. Polarization cross sections reveal more information about proton structure and are more sensitive to the details of different models. Comparisons with the calculations from different models can show if the details are correct.

A commonly used polarization observable is the cross section asymmetry Σ, which is defined as the ratio of the polarization dependent part and the polarization independent part:

$$\Sigma = \frac{I_1}{I_0} = \frac{\left(\frac{d\sigma_{\parallel}}{d\Omega}(\theta) - \frac{d\sigma_{\perp}}{d\Omega}(\theta) \right)}{\left(\frac{d\sigma_{\parallel}}{d\Omega}(\theta) + \frac{d\sigma_{\perp}}{d\Omega}(\theta) \right)} \tag{1.5}$$

An important use of the polarized beam is to study the tensor force component in the $q-q$ interactions [3]. Nonrelativistic spherical bag models have been very successful in predicting many particle properties. However, they have failed to reproduce a few important

observables such as the axial vector coupling constant g_A [3]. S. Glashow suggested in 1979 that the inclusion of a tensor component in the $q-q$ potential may solve this problem [12]. This tensor interaction is an analogue of the magnetic dipole interaction. The tensor component in the potential leads to a D-wave component in the predominantly spherical nucleon wave function. That is, the shape of the nucleon will be deformed from a sphere.

A D-wave component in the nucleon wave function also leads to a small quadrupole amplitude in the $N-\Delta$ transition, which is primarily a magnetic dipole transition. This small quadrupole amplitude is usually expressed in terms of a ratio of the electric quadrupole amplitude to the magnetic dipole amplitude, *i.e.* $E2/M1$. In recent years, interest in this mixing ratio has increased significantly. Theoretical predictions of this $E2/M1$ ratio range from -0.9 in the deformed Chiral bag model to -2.9 in the revised Skyrme model [3]. There have been many attempts to extract the $E2/M1$ ratio from the existing pion photoproduction data. The extracted $E2/M1$ ratios are listed in Table 1-1.

The wide spread, sometimes incompatible, values of this $E2/M1$ ratio show that our present understanding of the D-wave component and the tensor interaction is very poor. These values only show that this ratio is small. The errors and scatter in the values are partly due to the fact that most of the data were collected in experiments which were not designed to measure this ratio. Part of the reason is the uncertainty from the interference of non-resonance background processes. The results of the present experiment can, hopefully, be used for a better determination of the $E2/M1$ mixing ratio.

1.5 The Uniqueness of the Present Experiment

This proton Compton scattering experiment was conducted at the Brookhaven National Laboratory (BNL), with the γ-ray beam of the LEGS facility. One unique feature of this experiment is that the γ-rays are highly polarized, close to 100%. The polarization is

Table 1-1: $E2/M1$ ratio extracted from existing pion photoproduction data

reference	$E2/M1$ ratio %
Metcalf & Walker(1974) [13]	-1.2 ± 1.3
Omelaenko & Sorokin(1983) [14]	-0.6 ± 0.1
	-0.6 ± 0.1
Crawford & Morton(1983) [15]	-1.17
Tanabe & Ohta(1985) [16]	-3.7 ± 0.4
Yang [17]	-7.9
Davison, Mukhopadhyay, Wittman(1986) [18]	-1.5 ± 0.2
Cenni, Dillon, Christillin(1987)[19]	0
Li [20]	-2.5
Laget(1988) [21]	-4.0
Davison, Mukhopadhyay(1990) [22]	-0.59 ± 1.01
	-2.25 ± 1.02
Nozawa, Blankleider, Lee [23]	-3.1
Davison, Mukhopadhyay, Wittman(1991) [24]	-1.57 ± 0.72

obtained by backscattering laser light from a circulating 2.5 GeV electron beam. A detailed description of LEGS is in Chapter 2.

The γ-ray beam at LEGS is tagged. Unlike the tagged Bremsstrahlung beam, the tagging efficiency is 100%, due to the unique production mechanism of the γ-ray beam. This makes it possible to determine the γ-ray flux accurately. Therefore, the Compton scattering cross section can be determined with less systematic error. The LEGS γ-ray beam can reach a relatively high flux, about 10^7 photons per second.

The differential Compton scattering cross sections with the γ-ray polarization parallel and perpendicular to the reaction plane have been measured. The polarization direction in the LEGS γ-ray beam can be controlled by computer and can be rotated easily. This makes it possible to measure the cross section with the two polarizations in the same run. In the ratio of the two cross sections most of the systematic error can be cancelled out.

Another unique device in this experiment is the high energy, high resolution gamma-ray spectrometer. Since the Compton scattering has a huge background from π^0 decay to photons, which are very close in energy to the Compton photon, a high performance γ-ray spectrometer is needed. The gamma-ray spectrometer, with a cylindrical NaI(Tl) crystal 19 inch in diameter and 19 inch in length, has been designed and built. At present, it is the biggest detector of its kind in the world. It can contain most of the energy from high energy photons, and thus has a excellent energy resolution. The detector also has an excellent live surrounding shield, so that events with energy leaking out can be eliminated. The energy resolution for 300 MeV γ-rays is about 1.6%. This makes it possible to get a good separation of the Compton events from the π^0 decay background.

A drift chamber system is used to determine the proton scattering angle. And the energy of the recoil proton is measured in order to improve the separation of the Compton peak from the background. An array of NaI bars were placed opposite to the big NaI detector to veto some of the π^0 events. The unique features of this experiment lead to a good determination of the cross section with polarized photons.

Chapter 2 describes the γ-ray production mechanism and the main components of the LEGS facility. The proton Compton scattering experimental set up is described in Chapter 3. The data analysis is given in Chapter 4. The calculation of the polarization cross section and the final results are in Chapter 5. Chapter 6 describes different models and compares our results with model calculations and previous data. Chapter 7 gives the conclusions and outlook.

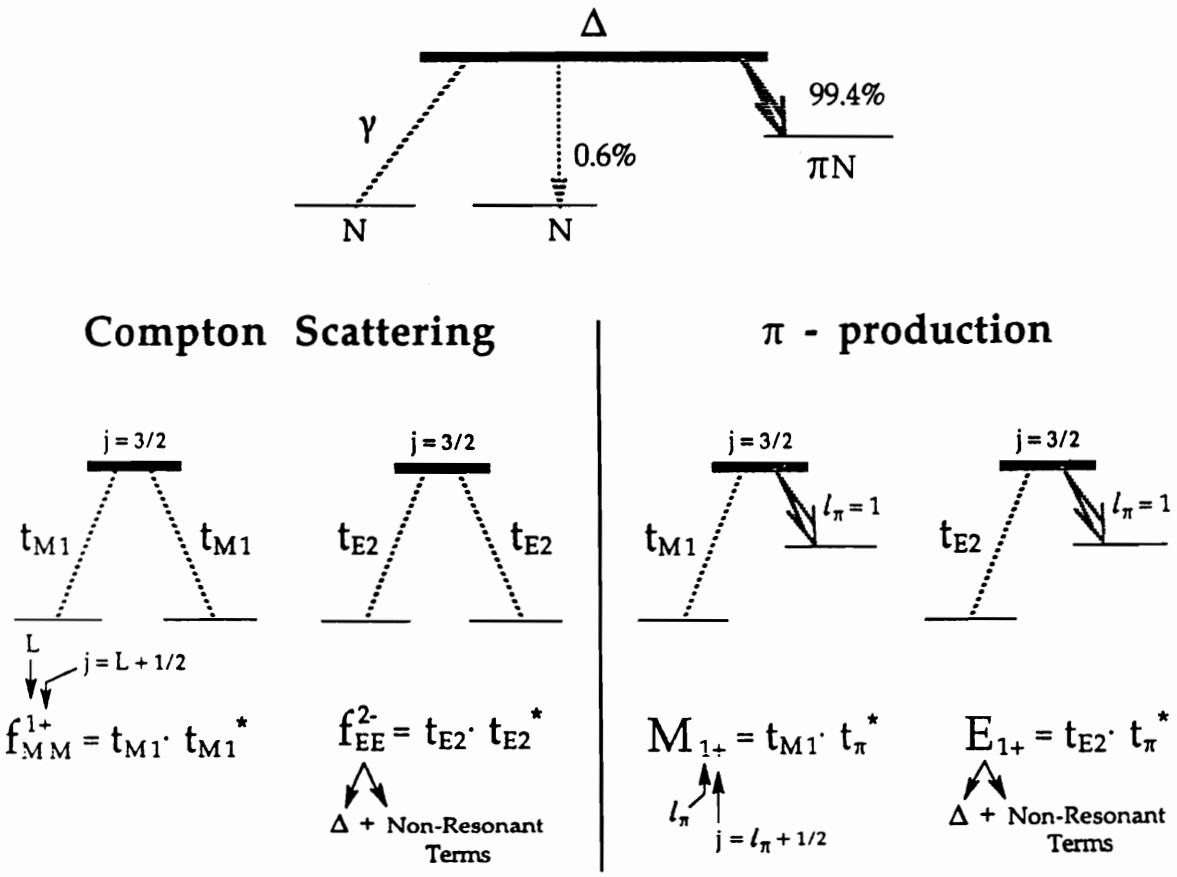

Figure 1-1: Schematic of the $N - \Delta$ transition in the proton Compton scattering channel and the pion photoproduction channels.

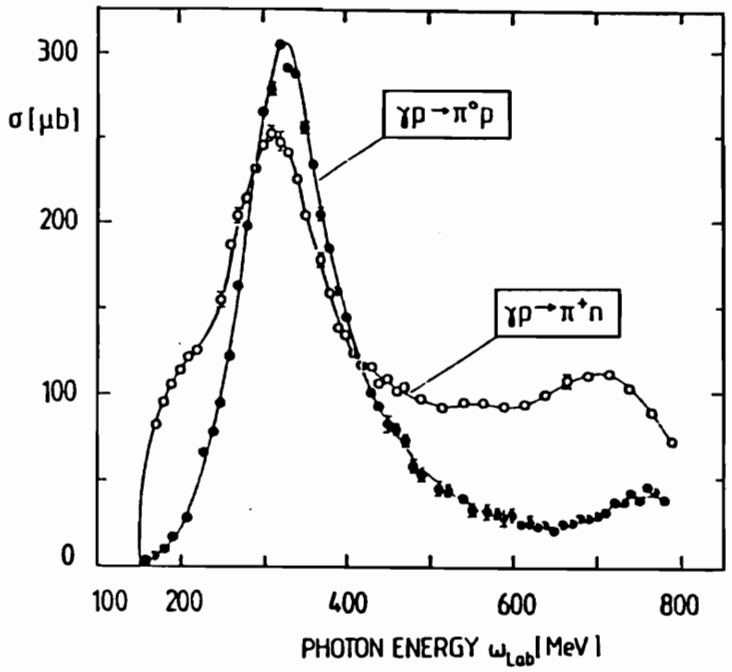

Figure 1-2: Total cross section for π^0 and π^+ photoproduction [5]. A considerable non-resonance background can be seen in the π^+ photoproduction, while the background is much smaller in the π^0 production.

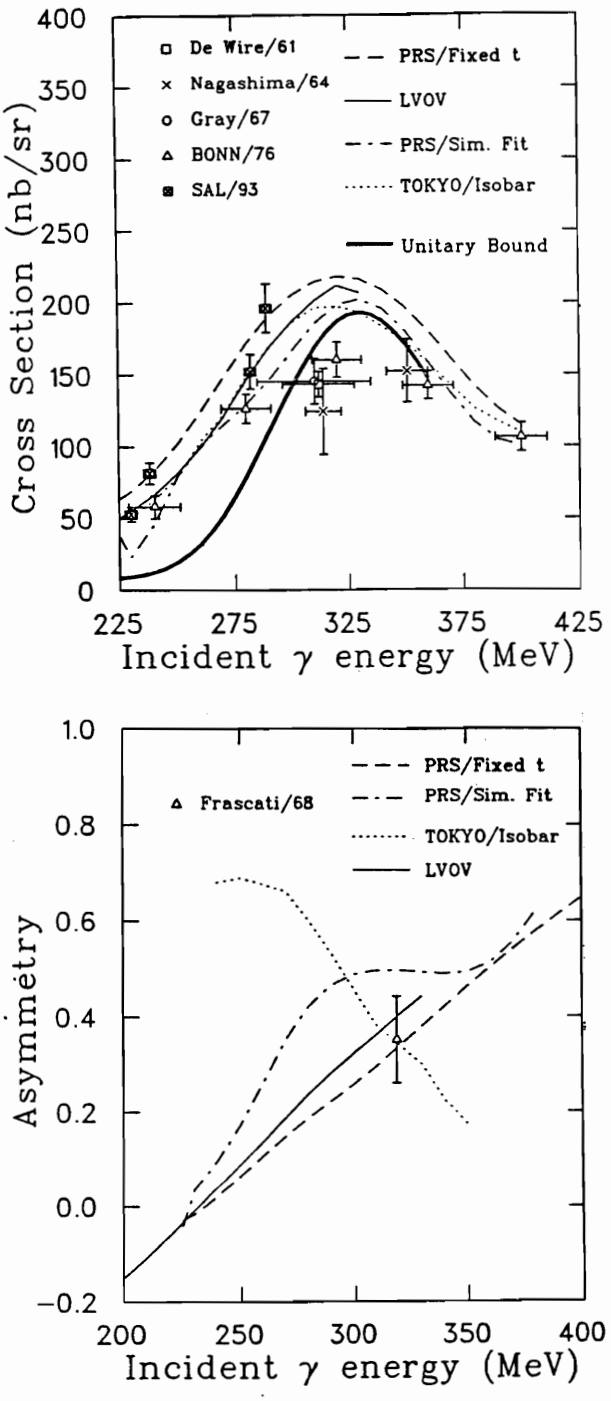

Figure 1-3: Previous Compton scattering data in the Δ region. Upper: the unpolarized Compton scattering cross section. The sources of these data are: De Wire *et al.* [6]; Nagashima, [7]; Gray *et al.* [8]; Bonn data, [9]; SAL data, [10]. Lower: The only datum of the cross section asymmetry from [11]. Discussion of various models is in Chapter 6.

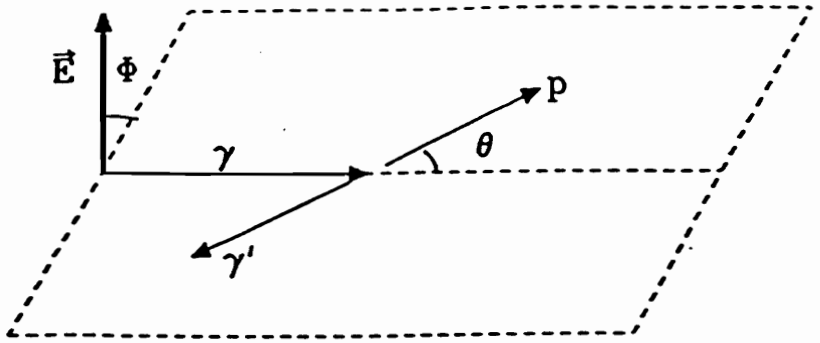

$$\Phi = 0° \Rightarrow d\sigma_{\parallel}/d\Omega$$
$$\Phi = 90° \Rightarrow d\sigma_{\perp}/d\Omega$$

$$d\sigma_{unpol} = \frac{1}{2}(d\sigma_{\parallel} + d\sigma_{\perp})$$

$$\Delta = \frac{1}{2}(d\sigma_{\parallel} - d\sigma_{\perp})$$

$$\Sigma = \frac{(d\sigma_{\parallel} - d\sigma_{\perp})}{(d\sigma_{\parallel} + d\sigma_{\perp})}$$

Figure 1-4: Kinematic vectors for scattering with a polarized beam. The photon polarization angle is Φ. The relations of unpolarized cross section and asymmetry with polarized cross sections are also shown.

Chapter 2

LEGS Facility

2.1 General Description

LEGS Stands for Laser Electron Gamma Source. The LEGS facility provides highly polarized and monochromatic gamma rays with energies up to 331 MeV. Instead of using the traditional way of producing gamma rays via Bremsstrahlung, the mechanism of laser photon electron backscattering is used at LEGS to produce gamma rays. Photons of a few eV from a laser are shined head-on at a highly relativistic electron beam. After backscattering from an electron the photon gains an enormous amount of energy. For a 2.5 GeV electron the photon gains about 100 million times its original energy and becomes a gamma ray of a few hundred MeV. A detailed description of the production mechanism is given in section 2.2 .

The idea of producing high-energy gamma rays by electron backscattering was proposed by Arutyunian, Tumanian and Milburn in 1963 [25] [26]. It was introduced to explain the observed high-energy gamma component of cosmic rays, created by the backscattering of the visible star light with highly relativistic electrons in the space.

The LEGS facility is located at the National Synchrotron Light Source (NSLS) of the Brookhaven National Laboratory (BNL). LEGS make use of the 2.5 GeV high current (about 250 mA) electron beam in the NSLS X-ray storage ring. The layout of the LEGS facility is shown in Figure 2-1. The LEGS experimental floor has two target areas and three electronics and data acquisition rooms. The electron beam goes clockwise around the storage ring in Figure 2-1. A laser beam is pointed at and aligned with the electron beam in the straight section where the photon electron backscattering takes place. The distance between the center of the straight interaction section and the down-stream experimental target is 43 meters. After backscattering gamma photons pass through the collimator and sweeping magnet and enter the target area. Charged particles in the γ-ray beam are swept out by the sweeping magnet. The collimator is made of nickel slits and used to confine the gamma beam spot at the target. The electron which lost energy in the backscattering process is bent out of the ring and enters a tagging spectrometer. The energy of the electron is measured in the spectrometer so that the energy of the corresponding photon is obtained.

In the Bremsstrahlung process, photons are created when the electron decelerates in the field of a nucleus. The energy of a Bremsstrahlung photon can range from 0 up to the electron energy. The intensity of the Bremsstrahlung beam decreases very rapidly with energy, almost as $\frac{1}{E_\gamma}$, and drops to 0 at the highest energy. Thus a Bremsstrahlung beam with reasonably high flux is always accompanied by a large low-energy photon tail, which could create many background processes. Moreover, a Bremsstrahlung beam is generally unpolarized. By using a special scatterer, such as diamond crystal, a partially polarized Bremsstrahlung beam can be obtained. However, the polarization so far obtained is low, $\leq 30 - 40\%$.

The gamma ray from electron Compton backscattering does not have the disadvantages of the Bremsstrahlung beam. The gamma rays from LEGS have several distinguishing features because of the unique production mechanism:

- The gamma rays are almost 100% polarized at the Compton edge. The beam can

be polarized circularly or linearly along any direction. This is because backward Compton scattering preserves photon polarization.

- The polarization direction can be changed quickly from one state to another, so that data can be taken for reactions with different photon polarization in the same run.
- The low-energy gamma ray background is small, and it can be further reduced with collimators since low-energy photons are directed away from the center of the beam.
- The energy of the gamma photon is measured by means of the 'tagging' spectrometer. The photon energy resolution is about 5 MeV throughout the tagging range.
- The flux of gamma rays is relatively large, of the order of 10^7 photons/second in the range of 200-331 MeV.

The photon is an electromagnetic probe. In studying the basic structure of elementary particles and the interactions between them, electromagnetic probes have certain advantages. Electromagnetic interactions are well understood and can be calculated accurately. From the experimental results information concerning the interactions under study can be accurately extracted. With other types of probes, such as hadronic probes, it is harder to extract the information needed, because certain aspects of the probe itself are not understood well.

The other type of electro-magnetic probe is the electron. Electrons interact by means of virtual photons. Virtual photons have wider dynamic range since its momentum squared, Q^2, can be different from zero, and it is relatively easy for virtual photons to reach very high energies. But a real photon probe has many unique features. A real photon, by its name, is real (it has zero mass) and can be directly observed; whereas a virtual photon needs to be inferred and understood through the theory of electromagnetic interactions. Real photons can be used as a tool to test and verify theories of electromagnetic interactions. Complementary measurements with both real and virtual photons serve as important cross checks. Moreover, since the form factors for photon interactions are significantly different

from these for electron interactions, there are many problems that can be more suitably studied with a real photon probe [28].

The backscattering production mechanism is described in section 2. The main components of the LEGS facility, *i.e.*, the NSLS electron beam, the laser beam, the feedback system, the tagging system, and the beam monitor system are described in sections 3 through 7.

2.2 The Gamma Photon Production Mechanism

2.2.1 Backscattering kinematics

The backscattering of a photon off an electron is shown schematically in Figure 2-2(a). where $\vec{k_e}$ is the initial electron momentum, $\vec{k_i}$ and $\vec{k_f}$ are the initial and final photon momenta. The incident and recoil angles, ϕ and θ, are small. The backscattering process can be conveniently calculated by means of Lorentz transformations along the direction of the electron momentum.

In the first transformation the system is transformed into the electron rest frame. The energy of the laser photon is boosted according to:

$$E_l' = \gamma \ (E_l + \beta \ p_l) \tag{2.1}$$

where E_l and E_l' are the photon energy before and after the first Lorentz boost, $\beta = v/c$, $c = 1$, and $\gamma = \frac{1}{\sqrt{1-\beta^2}}$. For a relativistic electron with energy of 2.5 GeV, $\beta \sim 1$, $\gamma \doteq 5000$ and $E_l' \doteq 2\gamma E_l = 10000 E_l$, *i.e.*, the photon energy in the electron rest frame is 10000 times its energy in the laboratory frame. At the same time, the incident angle ϕ will be greatly compressed. For $\gamma \doteq 5000$, all incident angles will be compressed into a fraction of a degree (Figure 2-2(b)).

After backscattering the system is transformed back into the laboratory frame. The energy of the scattered photon is boosted by another factor of 2γ. The angular spread of the outgoing photon will be compressed again due to the second Lorentz boost (Figure 2-2(b)).

As a result of the two angular compressions the backscattered photon energy is unaffected by the initial photon incident angle ϕ. Therefore, the initial finite divergence in the laser will not affect the backscattered photon energy [27, 3]. To an excellent approximation the backscattered photon energy can be written as:

$$E_\gamma = \frac{4\gamma^2 E_l}{1 + \frac{4\gamma E_l}{m_e c^2} + \theta^2\gamma^2} , \tag{2.2}$$

where m_e is the rest mass of the electron, and E_l and E_γ are the photon energies before and after the backscattering in the laboratory frame. The backscattered photon reaches the maximum energy at $\theta = 0°$. For the case of $E_e = 2.5$ GeV and $E_i = 3.0$ eV the angular dependence of the backscattered photon energy is shown in Figure 2-3.

2.2.2 The cross section for backscattering

The scattering cross section in the laboratory frame can be obtained by transforming the cross section in the electron rest frame to the laboratory frame. The Compton scattering cross section for a linearly polarized photon in the electron rest frame is given by[28, 29]:

$$\frac{d\sigma}{d\Omega} = \frac{r_0^2}{4}\left(\frac{E'_\gamma}{E'_l}\right)\left(\frac{E'_\gamma}{E'_l} + \frac{E'_l}{E'_\gamma} - 2 + 4\cos\xi\right) \tag{2.3}$$

where r_0 is the classical electron radius ($2.828fm$), E'_l and E'_γ are the photon energies before and after the backscattering in the rest frame, and ξ is the angle between the initial and final photon polarization vectors. E'_γ and E'_l are related by:

$$\frac{E'_\gamma}{E'_l} = \frac{1}{1 + \frac{2\gamma E'_l}{m_e c^2}(1 + \cos\theta')}, \tag{2.4}$$

where θ' is the polar scattering angle in the electron rest frame. ξ is a function of the polar and azimuthal angles, θ and ϕ_γ, of the outgoing photon. If θ is measured relative to the direction of the Lorentz transform, then $\phi'_\gamma = \phi_\gamma$, where ϕ'_γ is the azimuthal scattering angle in the electron rest frame. θ' and θ are related by the equation given in Figure 2-2. The parallel cross section scattered into θ' and ϕ'_γ can be written as:

$$\frac{d\sigma_{\|}}{d\Omega'} = \frac{r_0^2}{4}\left(\frac{E'_\gamma}{E'_l}\right)\left(\frac{E'_\gamma}{E'_l} + \frac{E'_l}{E'_\gamma} + 2 - 4\sin^2\theta'\cos^2\phi'_\gamma\right)(1 - \sin^2\theta'\cos^2\phi'_\gamma) . \tag{2.5}$$

The unpolarized cross section going into θ' and ϕ'_γ is:

$$\frac{d\sigma_{tot}}{d\Omega'} = \frac{r_0^2}{4}\left(\frac{E'_\gamma}{E'_l}\right)\left(\frac{E'_\gamma}{E'_l} + \frac{E'_l}{E'_\gamma} - 2\sin^2\theta'\cos^2\phi'_\gamma\right). \tag{2.6}$$

The Klein-Nishina formula [30] can be obtained by integrating over ϕ_γ :

$$\frac{1}{2\pi}\int_0^{2\pi}\frac{d\sigma_{tot}}{d\Omega'}\,d\phi = \frac{r_0^2}{4}\left(\frac{E'_\gamma}{E'_l}\right)\left(\frac{E'_\gamma}{E'_l} + \frac{E'_l}{E'_\gamma} - 2\sin^2\theta'\right). \tag{2.7}$$

To obtain the cross section in the laboratory frame the electron rest-frame cross section needs to be multiplied by the the quantity:

$$\frac{d\Omega'}{d\Omega_{lab}} = \gamma\frac{\sin^2\theta + \cos\theta(\cos\theta - \beta)}{(\sin^2\theta + \gamma^2(\cos\theta - \beta)^2)^{\frac{3}{2}}}. \tag{2.8}$$

The cross section in the laboratory frame can be expressed as:

$$\frac{d\sigma_{tot}}{d\Omega_{lab}} = \frac{d\sigma_{tot}}{d\Omega'}\frac{d\Omega'}{d\Omega_{lab}}, \quad \frac{d\sigma_{||}}{d\Omega_{lab}} = \frac{d\sigma_{||}}{d\Omega'}\frac{d\Omega'}{d\Omega_{lab}} \tag{2.9}$$

The Lorentz transformation compresses the cross section into a small angular cone about $\theta_{lab} = 0$. The compression effect increases approximately as the square of the electron energy. The lab cross section as a function of lab scattering angle for a 3 eV incident photon and a 2.5 GeV electron is shown in Figure 2-3. It can be seen that the high-energy gamma rays peak strongly at small angles. The low-energy gamma component is away from the γ-ray beam center and can be eliminated by a collimator.

The γ-ray flux as a function of energy, after integration over the the proper solid angle, is shown in Figure 2-4(a) for five different laser photon energies. Compared with the Bremsstrahlung gamma spectrum in which the intensity decreases roughly as $\frac{1}{E_\gamma}$, the backscattering spectrum is much flatter. In contrast to the Bremsstrahlung beam in which the flux is smallest at the maximum energy, the maximum flux for backscattered γ-rays is obtained at the highest energy at the tagging range.

Figure 2-5(d) shows the effects of the dynamics and kinematics of the backscattering on the spacial distribution of the γ-ray flux. This figure shows the case with the incident

photon polarization $\vec{\epsilon}$ parallel to the electron orbital plane (horizontal). The right side of Figure 2-5(d) indicates that the angular cross section for backscattering peaks in the plane perpendicular to the plane of the incident photon polarization. The middle part of Figure 2-5(d) shows that, for a γ-ray energy smaller than the maximum, the backscattered γ-ray is kinematically constrained in a circular band. The left part of the figure shows the folding of the two effects. The hatched area indicates the region of intense γ-ray flux. The results of the Monte Carlo simulation of this process, shown in Figure 2-5(c), are compared with the real γ-ray profile in Figure 2-5(b). At 100 MeV the profile shows two distinct lobes. Close to the Compton edge at 200 MeV the separation between the two lobes are not observable, which agrees very well with the Monte Carlo results.

2.2.3 Polarization of the Backscattered γ-Rays

The Compton backscattering preserves most of the linear polarization of the incident photon. This can be seen by comparing the parallel component of the cross section with the unpolarized cross section, $\frac{d\sigma_{tot}}{d\Omega'}$, in equation 2-9. The polarization of the backscattered γ-ray is the ratio of the parallel to the unpolarized cross section. Figure 2-6 shows the parallel and unpolarized cross section as a function of the scattering angle.

It can be seen that, at $\theta_{lab} = 0$, where both the energy and cross section are at the maximum, the γ-rays are 100% polarized. For angles less than 10^{-4} radians the polarization can be approximately expressed as:

$$P \simeq 1 - (\theta\,\gamma)^2\,, \tag{2.10}$$

where θ is in radians. By using different laser energies the backscattered polarization can reach 90% and higher polarization over the desired energy range(Figure 2-4 (b)).

2.3 NSLS electron beam

The National Synchrotron Light Source(NSLS) is one of the largest accelerator facilities dedicated to synchrotron radiation research. It has one of the brightest sources of synchrotron radiation in the UV and X-ray energy range. A floor plan of NSLS is shown in Figure 2-7. There are two electron storage rings. The smaller ring, called the UV ring, stores 750 MeV electrons and yields UV radiation. The larger one, called the X-ray ring, accelerates and stores electrons up to 2.5 GeV.

The X-ray storage ring has a very intense electron current, with maximum current of 250 mA. As a result the γ-rays from LEGS can reach a relatively high intensity. The parameters of the X-ray ring are shown in Table 2-1 [33]. LEGS is designed to operate at all standard ring turns with other users operating at the same time.

Electrons circulate the ring in spatially localized groups called 'bunches'. The natural bunch length is 0.3 ns (10.5 cm long) with 18.9 nsec separation between adjacent bunches. The ring can hold a maximum of 30 bunches. However, normally it operates with 25 bunches distributed asymmetrically around the ring, in order to decrease the ion concentration in the passage of the beam due to the periodical field from the motion of electrons.

Between two bending magnets in the X-ray ring there is a straight section. The LEGS facility is built around the straight section ahown as X5 at the bottom of the X-ring in Figure 2-7. Figure 2-1 is a detailed layout of that portion. The electron beam is focused in the straight section to a size of $\sim 0.40 \pm 0.06\ mm$ in the horizontal direction, and $\sim 0.026\ mm$ in the vertical direction, with angular divergences of $\sigma_x \simeq 235\ \mu rad$ and $\sigma_y \simeq 74\ \mu rad$. Most of the γ-ray flux is generated in the center of the straight section, since the electron and laser beam have the smallest transverse extent there.

Table 2-1: NSLS X-ray storage ring parameters

Parameters	X-ray Storage Ring
Normal Operating Energy	2.584 GeV
Maximum Operating Current	250 mA
Lifetime	$\sim$ 20 hrs
Circumference	170.1 meters
Electron Orbital Period	567.7 nanosecond
Number of Super-periods	8
Magnet Complement	16 Bending (2.7 meters each)
	40 Quadrupole (0.45 meters each)
	16 Quadrupole (0.80 meters each)
	32 Sextapole (0.20 meters each)
RF Frequency	52.888 MHz
Radiated Power for Bending Magnets	126 KW/0.25 Amp of Beam
RF Peak Voltage	700 kV
Design RF Power	300 kW
Natural Energy Spread (σ_ϵ/E)	0.00082
Natural Bunch Length (2σ)	10.5 cm
Maximum number of RF Buckets	30 (18.9 ns apart)

2.4 The Laser Beam

Lasers provide photons for backscattering, since laser beams have high intensity and are linearly polarized. The laser and optical devices are placed in the laser hutch. In the present experiment an Ar-Ion laser (Coherent, INNOVA 200-25/7 UVA) was used. It can operate in a single-line or multi-line mode from 300.2 nm to 528.7 nm, delivering a power up to 30 W (in multi-line visible mode). In the present experiment the laser was operated in the multi-line UV emission mode. This mode has three close laser lines having approximately equal intensity with wavelengths of 333.6 nm, 351.1 nm, and 363.8 nm. The photon energies are 3.72, 3.53 and 3.41 eV and produce γ-rays with energies of 331.2, 316.8 and 307.0 MeV, respectively.

The laser is placed on an optical bench. The optical bench is shown in Figure 2-8. Since the laser cannot be in the way of the γ rays, it is placed parallel to the γ-ray beam at a distance of 23.5 cm. The laser beam is reflected by two mirrors, M1 and M2, pointed to and aligned with the electron beam in the straight section. Out of the laser there is a half-wave plate (polarization rotator), through which a linear beam remains a linear beam. But when the plate is rotated, the polarization direction of the out-going laser beam also rotates. A quarter-wave plate can translate a linear beam into a circularly polarized beam. The prism and the mirror M2 can translate and rotate the laser beam, respectively, in order to align it with the electron beam. The two optical lenses focus the laser beam at the center of the straight section. The backscattered γ-ray goes back into the laser beam, passes through the mirror M2, sweeping magnet, and collimator, and then enters the target area. The polarization rotator is computer controlled. The laser polarization, and thus the γ-ray polarization, can be easily changed by the computer.

The polarization of the laser beam is linear when it comes out of the polarization rotator. After going through optical devices the polarization of the laser beam will drop slightly. The degree of polarization in a certain direction was measured before and after the straight interaction section. In the measurement, the beam was reflected by a Brewster window. The

reflected power in the incident plane was measured when the incident plane was parallel and perpendicular to the polarization plane, denoted by $N_{||}$ and $N_{\perp}$, respectively. The degree of polarization of the laser beam in this direction, P^L, can be written as:

$$P^L = \frac{N_{||} - N_{\perp}}{N_{||} + N_{\perp}}. \tag{2.11}$$

At the straight section the laser polarization is approximately 96%.

In order to measure cross sections with incident γ-ray polarization parallel and perpendicular to the reaction plane under similar conditions, the laser polarization is flipped between the two polarizations during a run. The flipping duration of each polarization is set at random around a time interval. In this way most of the systematic errors can be canceled out in the ratio of the two polarization cross sections. The duration of the two polarization states differs by a small amount. Because the mirrors have higher reflectivity for photons with polarization in the reflection plane, the γ-ray flux with parallel polarization is a few percent smaller than that with perpendicular polarization. Since an equal amount of total flux is desired for both, the duration for parallel and perpendicular states is set at an average of 335 *sec* and 300 *sec*, respectively.

When flipping the polarization the laser shutter is closed for 20 sec. During this time events from Bremsstrahlung radiation, which results from the residual gas in the beam pipe, are collected. This Bremsstrahlung background is unpolarized and will dilute the polarization of the γ-ray beam. The correction of the γ-ray beam polarization due to this background is included in the calculation of the cross sections. This Bremsstrahlung background is small, only about 0.2% of the total γ-ray beam.

2.5 The Tagging Spectrometer

The LEGS tagging system is used to momentum analyze the electrons after the backscattering process, so as to determine the corresponding gamma energy. The tagging system

is shown in Figure 2-9. It consists of two main parts, the tagging magnets and the focal plane hodoscope. The scattering angle η of the electron after producing a γ is related to the energy and angle of the gamma by[28]:

$$\eta = (\frac{E_\gamma}{E_e - E_\gamma})\theta. \tag{2.12}$$

For gamma energies of 200 to 331 MeV produced by backscattering from 2.5 GeV electrons $\eta \sim 0.5$ to 0.05θ. The cone of scattered electrons is about a factor of 10 times smaller than the already narrow γ-ray cone. Therefore, where the backscattering process happens along the straight section has little affect on the electron position at the focal plane.

2.5.1 The Spectrometer magnets

The tagging magnets consists of three external dipoles and one ring dipole [27]. The ring dipole and three external dipoles are labeled D1, D2, D3 and D4 (Figure 2-9 (b)). The D1 dipole faces are 15.5 cm wide, and the gap between them is 5.5 cm. At a stored electron beam energy of 2.5 GeV, D1 operates with a field of 1.19 T. The upper limit of the gamma energy that can be tagged is set by this field. In the normal operation mode the upper limit is about 500 MeV.

Because of the need for a large tagging range the external dipoles, especially D2, are located close to the electron beam. The fringing field from these magnets are a potential source of disturbance to the electron beam. In order to minimize the perturbations, the external magnets were constructed with trim coils to cancel out the fringe fields. The settings of the trim currents were determined by observing the disturbance to the electron beam when the magnets were turned on and off. At the final settings, when all magnets and trim coils are on, the disturbance to the beam is negligible and smaller than any present NSLS X-ray user can observe.

The magnet D2 is a septum magnet with a gradient field. The faces of D2 are 50 cm long and 11 cm wide with a gap of 1.2 cm. At normal beam energy of 2.5 GeV it operates with

a field of 1.6 T. The distance from D2 to the stored electron beam sets the lower limit of gamma energy that can be detected by the tagging system. The smaller the distance to the beam the lower the tagging limit can be. The limit of the distance is determined by the the clear aperture requirements of the ring during beam injection. In the final setting the D2 field is only 3 cm away from the storage beam. This determined the lower tagging limit to be 186 MeV.

Magnet D3 is constructed similar to D2 but larger, with a face length of 96 cm and a field gap of 1.9 cm. It operates at 1.16 T at normal beam energy, but can produce a stable magnetic field up to 1.9 T. Magnet D4 is a conventional 'C' magnet. It is far enough from the beam so that its fringing field has little effect on the beam. It is 79 cm long with a face gap of 5 cm. Its normal operating field is 1.29 T.

2.5.2 The Focal Plane Hodoscope

The tagging hodoscope is located in a shielded cave at the focal plane of the magnetic spectrometer about 6 meters away from D4(Figure 2-9). The shielded cave is to prevent the hodoscope from triggering on random non-tagged background radiation. The hodoscope is used to measure the relative position of electrons from which the corresponding photon energy can be obtained.

The hodoscope consists of two layers of plastic scintillators. In each layer are 64 square cells of plastic scintillators with a width of 0.76 cm. The front layer is offset by half a cell from the back layer. An eight stage photomultiplier tube (Hamamatsu R1635) is mounted on each scintillator. The rise time from these tubes is only 0.8 ns. Since the separation between two consecutive electron buckets is 18.9 ns, the signals from the hodoscope are fast enough to separate photons created in adjacent buckets. The maximum counting rate of the hodoscope is several MHz per element, much greater than the actual counting rate of about 10^4 Hz per cell. The focal-plane hodoscope was gain matched and a trigger timing resolution of less than 1 ns was obtained.

In previous LEGS experiments the signals from the 128 scintillators were sent to registers and the OR of all the front and back signals was sent to stop a TDC. The time of the first signal in the trigger gate was recorded and the fired tag channels at this time were recorded. This would cause difficulties in the data analysis, since in the trigger gate the true peak is not necessarily the first peak [31, 32]. In the present experiment, signals from each of the 64 front layer scintillators were sent to a TDC . This way we know for each event which tagger channel fires and the timing within the trigger gate.

The tagging range of the spectrometer can be adjusted within the allowed minimum and maximum limits, from 186 to 500 MeV. In the present experiment, the tagging spectrometer was adjusted to tag photons from 206 to 354 MeV. The energy resolution is 5 MeV throughout the tagging range. The energy resolution is predominantly determined by the energy spread of the NSLS electron beam[27].

2.6 The Feedback System

LEGS requires a highly stabilized electron beam at the straight section. At the beginning of each electron beam fill, the laser beam position and angle are adjusted to align with the electron beam in the straight section in order to maximize the γ-ray flux. When the electron beam moves, even slightly, the γ-ray flux will drop considerably, and the beam spot at the target position may move. There are some disturbances on the NSLS electron beam from a variety of random sources, such as power supply ripple and drift, inductance from electrical equipment near the beam, and floor vibrations, etc. From fill to fill, the beam position may also be slightly different.

In order to prevent these disturbances from changing the γ-ray flux and beam spot on the target, a feedback system was built and installed in the straight section. The feedback system can stabilize the electron beam in the straight section to a high precision. The feedback system is composed of beam position sensors and position adjusting coils. The

sensor is called PUE, or Pick Up Electrode. The beam position is measured and fed out in terms of RF signals. Each signal is sent to a RF receiver whose output is the amplitude of the signal. Each PUE sends out 4 RF signals, and the 4 amplitudes form a matrix. This matrix is multiplied by the interference matrix obtained from calibration in order to determine the proper correction voltages. The output voltages are applied to the adjusting coils and the beam is shifted back towards the center. When the beam is at the center position of the PUE the voltage outputs will be zero.

Two sets of PUEs and adjusting coils measure and correct the electron beam at only one position. Eight sets of PUEs and adjusting coils are used in the feedback system. Four sets are used to correct the orbit in the x and y directions at the upstream end of the straight section. Four other sets are used at the down stream end of the straight section to restore the orbit to its previous position. The feedback system can stabilize the beam to an accuracy of $\sigma_x = 50\mu m$ and $\sigma_\theta = 50\mu rad$.

Since the feedback system does not change the overall orbit state outside the straight section, LEGS has the freedom to adjust the electron beam position and angle in the straight section without disturbing other NSLS users. The feedback system also helps to stabilize the tagging spectrometer calibration. The electron beam shift will lead to a shift of the electron position in the spectrometer, thus changing the calibration coefficients. When the beam is stabilized by the feedback system the tagging spectrometer calibration is also stabilized.

2.7 The γ-ray Beam Profile Monitor (Photon Scanner)

The beam profile monitor, or photon scanner, measures the spacial distribution of the γ beam flux intensity in the target area. Photon scans are done at the beginning of each electron beam fill. The beam profile monitor serves several purposes. Firstly, it is used as a diagnostic tool to check weather the feedback system and the ring magnets are functioning properly. Secondly, the beam profile can be used to determine where the target should be

placed in order to maximize the flux going through the target material. Thirdly, it can be used to check if the position of the collimation slits is correct. Fourthly, the beam profile can be compared with the results of the Monte Carlo simulation of the backscattering process, and provides a cross check on the LEGS performance as well as the γ-ray polarization calculation (Figure 2-5).

The beam profile monitor is located in the path of the γ-ray beam 47.9 meters away from the center of the straight section. It is a scintillator hodoscope composed of 16 scintillators. Each scintillator has a width of 3.2 mm and is optically coupled to a Hamamatsu R1635 phototube. Eight of the scintillators are placed horizontally with a 3.2 mm space between adjacent scintillators; eight are placed vertically in the same manner. A converter, an aluminum plate, is placed in front of the profile monitor in order to convert a sample of the γ rays into electron positron pairs to be detected by the plastic scintillators. After taking enough counts in one position, the horizontal and vertical array can be shifted by 3.2 mm to cover the gap between two scintillators. Thus the 2×8 array of scintillators can measure the beam intensity at $4 \times 64 = 256$ different positions covering an area of $51.2 \times 51.2 mm^2$. The resolution is equal to the detector width of 3.2 mm.

The γ-ray flux profile has an approximately normal distribution. At the target position 41 meters away from the straight section center the FWHM is $\sim 22mm$ horizontally and $\sim 9mm$ vertically. The beam centroid at the target position is maintained to within $\pm 1mm$ with the help of the feedback system. Figure 2-5(a) shows the untagged γ-ray spectrum on the top panel, the 205 and 110 MeV tagged spectrum in the middle and lower panels, respectively. The beam profile corresponding to the 205 and 110 MeV γ-rays are shown in Figure 2-5(b). The results of the Monte Carlo simulation are shown in Figure 2-5(c) for comparison.

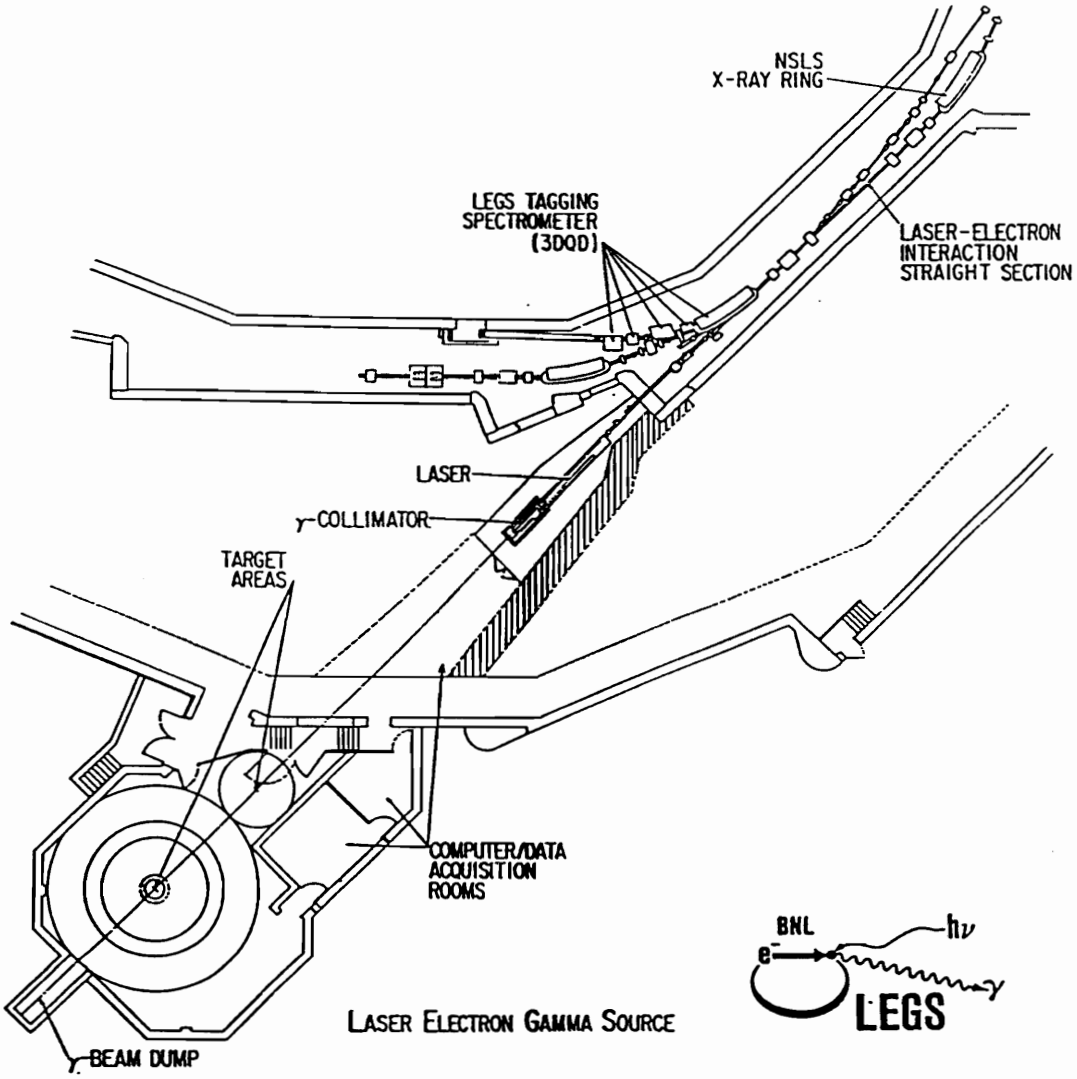

Figure 2-1: Layout of the LEGS facility

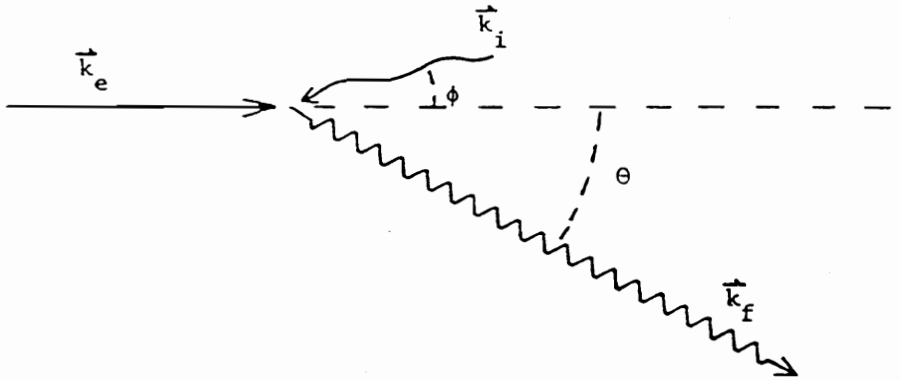

(a)

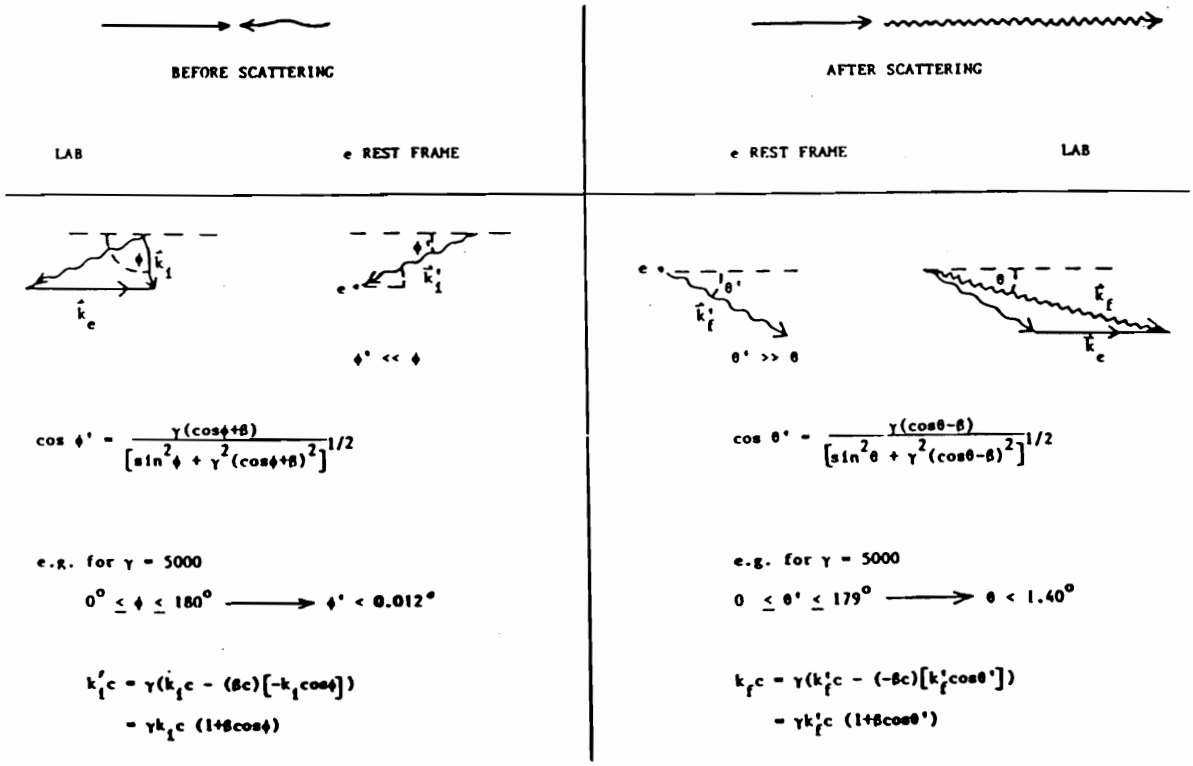

(b)

Figure 2-2: (a) Photon electron backscattering vectors. (b) Angular compression in the Lorentz transformations to and from the electron rest frame.

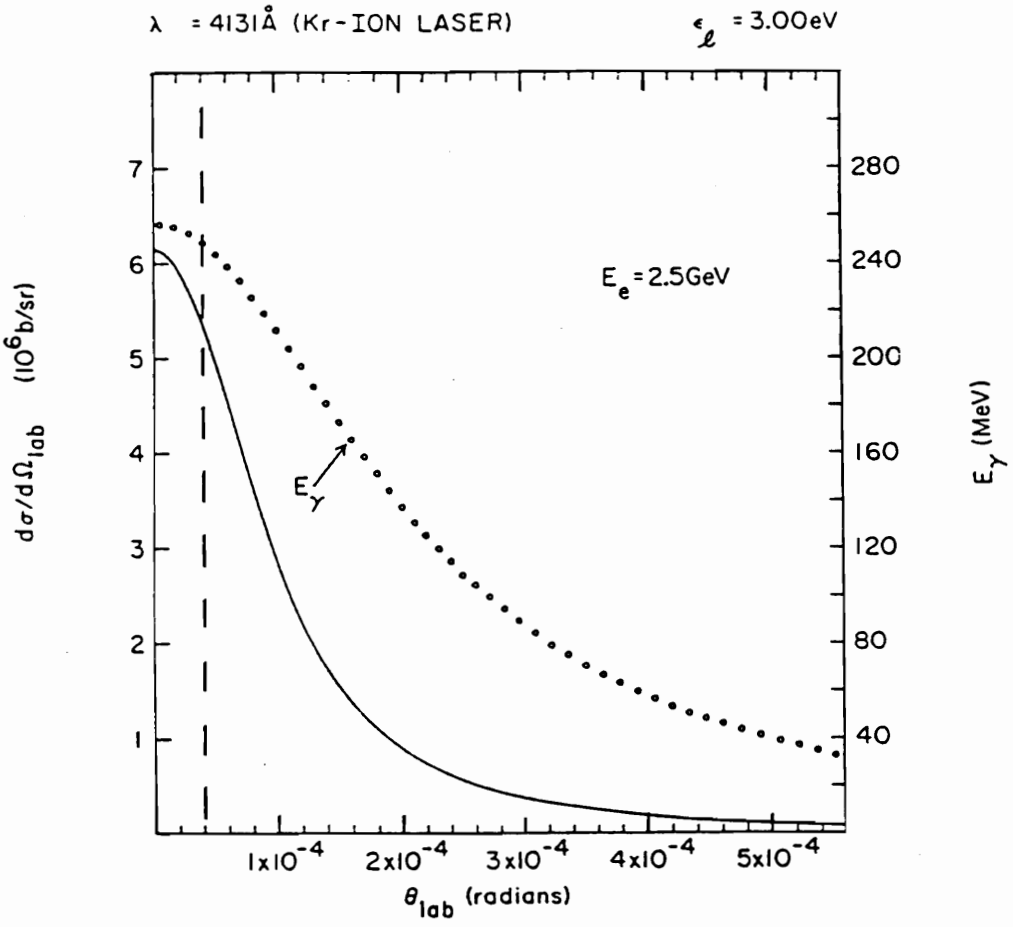

Figure 2-3: Backscattered photon cross section (left scale) and the γ-ray energy (right scale) in the laboratory frame as a function of the scattering angle for $E_l = 3eV$.

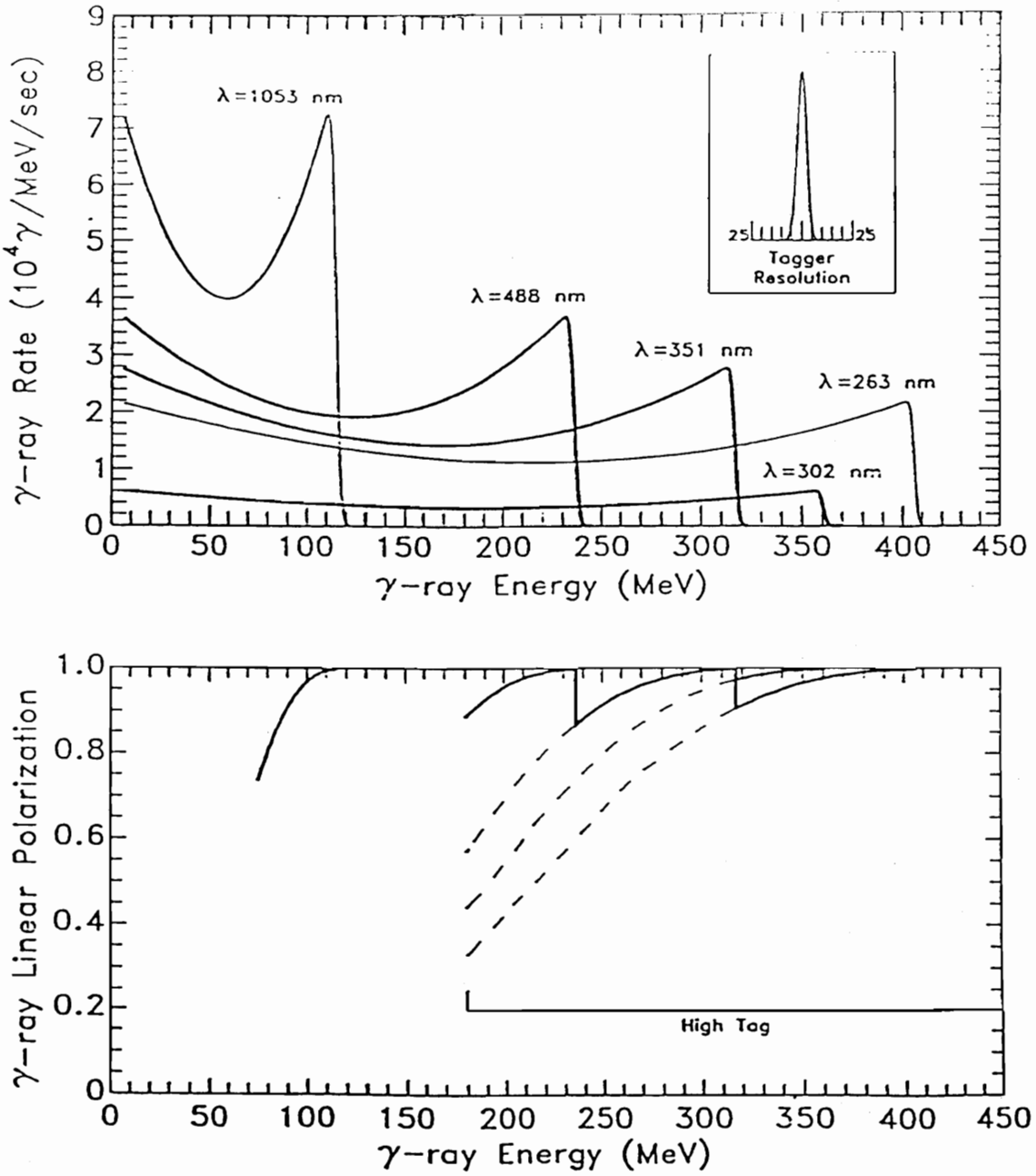

Figure 2-4: (a) Backscattered γ-ray flux as a function of the γ-ray energy for five different laser lines. (b) The γ-ray polarization corresponding to the above laser lines.

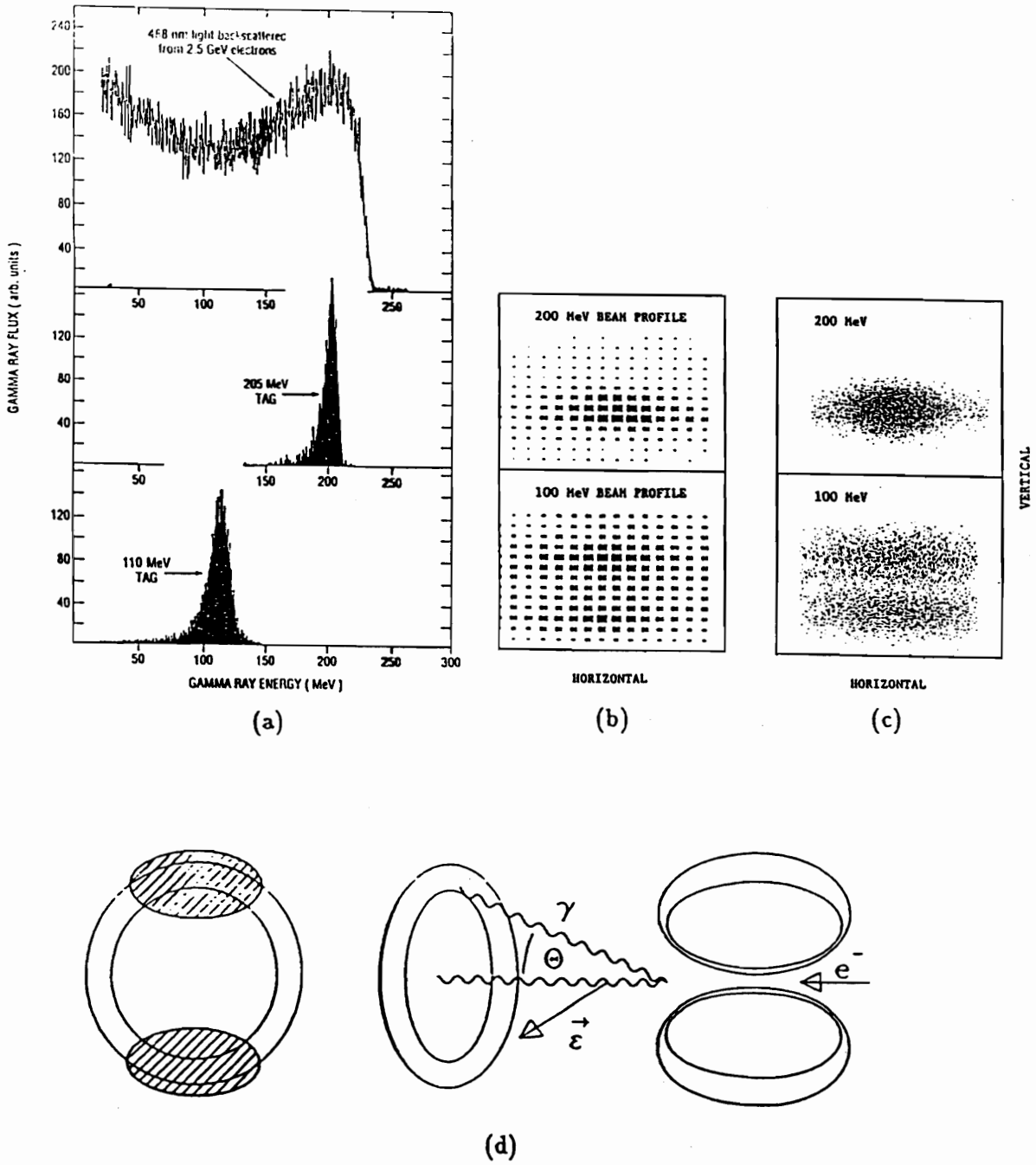

Figure 2-5: (a) The γ-ray spectrum for 488 nm laser light. The upper panel is the untagged spectrum. The middle and lower panels are the spectrum in coincidence with the 205 and 110 MeV TAGs, respectively. (b) The γ-ray beam profile. (c) The results from a Monte Carlo simulation. (d) The effect on the beam spot from kinematic and dynamic aspects.

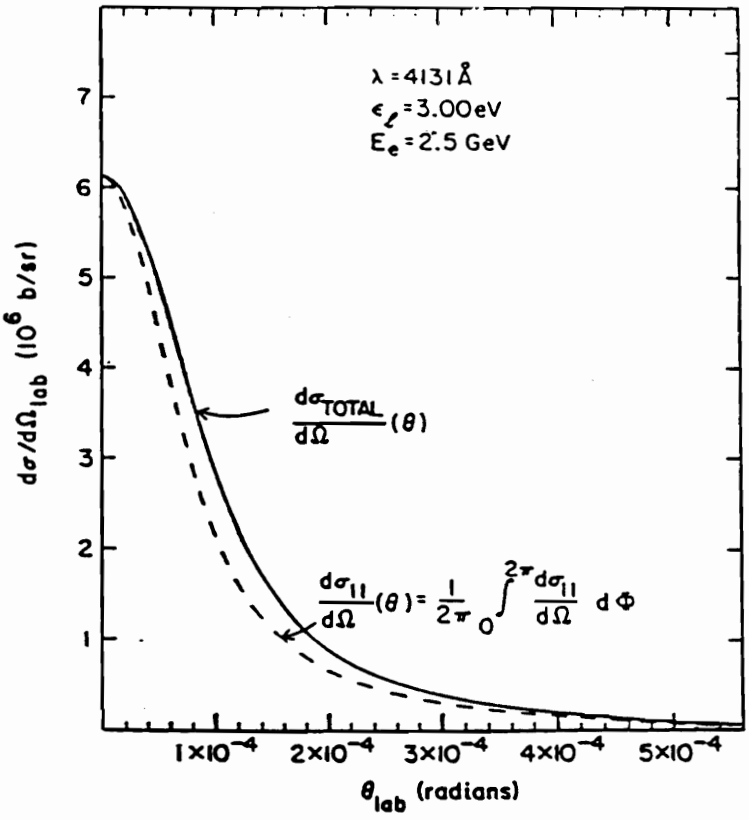

Figure 2-6: Total and parallel backscattering cross sections as a function of the backscattering angle.

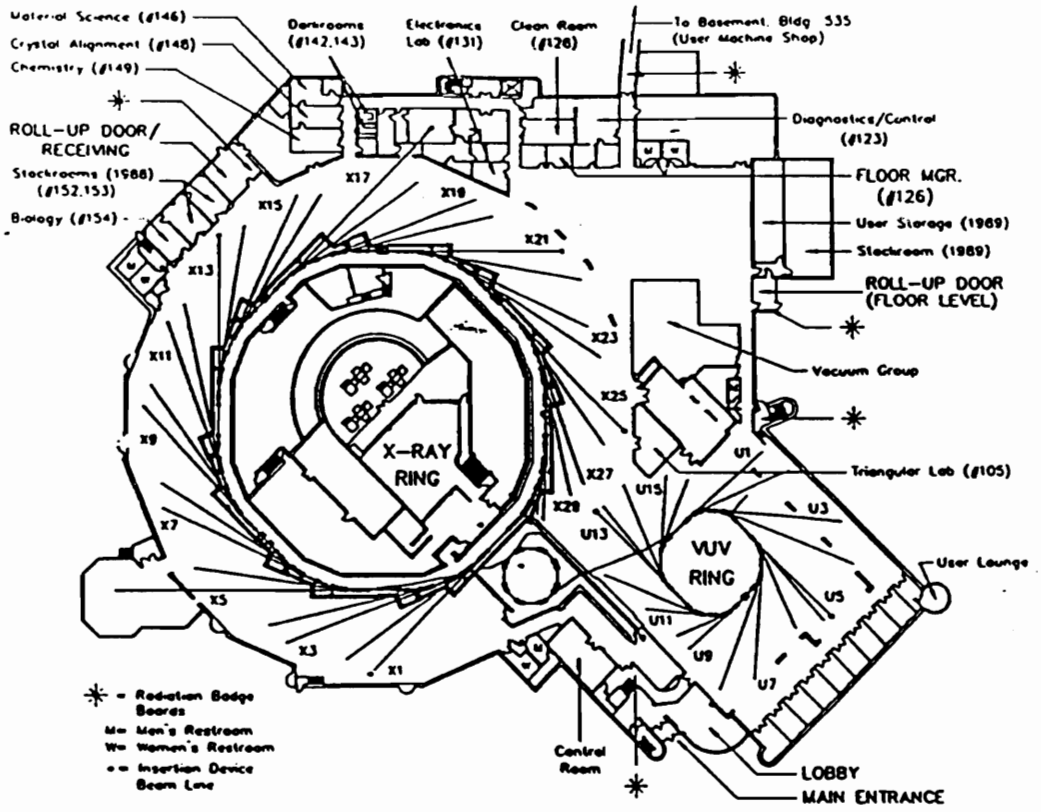

Figure 2-7: Floor plan of the National Synchrotron Light Source.

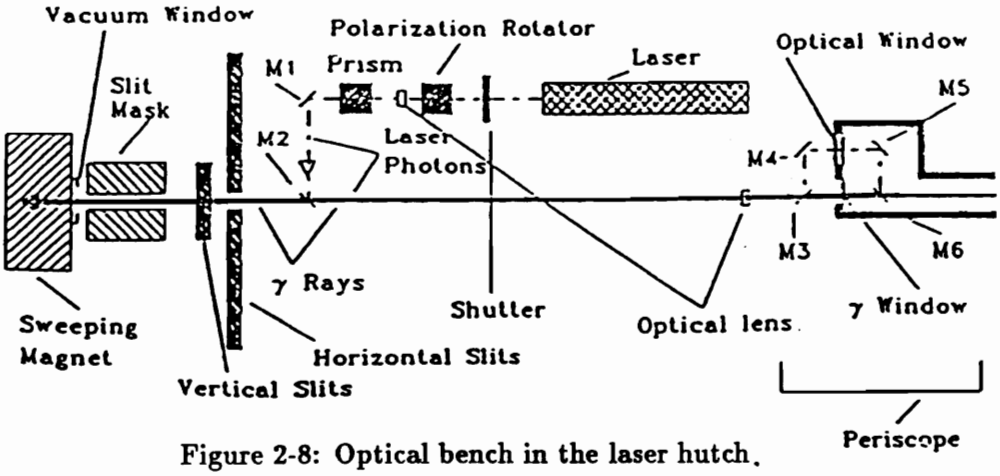

Figure 2-8: Optical bench in the laser hutch.

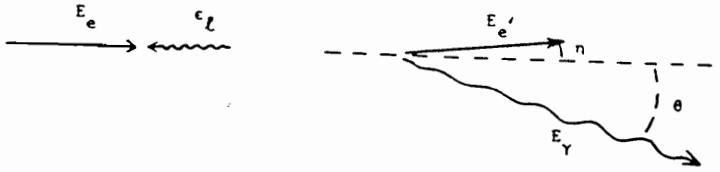

(a)

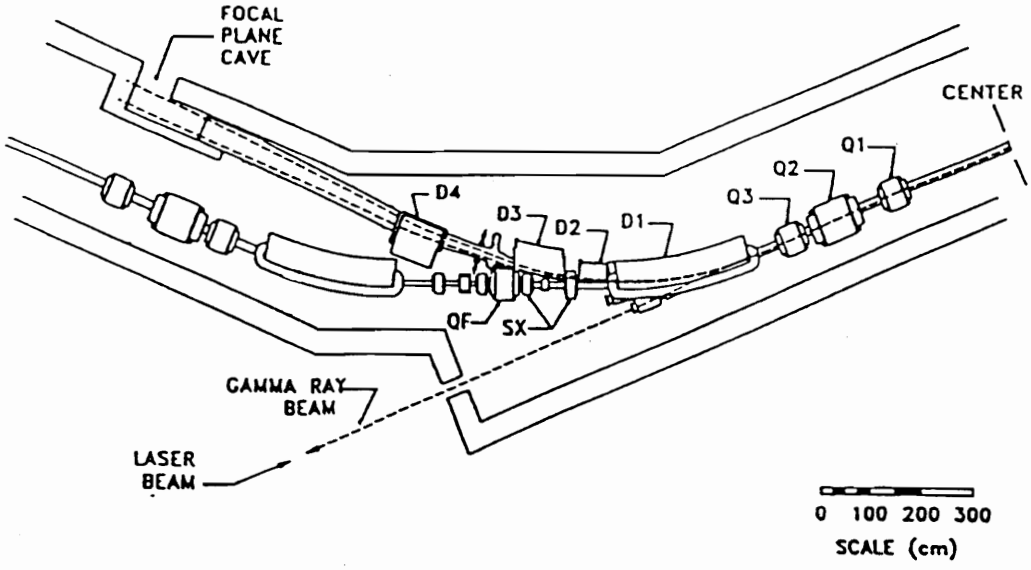

(b)

Figure 2-9: LEGS Tagging spectrometer. (a): The kinematic vectors of the electron photon scattering. (b): The layout of the LEGS tagging system. D1, D2, D3 and D4 are the spectrometer dipole magnets.

Chapter 3

The Set Up of the Proton Compton Scattering Experiment

3.1 The Planning and Set Up Of The Experiment

Since proton Compton scattering is elastic the energy of the scattered photon is uniquely obtained with 4-momentum conservation. The vector diagram of proton Compton scattering is shown in Figure 3-1(a). The energy of the scattered photon as a function of its scattering angle can be written in the lab system as:

$$E'_\gamma = \frac{E_\gamma}{1 + \frac{E_\gamma}{m_p}(1 - \cos\theta)}, \tag{3.1}$$

where E_γ and E'_γ are the photon laboratory energies before and after the proton compton scattering, θ is the photon laboratory scattering angle and m_p is the proton mass. This experiment measured the scattered photon at 90° in the CM system, which corresponds to 76° in the lab system for E_γ = 300 MeV. The corresponding recoil proton angle in the laboratory system is 44°. For an incident energy range from 240 to 330 MeV the corresponding laboratory angles change by only a few degrees. The scattered photon and

proton energies as a function of the incident energy for a recoil proton lab angle of 44° are shown in Figure 3-1(b).

As mentioned in Chapter 1 in this energy region the dominant photon reaction process is pion photoproduction. While charged pion photoproduction can be easily identified and vetoed, π^0 photoproduction, with a cross section about 150 times greater than that of the Compton scattering, cannot be easily distinguished and provides a huge background for this experiment. With a lifetime of $\sim 10^{-16} sec$ the π^0 decays almost instantaneously into two gamma rays. In the π^0 rest frame the two photons are distributed isotropically with the same energy, $\frac{m_{\pi^o}}{2} = 67.5\ MeV$. In the lab frame the decay photons have a continuous range of energies due to the Lorentz boost, and the one going along the π^0 momentum direction will have the largest energy:

$$E_{\gamma_{\pi^0}}^{max} = \tfrac{1}{2}(E_{\pi^0} + \sqrt{E_{\pi^0}^2 + m_{\pi^0}^2}), \tag{3.2}$$

where E_{π^0} is the total energy of the π^0 in the lab frame after production and is given by:

$$E_{\pi^0} = \frac{(E_\gamma + m_p)(2E_\gamma m_p + m_\pi^2) + E_\gamma \cos\theta \sqrt{(2E_\gamma m_p + m_\pi^2)^2 + 4E_\gamma^2 m_\pi^2 \cos^2\theta - 4m_\pi^2(E_\gamma + m_p)^2}}{2((E_\gamma + m_p)^2 - E_\gamma^2 \cos^2\theta)}, \tag{3.3}$$

where θ is the π^0 scattering angle. The highest π^0 photon energy is close to that of the Compton scattered photons, shown as the dotted line in Figure 3-2(a). Since the π^0 mass is relatively small, the recoil proton energy is also close to that of the Compton recoil proton(Figure 3-2(b)).

In the planning of the experiment much effort was made to decrease the π^0 background and increase the separation between the π^0 and the Compton scattering events:

- The Compton scattering kinematics can be determined, in principle, by measuring two kinematic variables. In this experiment six variables were measured. This redundancy helped to distinguish between the two processes.

- Since the decay photon from π^0 production is close in energy to that of the Compton photon, a high-energy resolution in measuring the scattered photon is needed. A high-energy γ-ray spectrometer with a large cylindrical NaI(Tl) crystal, 19″ in diameter and 19″ long, was used. For 300 MeV γ-rays the energy resolution is about 1.6%.
- Seven NaI bars were used to detect the second photon from the π^0 events and, thus, veto part of the π^0 background.

The set up of the experiment is located on the LEGS experimental floor(X5) just outside of the main building of the National Synchrotron Light Source of BNL(Figure 2-1). The set up of the detectors and target is shown in Figure 3-3. The proton target is liquid hydrogen contained in a cylindrical mylar cell located 41 meters from laser backscattering center. The 7 NaI bars to veto part of the π^0 events were placed around the target opposite to the the γ-ray spectrometer. Both the final state photon and proton were detected.

The energy of the scattered photon was measured by the γ-ray spectrometer. The detector was set at 76° laboratory angle to measure the 90° CM Compton scattering. The front face of the spectrometer collimator is 22.7 cm away from the target center. The scattering angle of the recoil proton is measured by drift chambers, from which the scattering angle of the photon can be calculated. Three X-chambers and one Y-chamber were used (Section 4). The first X-chamber was about 25 cm from the target center.

An array of 16 plastic scintillators, called proton bars, was used to determine the time of flight, as well as the energy deposition of the recoil proton. The proton bars were centered at 44° laboratory angle and 391.2 cm away from the target center. In this experiment the recoil proton has relatively small energy. After the energy loss in the target its energy is even smaller. We cannot do much about the energy loss in the target, but the energy loss over the flight path to the proton bars can be reduced. Between the wire chamber system and the proton bars there was a big tent filled with helium gas, which reduced the energy loss and multiple scattering of the recoil proton. A three dimensional view of the set up is shown in Figure 3-4(a).

The following sections describe in detail the detectors used in this experiment. The high energy γ-ray spectrometer is described in Section 2. The target is described in Section 3. The wire chamber system is described in Section 4. The proton bars, and the helium tent are described in Section 5 and the NaI veto bars are described in Section 6. Signal processing and electronics are described in Section 7.

3.2 The High Energy γ Ray Spectrometer

3.2.1 The Important Aspects of the NaI Detector

The small difference in the scattered photon energies of the π^0 and Compton processes requires a high resolution γ-ray detector. In designing a high-performance high energy γ-ray detector three main factors need to be considered [34]. First, a substantial fraction of the showers produced by a γ-ray should be contained within the scintillator. Otherwise, fluctuation of the energy that escapes will dominate the resolution. Second, the light output of the scintillator, the number of scintillation photons produced per unit energy deposited, is crucial to the energy resolution. The statistical fluctuation in the number of photons detected by the phototube imposes a upper limit on the energy resolution that can be achieved. The higher the light output the smaller the fluctuation and the better the resolution. Third, the uniformity in scintillator light generation and in light collection is also an important factor. The generation of light can be strongly affected by the local concentration of thallium dopant and by the presence of other impurities and crystal defects. High-energy γ-rays produce showers in different locations throughout the scintillator volume, and the locations of the showers vary from event to event. The non-uniformities cause fluctuations in the number of photons collected and thus degrade the resolution.

The best candidate for a high-energy γ-ray spectrometer is a NaI(Tl) detector. NaI(Tl) is the most commonly used inorganic scintillator. A small amount of Thallium is added

to NaI as an impurity activator. Compared with organic scintillators NaI has greater stopping power due to its higher density and atomic number. This makes it very suitable for the detection of gamma rays. NaI(Tl) has the highest light output, 230% compared to anthracene, whereas other commonly used scintillators such as CsI(Tl), CsI(Na) and CaF_2 have much lower light outputs, 95%, 150% and 110% , respectively [35].

3.2.2 The structure of the high energy γ-ray spectrometer

The high-energy γ-ray spectrometer consists of the NaI detector, the front detector (the Turtle detector), the annulus and back detectors, and lead shielding. The cross section of the γ-ray spectrometer is shown in Figure 3-4(b). The scattered photon from $\gamma\ p \longrightarrow \gamma'\ p$ has relatively high energy, from 200-270 MeV. The core of the detector, the 19″ by 19″ NaI(Tl), can contain most of the shower. The crystal was built specifically for LEGS by the Bicron Co.[43]. It is very difficult to grow a NaI crystal of such a size. It took about 6 month to grow and evaluate one ingot. Several ingots were processed before a suitable one was chosen. Since NaI is hydroscopic and can be damaged by moisture, the crystal is housed in an air-tight protective enclosure made of aluminum.

The NaI(Tl) crystal is optically coupled to nineteen 3″ phototubes(Hamamatsu R1911). Since the light collection non-uniformity gets drastically worse with increasing phototube diameters, 19 tubes were used instead of one or a few big tubes. These phototubes were individually selected to have uniform responses. These phototubes were gain matched first with a ^{137}Cs gamma source, then with the LEGS γ-ray beam.

Upstream of the front face of the NaI is a plastic scintillator. It is 1″ thick and 23″ in diameter and viewed by six phototubes mounted evenly along the circumference. The phototubes are 2″ Hamamatsu R2049 tubes. This plastic scintillator is called the 'Turtle' detector because of its shape. It is used to veto charged particles entering the NaI detector in this experiment. It could be used to identify particles entering the detector by measuring

their energy loss. The γ-rays entering the spectrometer are collimated by a lead collimator. It is in front of the 'turtle' and has a circular openning of 20.76 cm.

The NaI crystal is surrounded by 12 plastic scintillators, called the 'annulus' scintillators. They are used to veto the events where some of the shower energy leaks out of the crystal, as well as to veto cosmic ray events. Each 'annulus' scintillator has a square cross section of 4″ width by 37″ length, and is coupled to a 5″ Hamamatsu R1650 phototube at the downstream end. The back of the NaI crystal is covered by another plastic scintillator called the 'back' scintillator. The 'back' scintillator is a cylinder with 18″ diameter and 4.5″ thickness. It is optically coupled to a single 9″ Amperex DVP60 phototube. It is used for veto and does not need to have good energy resolution.

3.3 The Proton Target

The target in this experiment is liquid hydrogen which is commonly used as proton target. The molecular and atomic binding energy between protons is very weak and can be completely neglected. Liquid hydrogen is contained in a mylar cell, which is a cylinder of 65 mm diameter and 130 mm length. The target cell is shown in Figure 3-5(a). The thickness of the mylar wall is 0.127 mm. At its two ends there are two curved end caps; each of them has a 18 mm overlap with the cylinder.

The target cell was surported from the top by the supply and ventilation tubes. The cryogenic refrigerator was placed on a stand about 80 cm above the target. Gaseous hydrogen was cooled down below the boiling point (20.1 K at 1 atm). The liquified hydrogen went down the supply pipe into the target and the evaporated hydrogen gas rose up through the ventilation tube to the cryogenic refrigerator. There is a resistor sensor at the top inside the target cell, which serves as a hydrogen level monitor. When the liquid hydrogen level dropped below the resistor, its resistance increased. This was reflected on the monitor board and proper measures were taken to correct the situation.

3.4 The Drift Chamber System

Multiwire proportional chambers (MWPC), invented in 1967 by Charpak, are widely used in nuclear and particle physics to determine the trajectory of charged particles. Better spatial resolution can be obtained with drift chambers which have a slightly different design from MWPC [35]. Drift chambers can measure the drift time of the electrons from ionization to the anode wires. The drift distance to the anode wire can be obtained if the drift velocity is known.

Compared with plastic scintillators, drift chambers are more complicated and difficult to maintain. When first planning the experiment a plastic scintillator hodoscope was considered to measure the scattering angle. A Monte Carlo simulation code was written to simulate the plastic hodoscope. After comparing different designs it was found that, for a reasonable number of plastic bars and scintillator size, the angular resolution of a plastic hodoscope could not meet the needs of the experiment. Thus, drift chambers were finally chosen to measure proton scattering angles.

Two types of drift chambers were used in this experiment, X-chambers and Y-chambers. Three X-chambers were used to measure the coordinates in the horizontal plane, which requires good spacial resolution. One Y-chamber was used to measure one of the Y coordinates, while another Y-coordinate was measured by a proton bar.

The chambers used in the experiment are hexagonal. One layer of the wire plane has 16 anode wires and 16 cathode wires, shown in Figure 3-5(b). The anode wires and cathode wires are alternatively placed at a distance of 8.25 mm, and the distance of a cell is 16.5 mm. Each anode (sense) wire is made of gold-plated tungsten and has a diameter of 20 μm. Each cathode (field) wire is also made of gold-plated tungsten, but has a larger diameter of 100 μm. The tension in the sense and field wires is $2.39 \times 10^3 kg/cm^2$ and $4.14 \times 10^2 kg/cm^2$, respectively, which are about half of the material yielding tension.

An X-chamber consists of two layers of wire planes. The two planes are identical but the second plane is rotated 180°. The wires in a plane are offset by a quarter of a cell from the center of the hexagon (Figure 3-5). An offset of half a cell results from the rotation, so that the field wire of the second plane is right behind the sense wire of the first plane. The distance between chambers is about 6 cm.

The chamber gas was a mixture of 85% argon and 15% butane. Argon was used because it requires the lowest electric field intensities to form an electron avalanche. Butane was used as a quenching gas to absorb the radiated photons from de-excitation of Ar atoms, and then dissipate this energy through dissociation or elastic scattering.

The chamber frame is made from G10 board (glass-epoxy) with printed circuit on it. The wires were soldered on the circuit. The sense wires are grounded and the field wires are at a negative high voltage of -2100 V. On both sides of the wire board, there was a layer of G10 board glued with aluminized mylar of 6 μm. The two aluminized mylar planes are at a negative high voltage of -1900 V which, together with the cathode wires, define the drift field. The field is not uniform; it is highest near the sense wire and smallest near the field wires. The signals from the wires are processed by a LeCroy card, consisting of 16 channels of pre-amplifier followed by discriminators. The signals from the LeCroy card go through delay repeaters to TDCs.

3.5 The Proton Bar Detector(P-bars) and the Helium bag

The P-bars consist of 16 plastic scintillators for determining the time of flight and energy deposition, as well as the Y position of the recoil protons (Figure 3-6(a)). They were placed in a vertical plane 4 meters away from the target center. Each scintillator is $10\,cm \times 10\,cm \times 160\,cm$ (Figure 3-6(b)). The space between two adjacent bars is 8 mm. Both ends of each bar are optically coupled to a phototube. Each bar is wrapped with two layers of aluminized mylar.

The P-bars were gain matched with cosmic rays, since the energy deposited in the bar from cosmic rays was close to that from the recoil protons. Cosmic rays are essentially muons created by high-energy protons in the showers in the atmosphere. Most muons reach the minimum ionizing energy region at sea level. Cosmic rays went through the bars in all directions, but most of them penetrated the bars perpendicularly. The energy spectrum from cosmic rays had a peak at energy $E_{bar} = 20MeV$. In the gain matching the high voltage on each phototube base was adjusted so that all the peaks from different bars were at the same channel.

Since the recoil protons have very low kinetic energy, a helium bag was placed between the drift chambers and the P-bars (Figure 3-6(a)). The length of the helium bag is 3 meters. The pressure in the bag was slightly above that of the atmosphere. The energy loss in the helium gas is about four times smaller than that in the air. The helium bag minimized the energy loss as well as multiple scattering in flight.

3.6 The NaI Veto Bars

Seven NaI bar detectors were used to veto the π^0 events when one of the decay photons entered one of the bars. Two bars were placed horizontally; on top of which three were placed vertically. Two others were placed around the drift chambers (Figure 3-3). Each bar has dimensions of $9.8\,cm \times 9.8\,cm \times 35.5\,cm$. A phototube was mounted on one end of each NaI bar. The signals from these bars only go to registers since the energy deposition in the bars was not needed.

3.7 Signal Processing and Electronics

Next to the target and detector area is the signal processing room. Here most of the electronics and a VAX computer are stationed (Figure 2-1). Most of the signal processing was done

with standard NIM and CAMAC modules. A few non-standard modules made at LEGS were also used. The signal processing logic diagram for this experiment is shown in Figure 3-7. Since various detectors used a large number of Analog to Digital Converters(ADC), Time to Digital Converters(TDC), and Coincident Registers(CR) (47 ADCs, 128 TDCs and 30 CR just for γ-ray spectrometer, P-bars and drift chambers), high density CAMAC modules such as 16 channel FERA ADC(LR4300), 16 channel TFC(LR4302) (together with a FERA ADC, it functions as a TDC.), and 48 channel Coincidence Register(LR4434) were used.

The trigger for the experiment was a coincidence between the 19″ NaI (above $\sim$ 100 MeV) signal, the tag signal and the computer not-busy signal. The trigger was very simple because other coincidences, such as the coincidence between scattered γ-ray and recoil proton, and the vetos were performed in software. Since the NaI pulse has a relatively long rise time, about 100 ns, a Constant Fraction Discriminator(CFD) was used to reduce the time jitter. The trigger signal, after the CFD and CRs, was later than the signals from the plastic scintillators and the drift chamber. This caused much difficultie in the timing of various signals. It was necessary to delay all other signals except the trigger. Since the delay ribbon cables needed for the drift chambers were too long and signals might be lost because of dispersion, special modules called 'repeaters' were built to amplify the signals after a certain length of delay (about 60 feet).

The pulse height of the 19″ NaI was measured by a wide gate ADC(LR2249W) after the pulse was clipped to about 300 ns. The signals from the Turtle, Back and Annulus were split into two branches after delays. Signals from one branch were recorded by registers; the others were converted into ECL signals and measured with FERA ADCs. The signals in the 'turtle','annulus' and 'back' were used during replay to veto the events with energy leaking out of the 19″ NaI.

The P-bars had 16 signals on each side, and signals from both sides were processed in the same manner. Each signal was split into two. One signal, after discriminator(LR4413, 16

channel) and repeaters, was used to stop the TDC. The TDCs were started by the event trigger. The pulse height of the other signal was measured by FERA ADCs.

The three X-chambers each had 32 signals and needed 6 sets of 16 channel FERA TDC modules to measure the drift time. Each pulse was processed by a preamplifier-discriminator card connected directly to the chamber, delayed by three sets of repeaters and ribbon cables, and then used to stop the FERA TDC, which was started by the trigger. The signals from the Y chamber, instead of going to the TDC, were recorded by a CR since high angular resolution in the azimuthal angle was not needed. The signals from the NaI bars, after proper delay and discrimination, were simply recorded by a CR. During the whole experiment, the deadtime rate is about 2%.

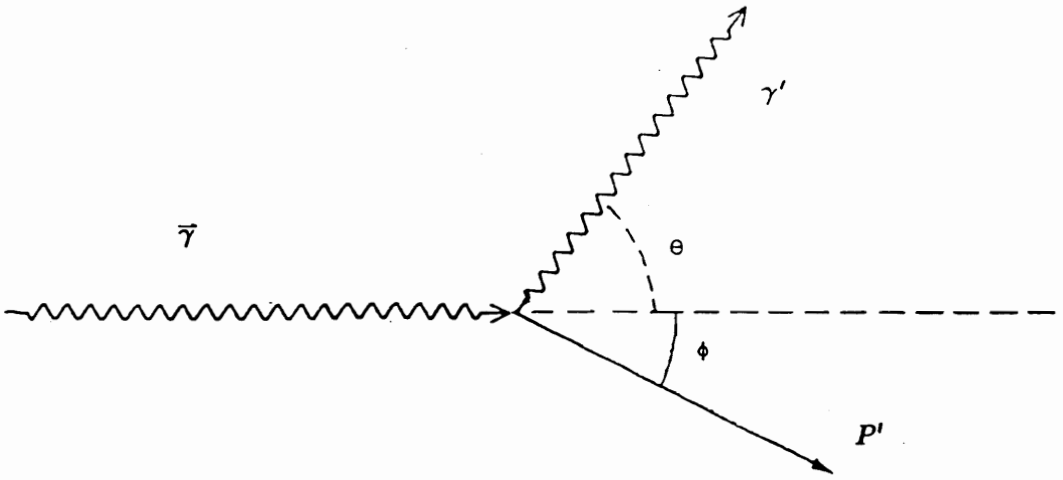

(a)

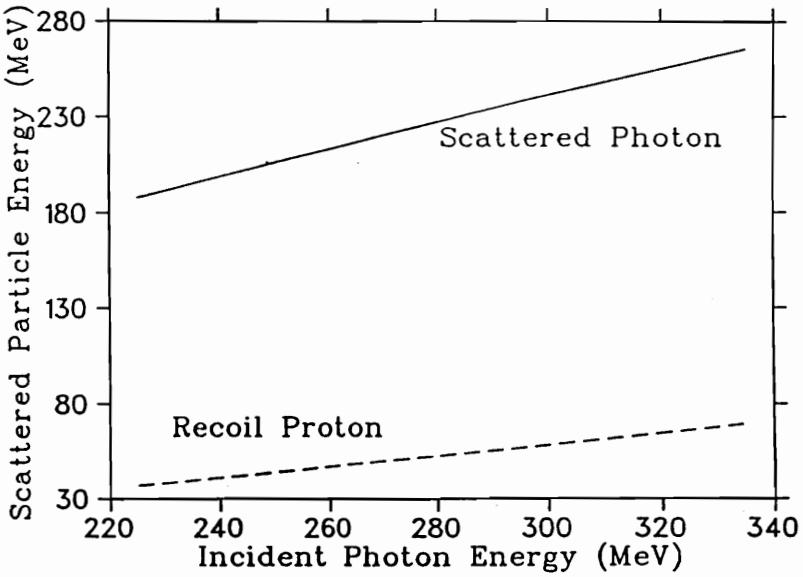

(b)

Figure 3-1: (a) The vector diagram of the proton Compton scattering. (b) The scattered photon and recoil proton energy as a function of the incident γ-ray energy at fixed recoil proton angle (45° Lab).

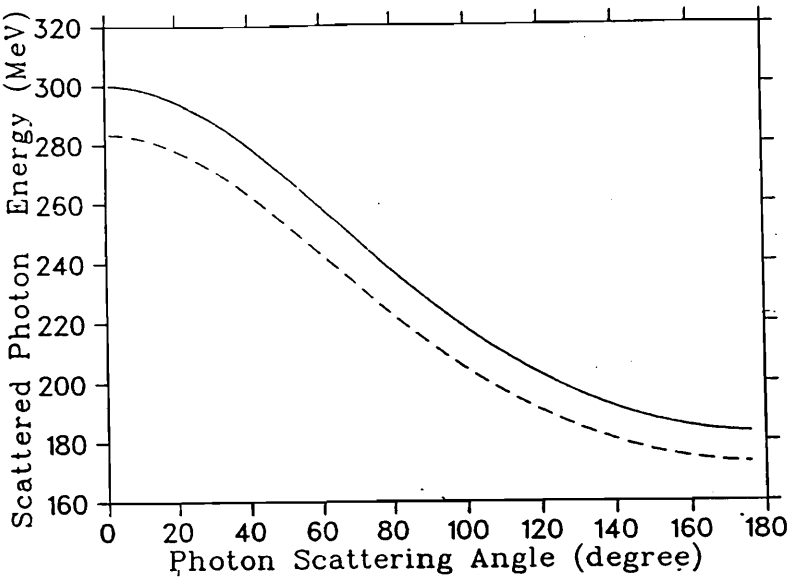

(a)

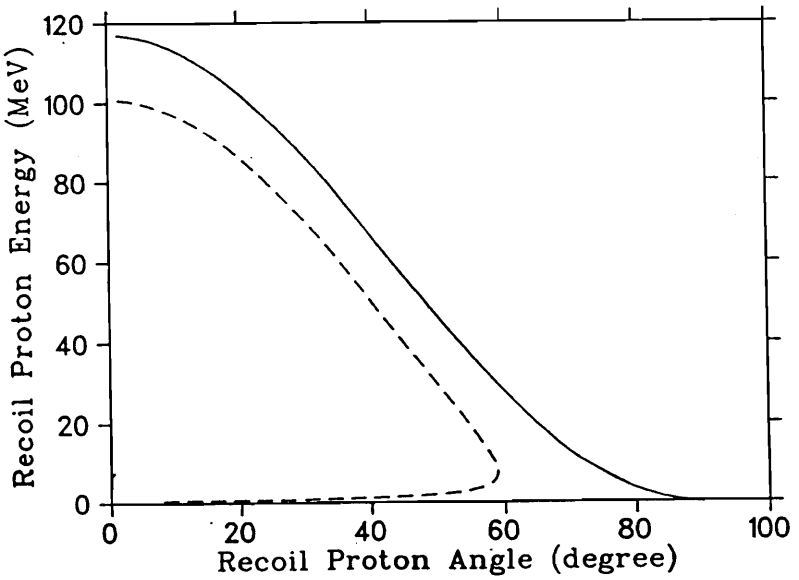

(b)

Figure 3-2: (a) The scattered photon energy as a function of scattering angle with fixed incident photon energy (300 MeV). The dashed line is for the maximum energy gamma from π^0 decay in π^0 photoproduction. (b) The recoil-proton energy as a function of scattering angle with fixed incident photon energy (300 MeV). The dashed line is for the π^0 production.

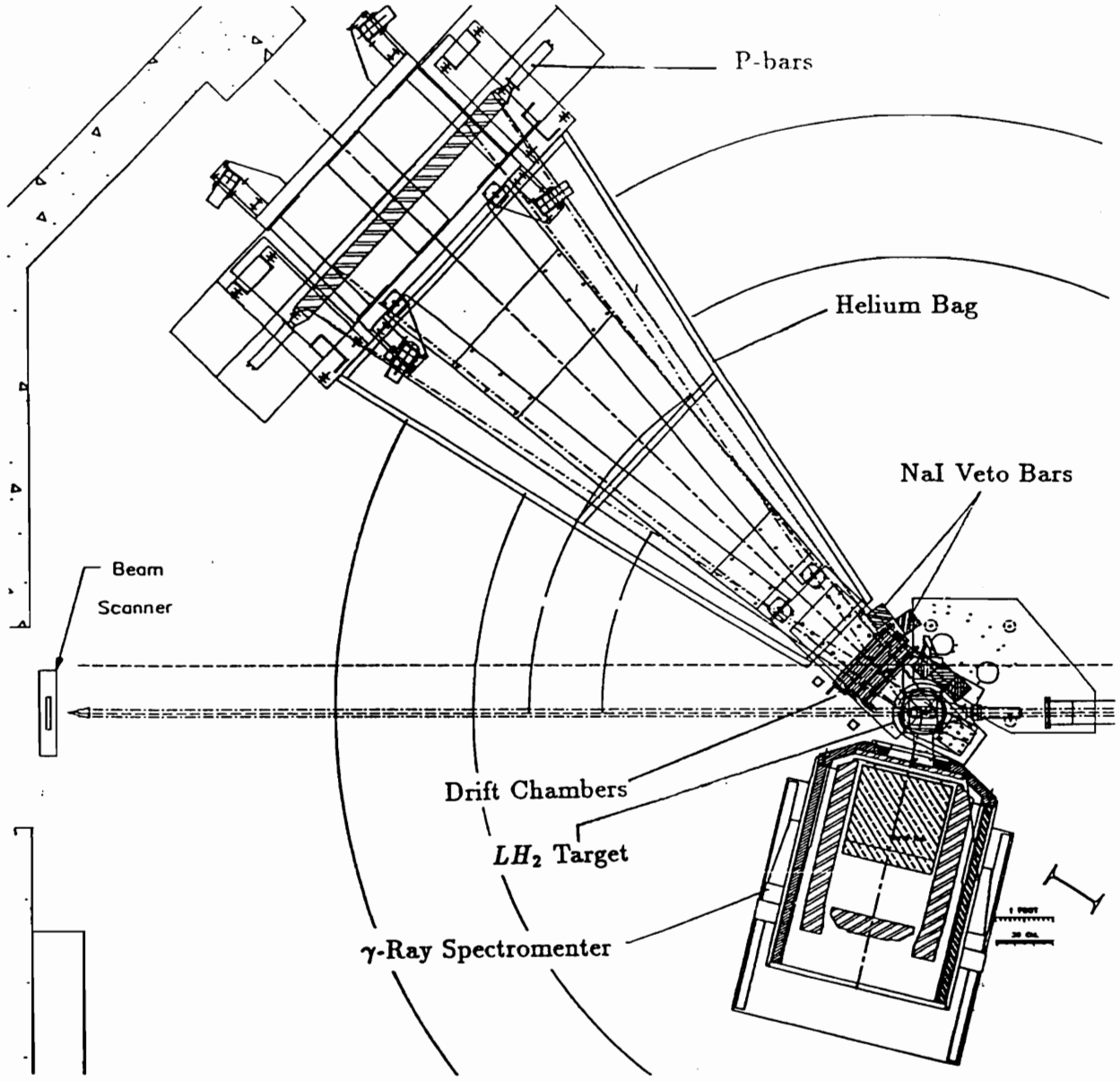

Figure 3-3: The top view of the experimental set up. The γ-ray beam comes from the right.

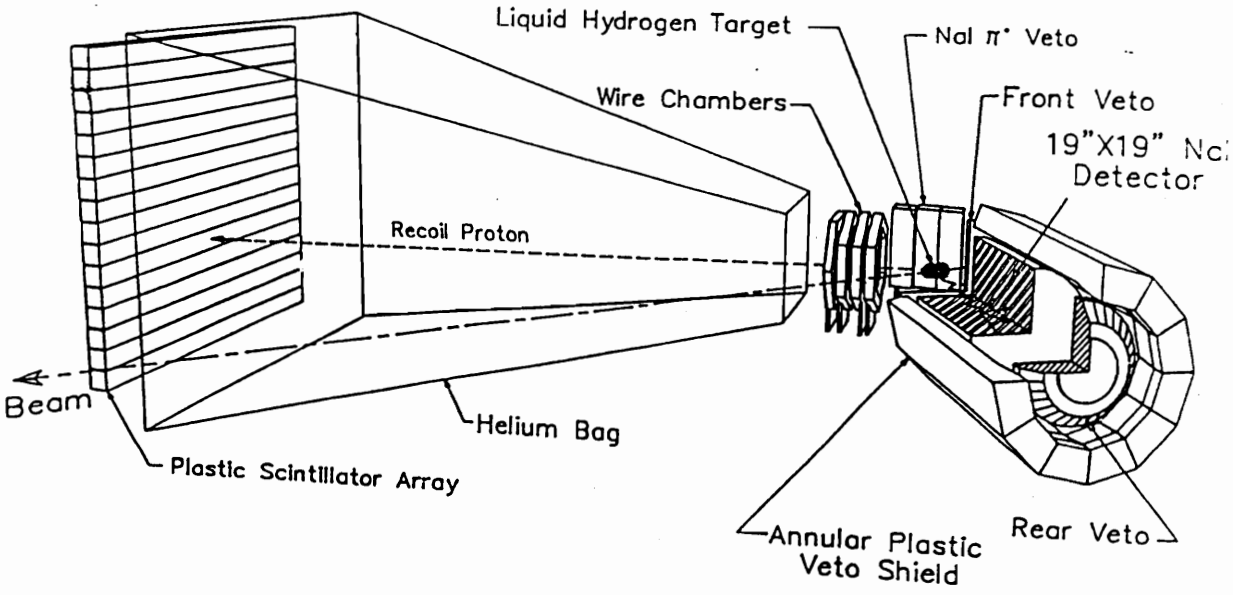

(a)

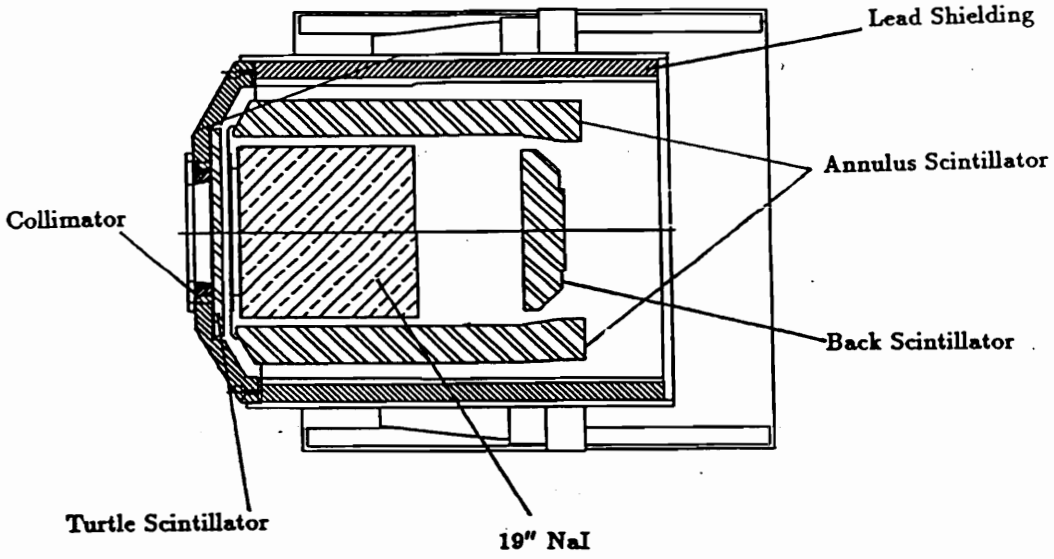

(b)

Figure 3-4: (a) The three dimensional view of the experimental set up. (b) A cross section view of the high energy γ-ray spectrometer (phototubes are not shown). It was placed on a stand which could move around the target.

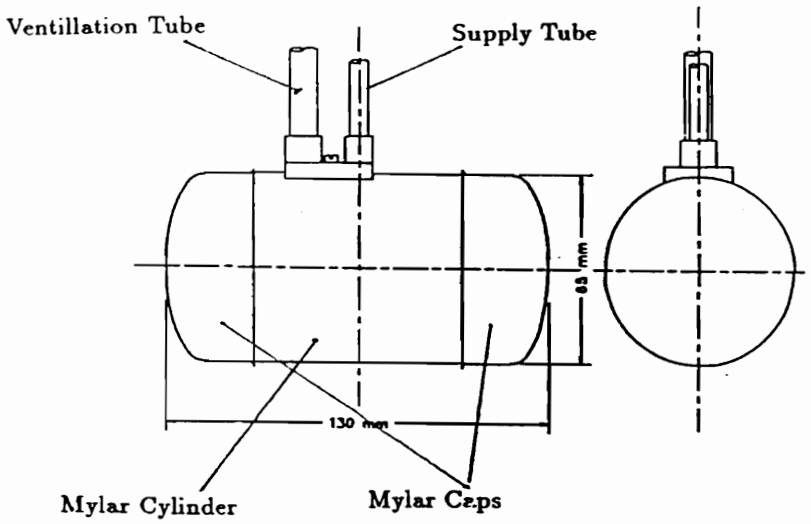

(a)

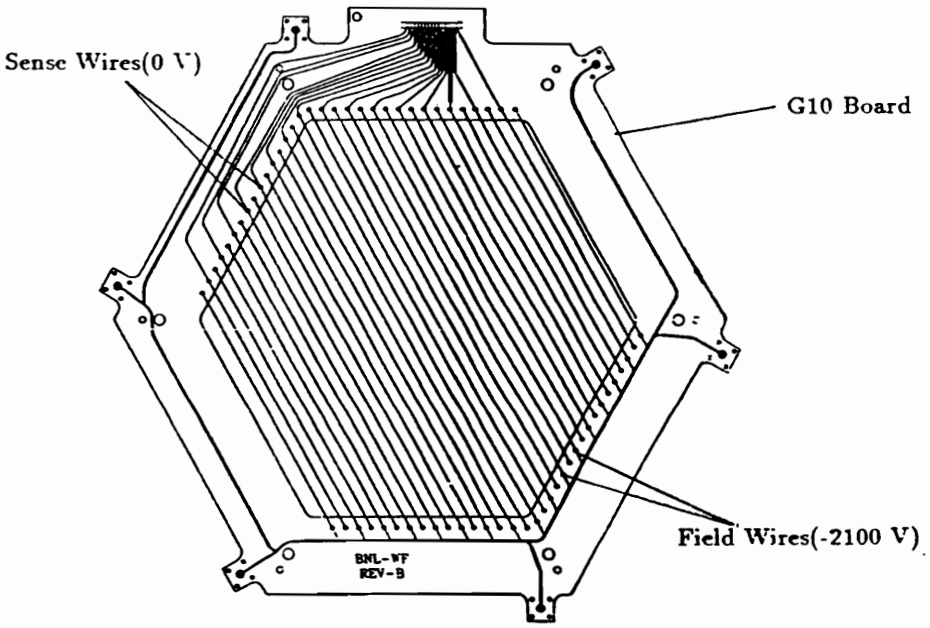

(b)

Figure 3-5: (a) The liquid Hydrogen target cell. (b) The drift chamber wire plane. Both the X-chamber and the Y-chamber used the same wire-plane design.

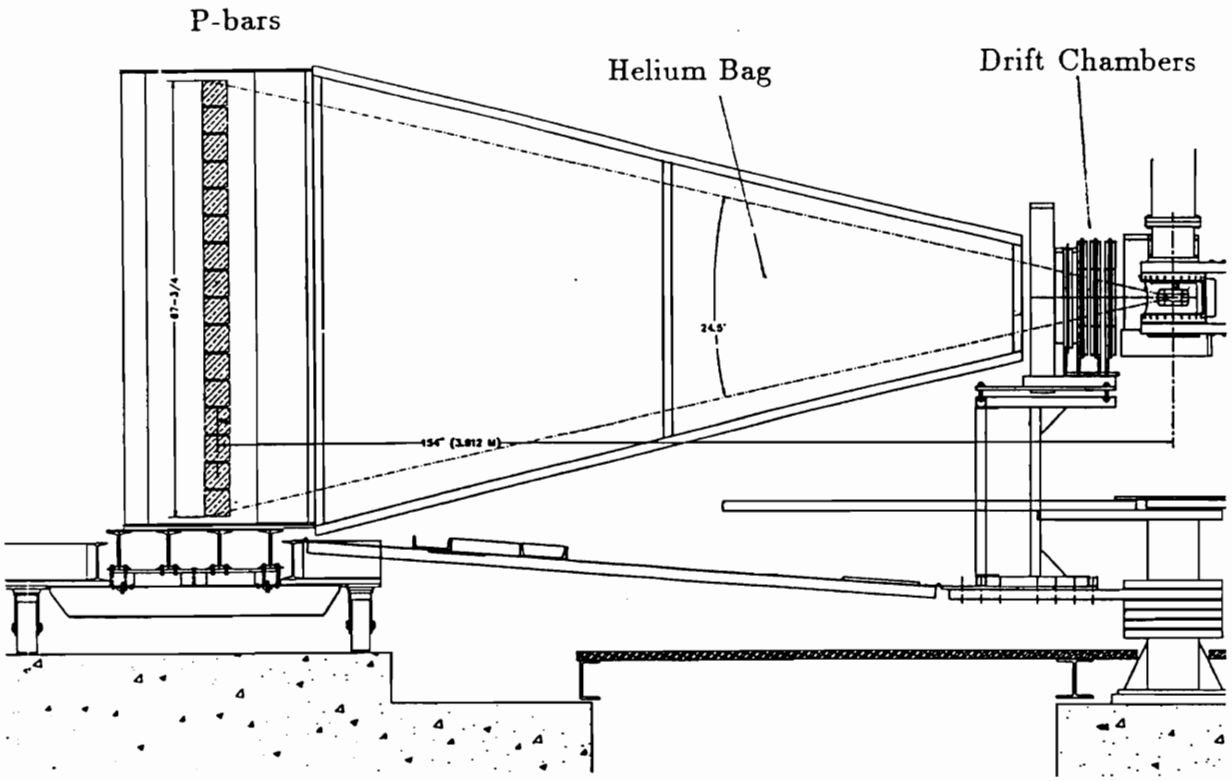

(a)

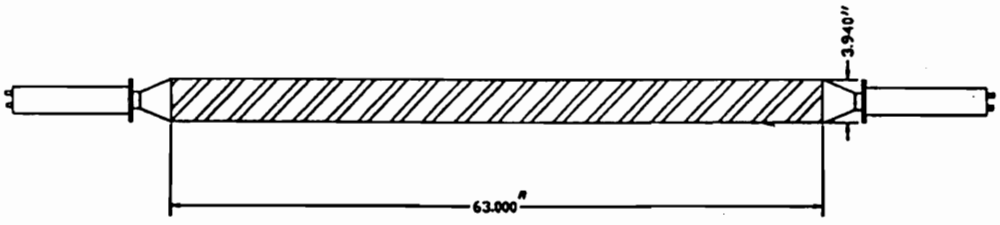

(b)

Figure 3-6: (a) A vertical view of the drift chambers, Helium bag and proton bars. (b) A proton bar with phototubes at both ends.

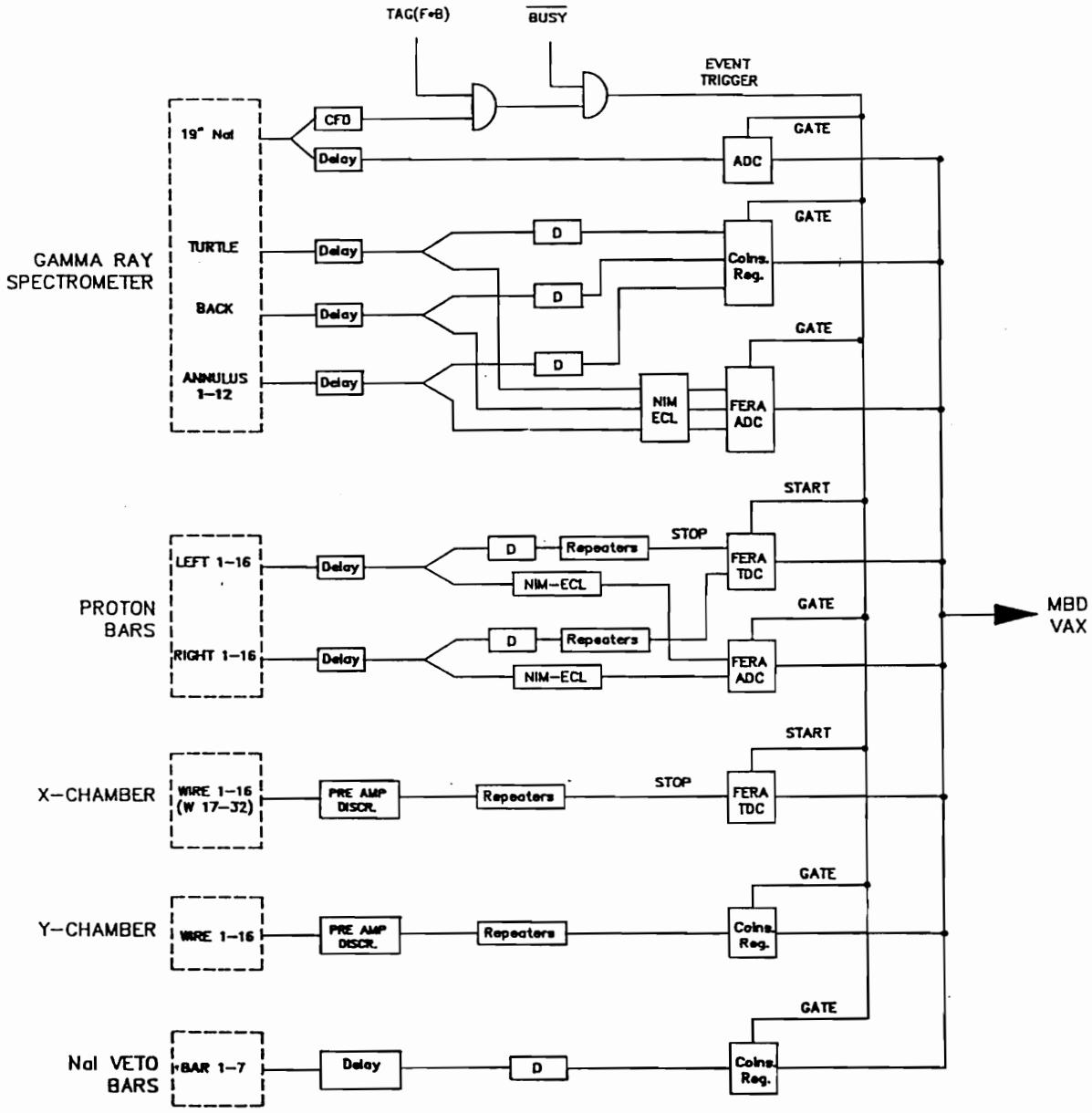

Figure 3-7: The electronics logic diagrams for the proton Compton scattering experiment.

Chapter 4

Data Aquisition and Analysis

4.1 Data Aquisition

4.1.1 Data Collection

The preparation of the proton Compton scattering experiment was completed in February of 1993. The data collection of photon scattering at 90° CM started on Feb. 12 and ended on April 31. During the data taking some the raw data were histogrammed on line. They were checked frequently to make sure detectors and electronics were functioning properly.

During the runs the gamma-beam spot was set to 27×40.5 *mm*. The beam spot was set near the target edge at the P-bars side in order to minimize the energy loss in the target. The nickel slits setting was 12×18 *mm*. The electron-beam current was between 110 and 250 mA with a partial lifetime of about 16 hours. The laser power was set to about 3.6 watts.

In the data replay different approaches were tried for the calibration of the drift chambers and P-bars before the procedures were finalized. The same held true for the separation of

the Compton events from the background. Sections 2 to 5 describe the final calibration procedures for the detectors and the proton energy loss. Sections 6 and 7 describe the particle identifications and separation of the Compton events from the background. Section 8 describes the empty target subtraction.

4.1.2 Data Aquisition System

The data aquisition system, Q, developed at the Los Alomos National Laboratory, was used in this experiment. Q is a general purpose data aquisition system mainly for nuclear physics experiments. This system acquires data from a CAMAC, supplies the data for each event to the analyzer for processing and allows keyboard control of the experiment. An analyzer specific to this experiment was written to carry out the online analysis.

Q includes provisions for histograming, data testing and dynamic parameter inclusion. The histogram subsystem can create, increment, display, and save one and two dimensional histograms. The data testing subsystem can execute sets of arithmetic and logical tests to apply to the data. The coincidence of the scattered photon and proton and the many vetos in the experiment were done with the data testing system, which greatly simplified the trigger logic. The dynamic parameter array subsystem provides a way to alter the values of parameters in the analyzer without stopping and re-editing the analyzer.

The Q system was used for data replay as well. A comprehensive analyzer was written for the data replay. Many utilities and subroutines are available with the Q system. The Histogram EDiting system(HED), Monte Carlo program GEANT and the PLOTDATA graphic packages were also used in the data analysis.

A micro-VAX computer, located in the electronics room was used for the data aquisition and experimental control. Another micro-VAX and three faster VAX workstations (two VAX-4000s, one VAX-3100) were used for the data analysis. All these computers were linked together to form a local network.

4.2 Calibration of the γ-Ray Spectrometer

The high energy γ-ray spectrometer was calibrated with the LEGS γ-ray beam. During the calibration the flux of the beam was reduced by turning down the laser power in order to avoid damage from excessive current in the phototubes and to avoid pile up in the computer. Monochromatic γ-rays were used by turning on only one or two tagger channels. The trigger required γ-ray events in the spectrometer in coincidence with the tagger. Short runs with different γ-ray energies were taken to obtain enough points to get the correspondence between the spectrometer ADC channels and the γ-ray energy deposited in the NaI. These points were fitted with a polynomial (Figure 4-1). The γ-ray energy as a function of the ADC channel number is given by $E_\gamma = a + bx + cx^2$, where x is the ADC channel number, E_γ is in MeV, $a = 132.25$, $b = -2.6367 \times 10^{-2}$, and $c = 1.2898 \times 10^{-4}$. The statistical errors for the points used to obtain the calibration are negligible.

4.3 Calibration of the Drift Chambers

4.3.1 Drift Chamber Plane Efficiency

The efficiency of a drift chamber is a function of the high voltages applied on the field wires and the foils. The efficiency of each plane in a chamber was measured at different voltages to find the efficiency plateau. Accordingly, the drift chamber operation voltage was determined. A plastic paddle of 3″ by 3″ was placed in front of the chamber to count the particles passing through the chamber. The plane efficiency is defined to be the ratio of the number of particles triggering a particular chamber plane to that passing through the chamber. The results are shown in Figure 4-2(a). The field wire voltage required is 1.13 times the foil voltage. The plateau for other planes are similar. It can be seen that efficiency reaches the maximum at foil voltage below 1900 V. Because the operation voltage

could not be set right on the edge of the plateau, it was chosen as -2100 V for the field wire and -1900 V for the foils.

4.3.2 Drift Velocity

In order to get the spacial information about a charged particle, precise knowledge of the the drift velocity is necessary in addition to the drift time. The drift velocity of the electrons from the ionization is a function of the electric field E and differs for different gas mixtures and pressures [35]. When the gas mixture and pressure are fixed, the drift velocity is a function of the distance from the sense wire. For the present chamber structure the distance between field and sense wires (8.25 mm) is more than four times greater than the distance between the sense wire and foil. Thus the electric field between the sense and field wires is quite non-uniform and it is difficult to calculate the drift velocity accurately.

The drift velocity can be obtained, in principle, by calibrating the chamber with a very narrow electron source with enough energy to penetrate the whole chamber. However, such a source is not available at LEGS. A unique way was found to obtain the drift velocity by utilizing the online nuclear event data. The recoil protons from Compton scattering and π^0 reactions went through all the chambers. Due to geometrical constraints the proton flux passing through the center of the chamber was the largest. Across the distance of the size of a cell, which is relatively small, the proton flux is approximately constant, $dN/dx = k$. Because all the drift chambers were under the same condition, the drift velocity should be the same for all the cells in a plane and for all chambers. Therefore, the protons going through the center cells can be used as a uniform source for calibration.

The TDC spectrum from a center wire is shown in Figure 4-2(b). The x axis is the TDC channel number t_{ch} which is proportional to the relative drift time t, $t_{ch} = gt$, where g is the channel–ns conversion coefficient. The y axis is the number of counts per TDC channel, $\frac{dN}{dt_{ch}} = \frac{1}{g}\frac{dN}{dt}$. The left edge in the TDC spectrum corresponds to events passing very close

to the sense wire which have almost zero drift time. The corresponding time, t_0, is the time offset and is subtracted from the relative drift time to obtain the real drift time. The right edge corresponds to events going very close to the field wire and, thus, having the longest drift time. In the case of constant drift velocity the TDC spectrum should be a step function. The spectrum in Figure 4-2(b) is far from a step function because of the non-uniform drift field. Since the drift time t has a one-to-one correspondence with the drift distance x, the number of counts dN within drift time of $dt = t_2 - t_1$ can be expressed as: $dN = k(x_2 - x_1)$ and thus:

$$\frac{dN}{dt} = \frac{k(x_2 - x_1)}{t_2 - t_1} = k\frac{dx}{dt} = kv \ , \tag{4.1}$$

where v is the drift velocity. The drift velocity is proportional to $\frac{dN}{dt}$ and can be easily obtained from the TDC spectrum. The ultimate relation needed is the drift distance as a function of the drift time, which can be obtained by integration:

$$x = \int_{t_0}^{t} \frac{1}{k}\frac{dN}{dt}(t)dt \tag{4.2}$$

where t is the drift time and k is the flux density across the chamber, which can be obtained by dividing the total number of counts at the wire by the cell distance 16.5 mm. The drift distance in a cell as a function of drift time is shown in Figure 4-3(a).

4.3.3 Track Reconstruction

After the positions at the six drift chamber planes were calculated, these points were fitted with a straight line by minimizing χ^2. The χ^2 fitting also helped to resolve the left-right ambiguity of each position obtained from the drift time, *i.e.* , the real position can be either to the left or right of the sense wire. For each event χ^2 of the fittings for both of the positions were calculated and the ones with minimum χ^2 were chosen.

The distribution of χ^2 for different events is shown in Figure 4-3(b). The spatial resolution of the chamber system is estimated to be 250 μm. The angular resolution for the proton

recoil angle is estimated to be 0.1°. The target image was reconstructed by the track retracing. The empty target image from the γ-ray interception in the beam direction is shown in Figure 4-4 with the wire chamber centered at 80°. The target cell walls, the vacuum window and the protection tent walls are clearly seen. Since the drift chambers were centered at 44° for Compton scattering, after projecting to the beam direction, the target walls and vacuum window walls were less clear.

4.4 Energy Loss of the Recoil Proton

The energy loss of the recoil proton was appreciable since the proton energy was relatively low and an extended LH2 target was used. A good estimation of the energy loss was needed for the kinematic calculations. To achieve this the incident gamma-ray energy, the proton-recoil angle and its traversing thickness in the medium must be known. The incident gamma energy and the recoil angle were well determined. The traversing thickness of the proton outside the target was accurately measured. However, the gamma-proton reaction point inside the target cannot be obtained. Even with event retracing the reaction point still can only be confined along a straight line through the target.

In the analysis the crossing point of the event retracing straight line and the vertical plane through the beam center was assumed to be the reaction point. This was equivalent to using the average traversing distance in the target and, thus, introduced an uncertainty in the energy loss. This uncertainty prevents an accurate energy loss estimation in the target. A narrow beam spot can reduce the uncertainty. A set of data, called 'narrow slits' data, was taken with a smaller beam spot, 22.5 mm wide and 20.25 mm high. The width of the narrow slits is about half of that of the normal slits and corresponds to a smaller uncertainty. This set of data was used for the calibration of the ADC and TDC of the P-bars. The Bethe-Bloch formula was used for the energy loss calculation[37], since it is suitable in the energy range of this experiment. For the narrow slits the average energy loss in the target for different incident energies and recoil angles is shown in Figure 4-5.

After leaving the target the recoil proton traversed the vacuum window, protection tent wall, various layers of the drift chambers and the helium tent. Since the proton energy was very low when it arrived at the P-bars, the helium tent walls, the two layers of the P-bar wrapper and the dead layer of the bar resulting from the machining heat, were also taken into account in the calculation. The traversing thickness, different for different recoil angle, was calculated for each event. The proton energy deposited in the bar and the time of flight (TOF) of the proton were then calculated for each event.

4.5 Calibration of the Proton Bars

4.5.1 The Proton Bar ADC calibration

In the preparation of the experiment, a rough gain match of the P-bars was done with cosmic rays. In the data analysis a detail energy calibration was done with online data. The background π^0 photoproduction was employed to make the calibrations. Compton scattering events are negligible in the calibration, since they are only about 0.6% of the π^0 events. In both the ADC and TDC calibrations the protons going into the center of the bars, with proton recoil angle from 43° - 45°, were used.

In an event the ADC channel number C of the P-bars is proportional to the energy deposition E in the bar. Because the bar is long (160cm), the light absorption in the bar is not negligible, so $C \propto Ee^{-\lambda x}$, where λ is the absorption coefficient of the scintillator and x is the distance from the particle entering point to the tube. In order to get better energy resolution the ADC channel numbers at both ends are needed to be combined. A straight forward way is to sum up both pulse heights, but the sum has a dependence on the entering point, since $C^A + C^B \propto E(e^{-\lambda x} + e^{-\lambda(L-x)})$, where C^A and C^B are the channel numbers for the A and B sides and L is the bar length. The A and B sides refer to the left and right side of the bars viewed from the target, respectively. A better way is to use the square root

of the product of C^A and C^B, $\sqrt{C^A C^B}$, since it has no dependence on the entering point: $\sqrt{C^A C^B} \propto (Ee^{-\lambda x} Ee^{-\lambda(L-x)})^{\frac{1}{2}} \propto E(e^{-\lambda L})^{\frac{1}{2}}$.

The above relation is for the case when there is no ADC offset between the two ends. So the ADC offsets of each bar needed to be determined and subtracted. The bar ADC offsets result from the differences in the response of tubes and from different pedestals of the ADC modules. The A-side ADC channel of each bar was plotted versus that of the B side. Figure 4-6(a) is the plot for bar 8. The events form a straight band, which shows that the responses of the tubes are linear. The band was divided into many slices and the centroid of each slice was found. The ADC offset for this bar was accurately obtained by fitting the centroids with a straight line (Figure 4-6(b)). The offset of the straight line a is the ADC offset. The difference of the slope b from 1 shows the difference of the gain at the two ends, which was folded in the calibration coefficient.

Next, the calculated proton energy deposition in the bar, E^c, was plotted against $\sqrt{C^A(C^B - a)}$, where a is the offset of the bar. Figure 4-6(c) is the plot for Bar 8. The band in the figure is broad because of the uncertainty in the energy loss within the target. The bar ADC calibration coefficients was obtained by fitting the centroids of the band with a polynomial (Figure 4-6(d)). All 16 bars were calibrated in the same manner. From the calibrations, the measured energy deposition in the bars was calculated for each event.

4.5.2 The Proton Bar TDC calibration

In the bar TDC calibration first the TDC channel number needed to be converted to time in ns. This was done by measuring the TDC channel numbers corresponding to six different delay times. These six points were fitted with a straight line and the slope gives the channel–ns conversion coefficient (Figure 4-7(a)). From the fit it can be seen that the linearity of the TDC module was excellent. It was found that the coefficients are slightly different even among the 16 individual TDCs of the same FERA-TFC module (Figure 4-7(b)).

The bar TDC offsets come from the cable-length differences between the two ends. The TDC offsets were determined in a similar way as for the ADC offsets. The channel numbers were first converted into *ns*. For the events going into the center of the bar the A-side time of flight (TOF) was plotted against the B side, then the offset was obtained from fitting the centroids of the band with a straight line.

The TOF of two ends of a bar was combined by averaging. The averaged TOF does not depend on the proton entering point. The calculated TOF was plotted against the averaged TOF from the TDCs for the protons entering the center of the bar (Figure 4-7(c) for bar 8). The calibration was obtained by fitting the calculated TOF as a function of the TDC-offset corrected and averaged TOF: $(T^A + (T^B - offset))/2$ (Figure 4-7(d)). With this calibration the measured TOF was calculated for each event.

After the calibration of the P-bars' ADC and TDC, an effort was made to combine the proton energy in the bar obtained from ADC with that deduced from TOF. Through this combination the P-bars energy resolution could be improved, in principle, by a factor of $\sqrt{2}$. However, the results of the combination did not show an obvious improvement. It was found that the errors in both energies measured with ADC and TDC were dominated by the energy loss in the target. Although the combination can improve the intrinsic energy resolution of the P-bar, the error in the combined energy was still dominated by the energy loss in the target.

4.6 Particle Identification and Various Cuts

To separate proton Compton scattering events, the scattered particles, *i.e.* , the gamma and proton, needed to be identified first. Gamma rays entering the gamma-ray spectrometer were easily identified by requiring no signal in the 'turtle' scintillator. Gamma rays did not deposit energy in the 'turtle' except for about 5% of which converted into $e^{\pm}$ in the scintillator itself. This small fraction was vetoed and taken into account as part of the

detector efficiency (Section 5-1). At the end of the shower initiated by a gamma ray in the NaI, the positrons come to a stop and annihilate. The two 511 *keV* photons from one annihilation go back to back and one of them has a small chance to go back into the 'turtle'. The veto threshold of the 'turtle' was set to be 2 MeV allowing up to four such photons back to the 'turtle'. A particle which deposited more than 100 MeV in the NaI and less than 2 MeV in the 'turtle' was identified as a photon.

Particles going into the P-bars were identified by their TOF and energy deposition in the bars. At 44° laboratory angle most of the particles entering the P-bars are protons, with a small fraction being pions. The protons form a band in the plot of TOF vs. bar energy. The pions have smaller TOF and are below the proton band. The cut limits around the band form the proton PID cut, called the 'banana' cut (Figure 4-8(a)).

In addition to requiring the coincidence between scattered protons and photons identified with the above PID cuts, several others cuts were placed on the data. These cuts are described as follow:

- The vacuum window cut: In the target image obtained from event retracing it can be seen that events from the vacuum window wall are separated from events from the LH2 target (Figure 4-8(b)). The unwanted vacuum window events were cut out when the retracing point in the beam plane was greater than 8.92 or less than -10.24 cm.

- The tag TDC true peak cut: The trigger gate was set wide enough to let photons corresponding to six consecutive electron buckets into the tag TDC spectrum. The second peak to the left is the 'true' peak, which corresponds to the photon that experienced the nuclear reaction and made the trigger(Figure 4-8(c)). Other peaks are called 'accidental' peaks. There is a chance that there is more than one photon in the 'true' peak, but only one photon results in the trigger. The probability of this case is equal to that of a photon appearing in the 'accidental' peak. The true peak cut

selects only the events in the true peak, requiring the tag TDC channel being within a range of 305 to 643.

- The γ-ray spectrometer shielding cut: When a shower leaks out of the 19″ NaI, or a cosmic ray triggers the events, the 'back', 'annulus' or 'turtle' scintillators are fired. These events were cut out in the shielding cut, which is an OR of the 'back', 'annulus' or 'turtle' signals.

- The NaI bar cut: The π^0 events with the second photon fires one of the seven NaI bars around the target were cut out by this cut. This cut is an OR of the signals from these bars. About 6% of the total π^0 events were vetoed by the NaI bars, but about 25% are in the high-energy reagion of cutout.

- The 1-hit cut: When there are two or more photons in the 'true' tag TDC peak, it cannot be known which photon has undergone the nuclear reaction and triggered the event. Therefore, the energy of the incident photon is not determined. Fortunately, 92% of all the events have only one photon in the 'true' peak and the incident energy is unambiguously known. The events with ambiguity in the incident energy were cut out with the 1-hit requirement in the 'true' peak.

After the particle identification and the various cuts, the Compton events are needed to be separated from backgrounds in the remaining events. The following section discusses the separation procedures.

4.7 Separation of the Compton Events from the Background

The separation of the Compton events from the background, mainly π^0 production, is possible due to the fact that the Compton scattered gamma and proton have a different

energy and angular dependence from that of the background. The first step to obtain the yields is to identify the Compton events. Various ways were tried to improve the separation of the Compton events from the background. The measured physical quantities used are the incident gamma energy E^{in}, scattered photon energy E_γ, the recoil-proton angle θ_p, energy E_p and its time of flight T_p.

At the same proton-recoil angle and incident gamma energy the Compton events should have the same scattered photon energy. However, in the histograms of the scattered photon energy the Compton peak could not be distinguished (Figure 4-9(a)). One reason is that the π^0 background is enormous and the peak from the Compton events is rather weak. Another reason is that, at the same proton-recoil angle, the π^0 scatters at a smaller angle than the gamma. For example, at the same 44° recoil proton angle, the gamma in Compton event scatters at 76° while the π^0 scatters at 64°. The decay gamma from this π^0 can have a maximum energy only a few MeV lower than the Compton gamma (Figure 3-2(a)). Therefore the weak Compton peak is almost completely shadowed by the continuous π^0 peak and cannot be identified with the scattered photon energy alone. In the histograms of other quantities, such as the the proton TOF (Figure 4-9(b)), the Compton peak is also not clear.

From E^{in} and θ_p the scattered gamma energy and recoil proton TOF can be calculated for each event, denoted as E_γ^c and T_p^c, respectively. A way to make use of the kinematic redundancy is to form the differences of the measured and calculated scattered gamma-ray energies $\Delta E_\gamma = (E_\gamma - E_\gamma^c)$, and that of the recoil proton time of flights, $\Delta T_p = (T_p - T_p^c)$. The Compton events of different incident gamma energy and scattering angle are brought together in one peak. As a result, the weak Compton peak has greater statistics and can then be identified.

The separation of the Compton peak from the background is enhanced in the 2-dimensional plot of $(E_\gamma - E_\gamma^c)$ verses $(T_p - T_p^c)$. Figure 4-9(c) shows the case for proton recoil angles from 43° to 45°, in which the Compton peak is near zero in both axis. The apparent spread

of the Compton peak is almost entirely due to variations in the recoil proton's energy loss in the proton target. The π^0 background is above the Compton peak since protons from π^0 events have smaller energy and larger TOF. In the lower left part there are some background events from the nuclear reactions with the target wall. They have lower gamma energy and are well separated from the Compton events. Cutting out events of ΔE_γ below -40 MeV can eliminate these background, and also cuts out most of the π^0 background.

In the projection to the ΔT_p axis of the 2-dimensional plot with the ΔE_γ cut, the Compton peak can be clearly identified (Figure 4-9(d)). However, from Figure 4-9(c) it can be seen that better separation can be obtained if the Compton peak is projected on a rotated axis $\Delta T_p'$ (Figure 4-10). $\Delta T_p'$ is a mixture of ΔE_γ and ΔT_p. This is especially helpful at smaller recoil angles since the separation is not as good there. The separation before and after the rotation at 39° to 41° was compared in Figure 4-10(b). The separation after rotation is clearly better. The rotation angle used is 14°. The final cut on the Compton peak is on this rotated quantity $\Delta T_p'$.

The incident gamma energy E^{in} was divided into 10 MeV bins from 220 to 340 MeV. Below 220 MeV most recoil protons do not have enough energy to reach the P-bars, because of energy loss. In order to see the angular dependence of the separation, the rotated $\Delta T_p'$ was plotted as a function of the proton recoil angle θ_p for each energy bin. In Figure 4-10(c), for E_γ of 290 — 300 MeV the Compton events form the lower band and the partially cut π^0 background form the upper band. It can be seen that the separation at large angles is better than at small angles. This can be seen from the relation between TOF and E_p: $T_p \sim \frac{1}{\sqrt{E_p}}$ for low energy, so $\Delta T_p \sim \frac{\Delta E_p}{E_p^{\frac{3}{2}}}$. Since ΔE_p is almost constant in the angular range (Figure 3-2(b)), the difference in TOF becomes larger when E_p gets smaller at larger recoil angle. Another reason is that at low energies the stopping power of the proton increases strongly with decreasing energy. The lower-energy proton loses more energy after traversing the same amount of medium. As the result the energy difference between the Compton and π^0 proton at the P-bar increases as the recoil angle increases.

To set the final cut for the Compton peak the rotated $\Delta T_p'$ was plotted for twelve 2° angle bins from 34° to 56°. For each angular bin the cuts of Compton peak were set after comparing the separation of the parallel (Figure 4-11) and perpendicular (Figure 4-12) polarization for E^{in} from 290 to 300 MeV. The same procedure was done for each of the 12 energy bins. For each incident energy the yields of several angular bins were summed to obtain reasonable statistics. After comparing the separation of all the energy bins it was found that for the energy bins from 245 to 335 MeV the separation within 39° to 49° was clear enough for a direct cut and could be summed together. The angular range of 41° to 45° was used for 225 to 235 MeV bins. The yields for the parallel (P1) and perpendicular (P2) polarization from energy 225 to 330 MeV summed over 39° to 49° are listed in Table 4-1.

4.8 Empty Target Substraction

In order to see the contribution of events from the target walls a set of data was collected with an empty target. The data set was analysed with the same procedure and the same cuts as the full target data set. The number of background target wall events which passed through the Compton peak cuts is small. The empty target yields are shown in Table 4-1. The γ-ray flux for Pol 1 and Pol 2 in the full target runs is 6.06 and 5.87 times that of the empty-target runs, respectively.

The main background process is assumed to be the quasi-free pion photoproduction from the target mylar wall. The backgrounds in the parallel polarization are smaller than in the perpendicular polarization, which is consistant with the assumption. Since the counts of the empty-target yields are small and have large fluctuations, the yields are averaged over the energy bins for each polarization. After scaling up to the same full target run flux, the averaged yields are: $Y^{p1}_{empty} = 3$ counts per energy bin for parallel polarization and $Y^{p2}_{empty} = 9$ counts per energy bin. This empty-target background was substracted in the calculation of the differential cross sections.

Table 4-1: The Yields of Two Polarizations for 11 Energy Bins

Energy Bin ($\pm 5\ MeV$)	Full Target (Parallel)	Full Target (Perpendicular)	Empty Target (Parallel)	Empty Target (Perpendicular)
225	88	101	1	1
235	171	161	0	4
245	222	223	1	1
255	323	291	0	1
265	418	344	1	1
275	614	396	0	1
285	743	540	1	1
295	976	593	1	4
305	1135	673	1	4
315	808	390	0	1
325	351	136	0	0

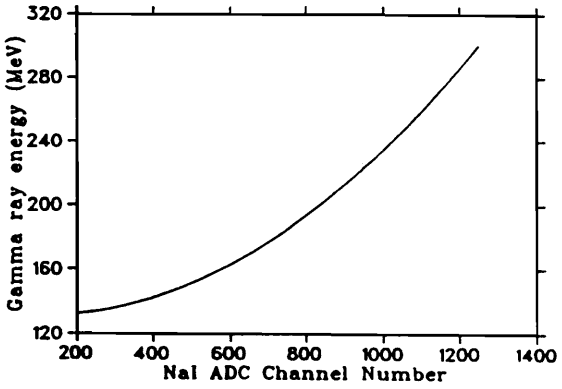

Figure 4-1: The calibration of the gamma ray spectrometer with the LEGS gamma beam: gamma ray energy as a function of the ADC channel number.

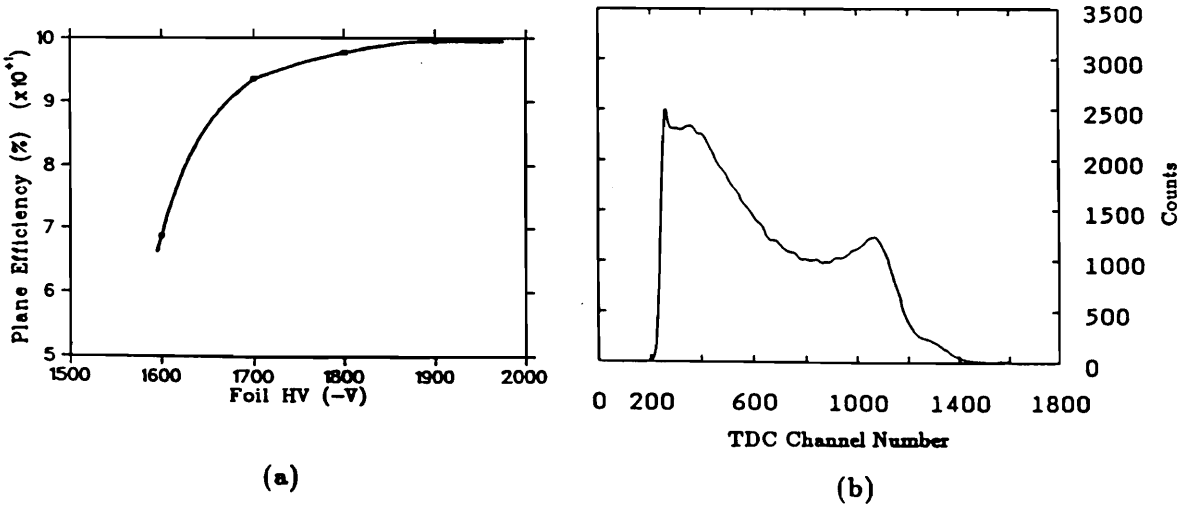

Figure 4-2: (a): The drift chamber plane efficiency as a function of the foil negative voltage for plane 1 of the first chamber. The field wire voltage was ' 13 times of the foil voltage. (b): The drift chamber TDC spectrum for a central wire. X axes is in channel number which is proportional to the relative drift time. Y axes is the number of counts per channel.

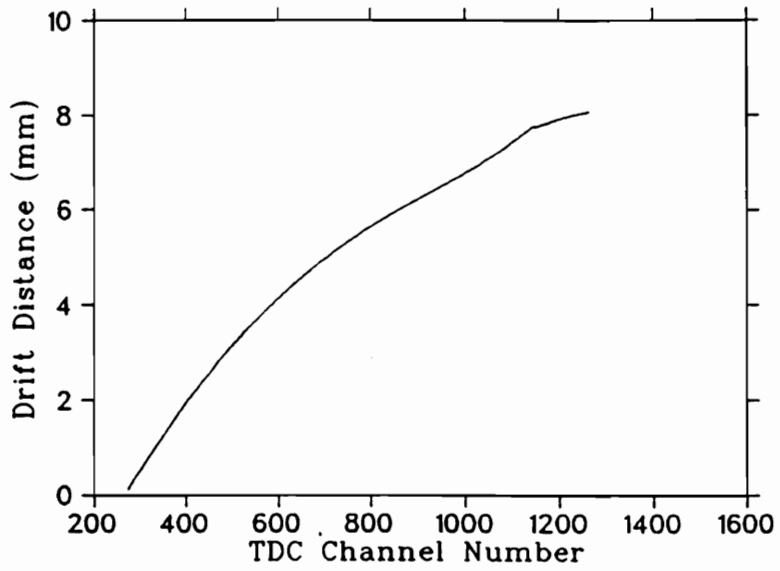

(a)

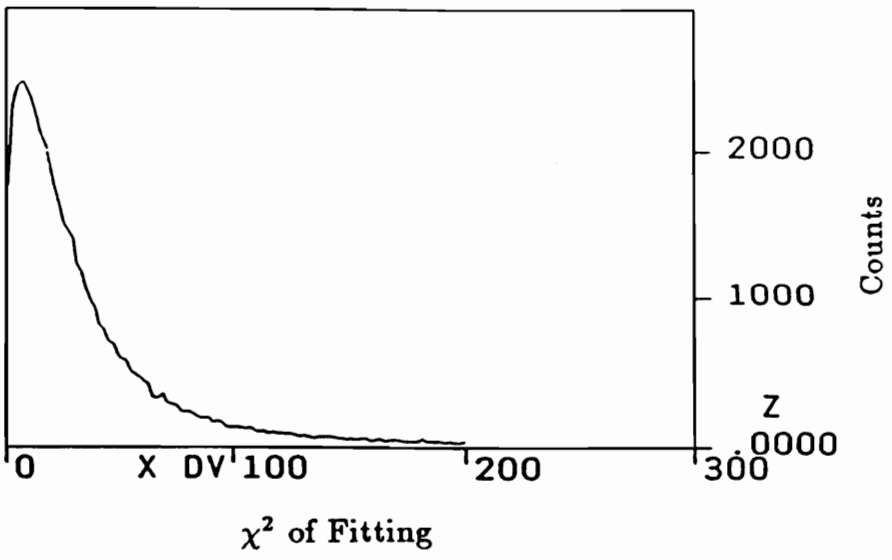

(b)

Figure 4-3: (a): The calibration of the drift chamber: drift distance as a function of the TDC channel number. (b): The histogram of the χ^2 (in unit of mm^2) of the fitting in event retracing.

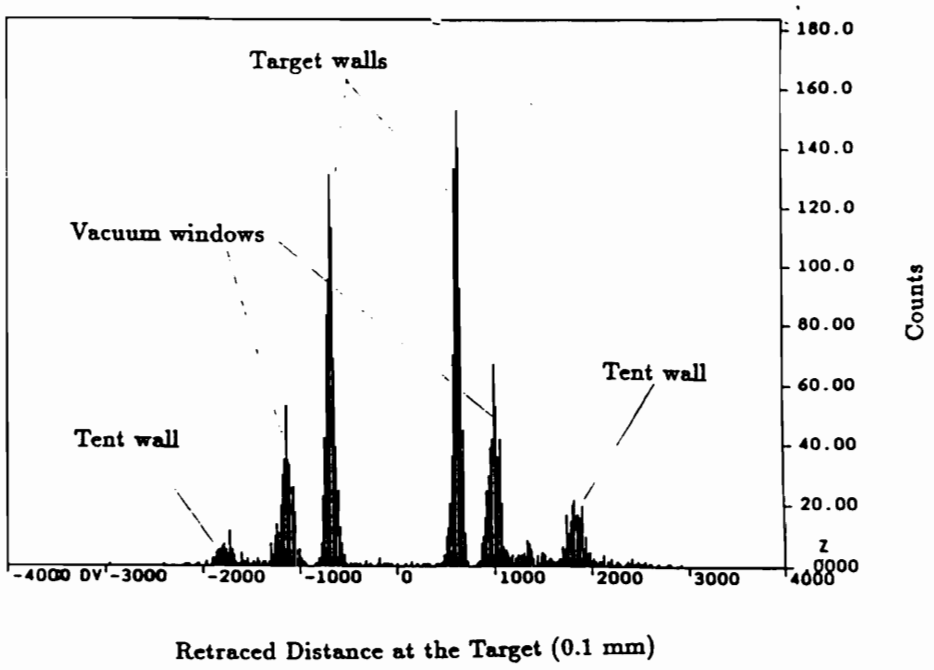

Figure 4-4: The target image from retracing for the empty target. Drift chambers were at 80°. The target walls, vacuum windows and protection tent walls are clear.

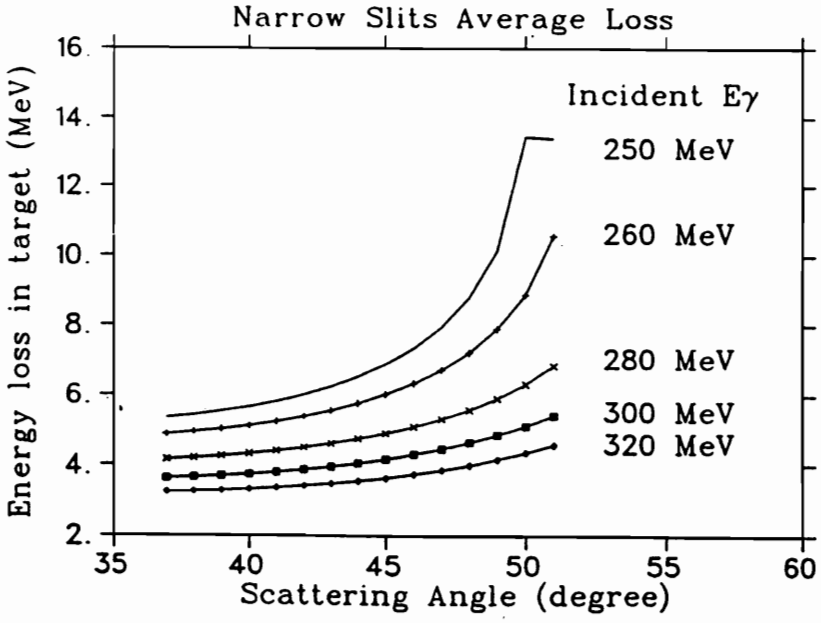

Figure 4-5: The calculated average energy loss in the target for narrow slits as a function of recoil proton angles.

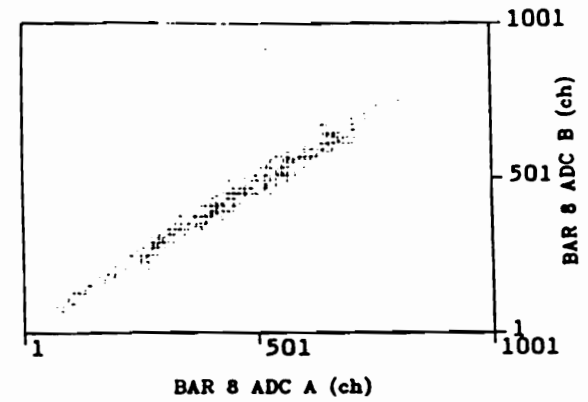

(a)

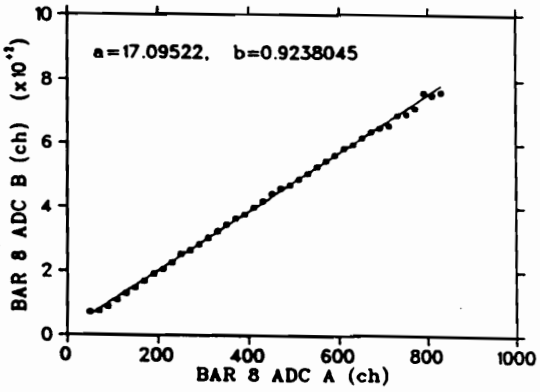

(b)

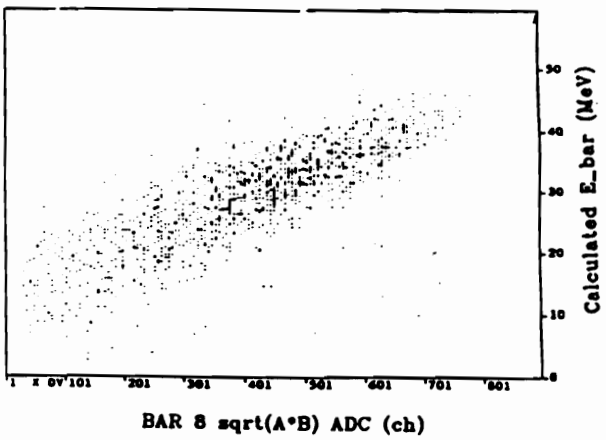

(c)

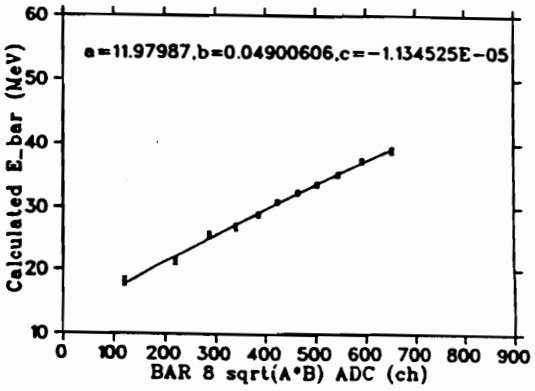

(d)

Figure 4-6: (a): 2-D histogram of bar ADC side A channel number verses that of side B for bar 8. (b): The centroids of the band in (a) and the fitting. The offset of this line is the offset of the bar ADC. (c): 2-D histogram of the calculated proton energy in the bar verses the combined bar ADC channel number for bar 8. (d): The centroids of the figure (c) and the polynomial fitting which gives the bar ADC calibration.

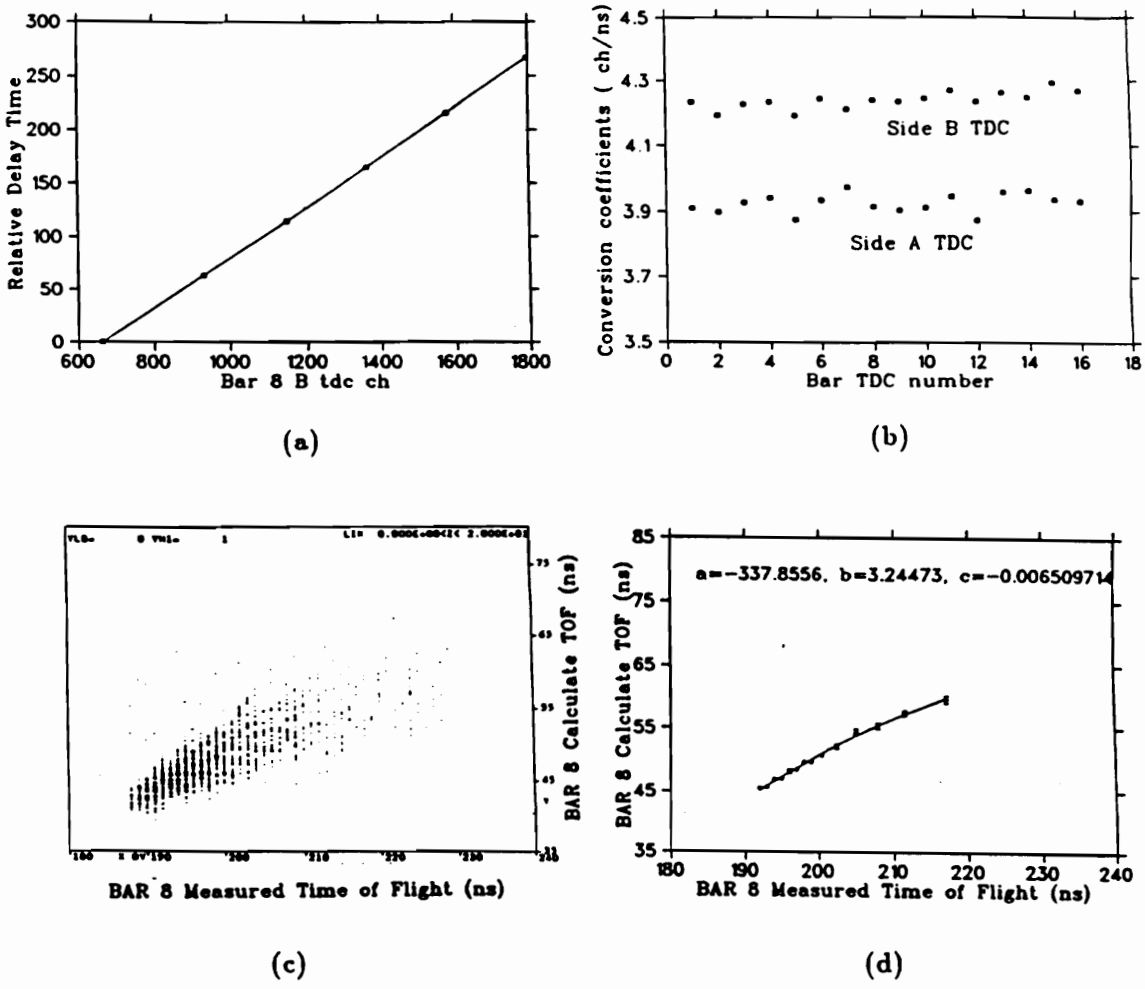

Figure 4-7: (a): The bar TDC channel number verses the delay time. The slope of the fit gives the channel–ns conversion coefficient. (b): The channel–ns conversion coefficients for the 16 individual TDCs in the same FERA-TDC modules for side A and B. (c): 2-D histogram of calculated TOF to the bar verses the combined bar TDC channel number, for bar 8. (d): The centroids of the figure (c) and the polynomial fitting which gives the bar TDC calibration.

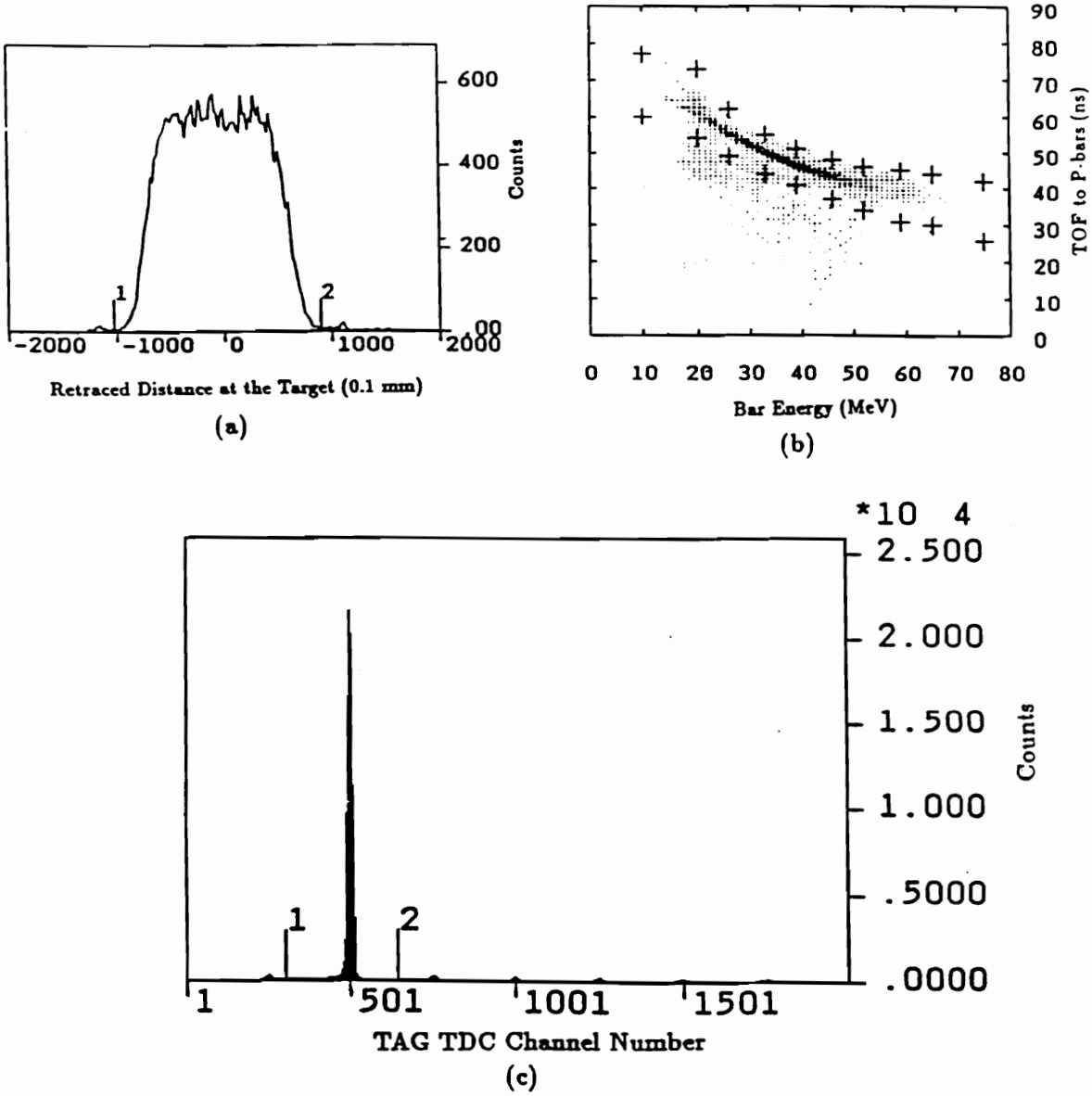

Figure 4-8: (a): The full target image from drift chamber retracing. The two small peaks outside were from the vacuum windows and were cut out. (b): The 2-D histogram of proton TOF verses the energy deposition in the bar. The points around the proton band form the proton PID cut. (c): The histogram of the tag TDC channel number. The peak between cut 1 and 2 is the 'true' peak. When requiring one tag hit the accidental peaks are small.

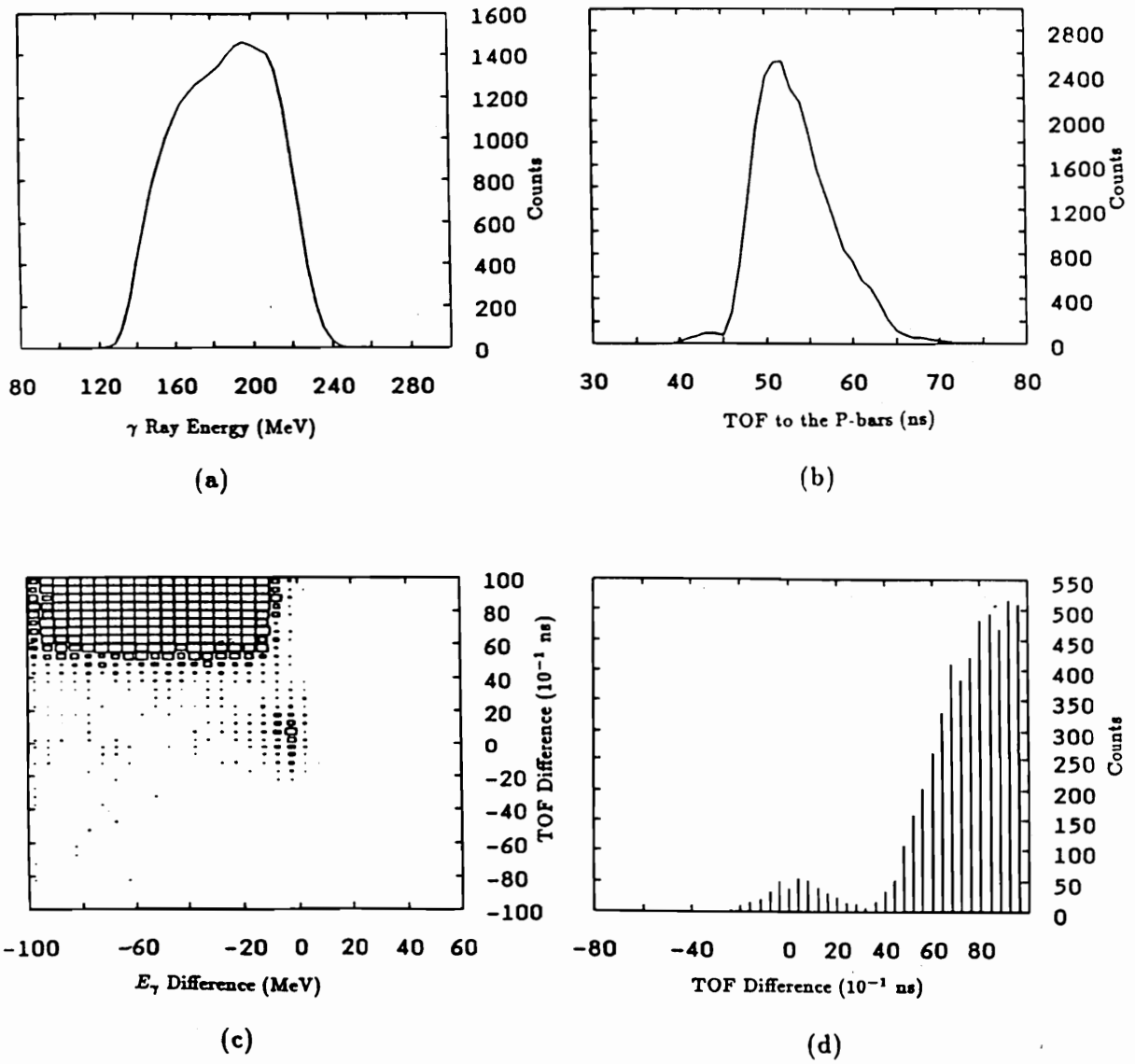

Figure 4-9: (a): The histogram of scattered γ ray energy at $\theta_p = 40 \pm 1^\bullet$ and $E_{in} = 295 \pm 5 MeV$. Compton events should be at the high energy edge. (b): The histogram of recoil proton TOF at $\theta_p = 40 \pm 1^\bullet$ and $E_{in} = 295 \pm 5\ MeV$. In both (a) and (b) the Compton peak can hardly be identified. (c): The 2-dimensional histogram of ΔT_p verses ΔE_γ in which the Compton peak is clear. The angular bin and E^{in} is the same as in (a) and (b). (d): The projection of (c) for ΔE_γ from -40 to 30 MeV on the ΔT_p axes. The Compton peak is the small one on the left.

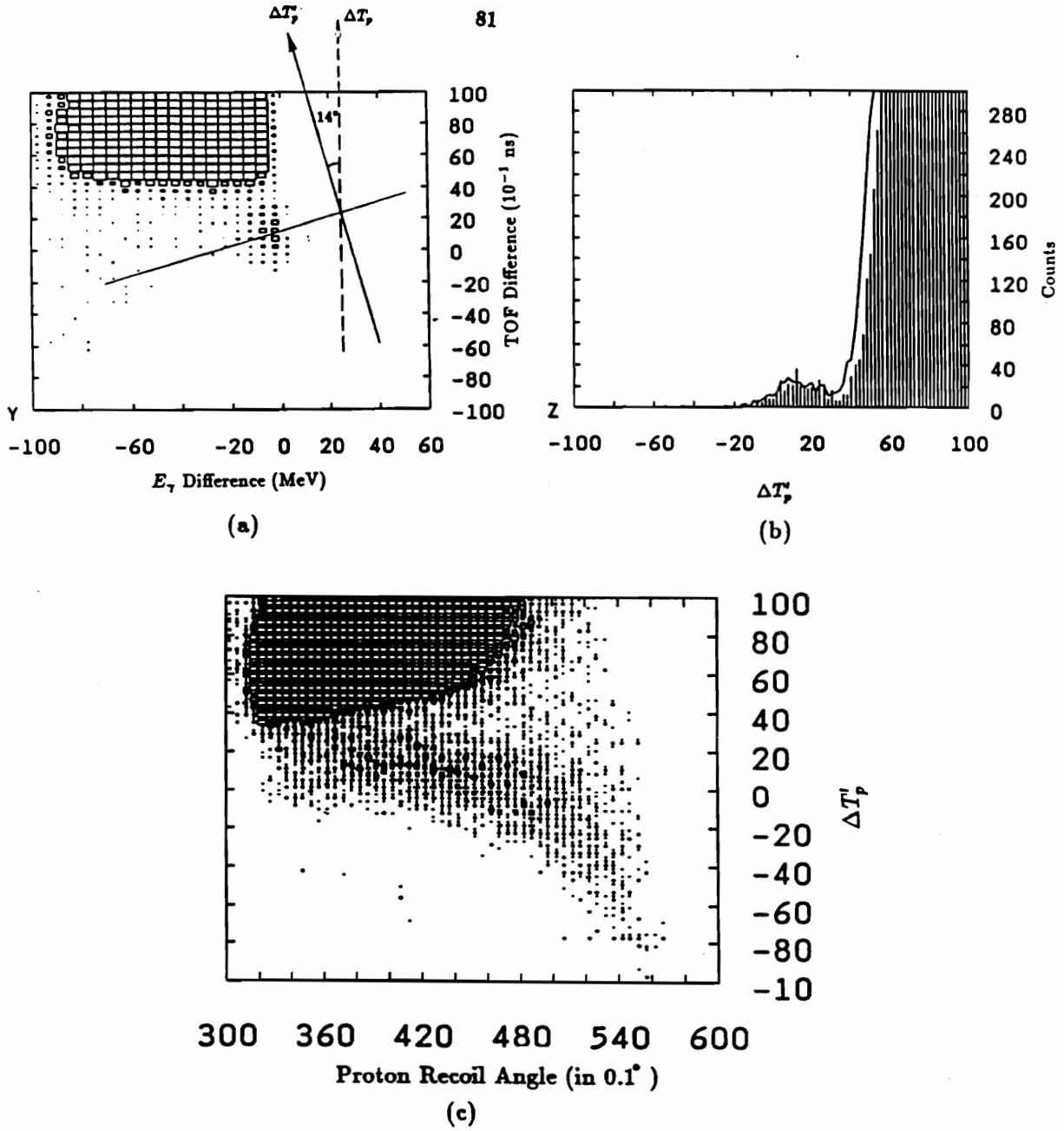

Figure 4-10: (a): The 2-D histogram ΔT_p vs. ΔE_γ at θ_p from 39° to 41° with the rotated projection axes. (b): The projection of (a), for $\Delta E_\gamma \geq -40$, on the rotated axes (bar plot) is compared with that before the rotation (solid line). (c): 2-D histogram of projection on $\Delta T_p'$ verses the proton recoil angles. The lower band is Compton events. The separation gets better at larger angles.

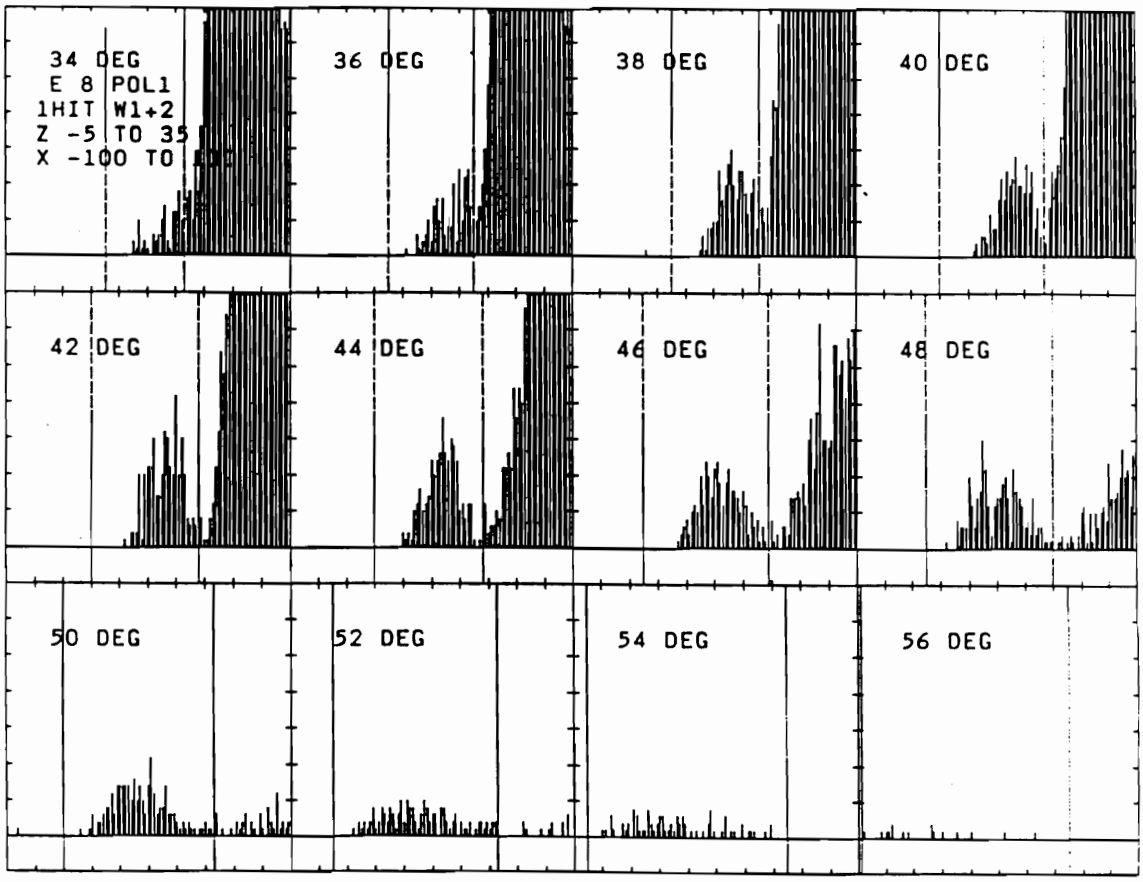

Figure 4-11: The projections on the rotated axis for twelve 2° recoil angle bins for the incident gamma rays with parallel polarization are shown in each panel. Incident gamma energy is 295 ± 5 MeV. The cuts for each panel are shown in dotted lines. The yields from 39° to 49° were summed together to obtain a reasonable statistics.

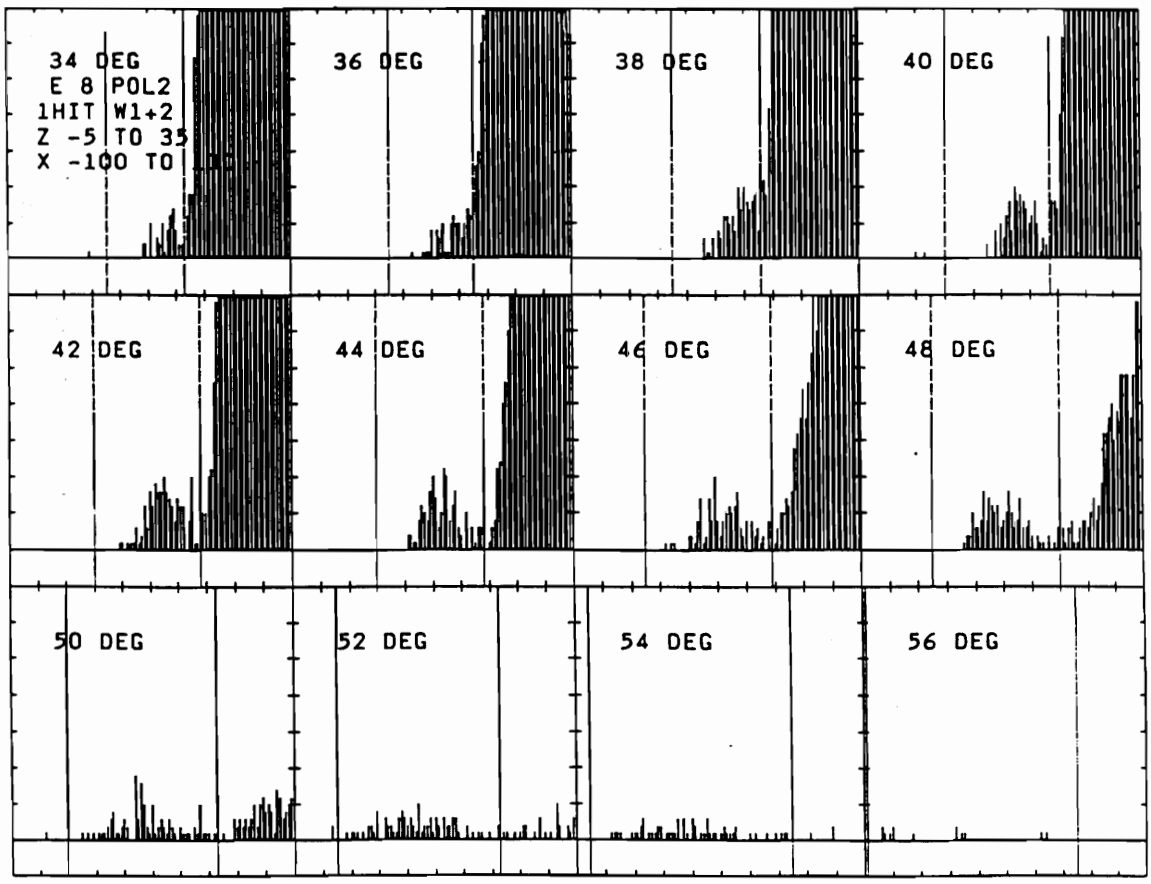

Figure 4-12: The histograms of projection on the rotated axis for 12 angular bins for the incident gamma of perpendicular polarization. Note that the Compton peaks are larger than that of parallel polarization, and the π^0 peaks are just the opposite. This is due to the opposite asymmetry for the Compton scattering and the π^0 production.

Chapter 5

The Asymmetries and Cross Sections

5.1 Detector Efficiencies and Acceptances

The overall efficiency of the P-bars was obtained using the recoil protons in the nuclear event with the drift chambers as a reference. The events used for measuring P-bar efficiency were restricted to the center part of the target, so that almost all particles passing through the drift chambers are protons. The ratio of the number of protons reaching the P-bars over the number of protons firing all drift chamber planes gives the overall efficiency of P-bars η_{bar}:

$$\eta_{bar} = \frac{N_{bar} * N_{dc} * N_{tc}}{N_{dc} * N_{tc}}, \tag{5.1}$$

where N_{bar} denotes the events reaching the P-bar, N_{dc} the events having a good track in the wire chamber, N_{tc} the events coming from center of the target, and $*$ denotes the logical AND between the events. This overall efficiency takes into account the case when a proton has too little energy and stops before reaching the P-bars. It also takes into account the

events passing through the gaps between bars. The P-bar overall efficiency was found to be 96% .

The overall efficiency for the drift chambers was obtained similarly with the P-bars as a reference. The events coming hitting central part of the P-bars and within the proton PID cut of P-bars were selected. Similarly, the drift chamber overall efficiency is written as:

$$\eta_{wc} = \frac{N_{dc} * N_{bar}^{P} * N_{bc}}{N_{bar}^{P} * N_{bc}}, \tag{5.2}$$

where N_{bar}^{P} denotes the events in the proton band of the plot T_p vs. E_p (Figure 4-8(b)) and N_{bc} denotes the events hitting the central part of the P-bars. The overall drift chamber efficiency was found to be 98.5% .

A Monte Carlo simulation of this experiment was conducted in order to obtain the detector acceptance and the efficiency of the gamma ray spectrometer. The geometrical acceptance of the gamma ray spectrometer only partially overlaps with the corresponding P-bars acceptance. Therefore, the combined acceptance has to be obtained with a Monte Carlo simulation. The GEANT package from CERN was used for the simulation.

In the simulation the whole gamma ray spectrometer structure with all the plastic scintillators, the 'turtle', 'annulus', 'back', lead shielding, and the P-bars geometry were put into the code to obtain the acceptance. The gamma beam profile and the target geometry were also put into the code. The kinematic thresholds in the simulation were the same as that used in the data analysis. The acceptance Ω and the gamma spectrometer efficiency η_γ were obtained from the simulation. Since the target end cap is curved, the average target length, L_{tgt}, was also obtained from the simulation. The product of the acceptance, gamma spectrometer efficiency and the average target length as a function of the incident gamma ray energies is shown in Figure 5-1. These points were fitted with a polynomial: $\Omega\eta_\gamma L_{tgt} = a + bE^{in} + cE^{in^2}$, where $a = -1.9578$, $b = 2.9912 \times 10^{-2}$, and $c = -5.32064 \times 10^{-5}$ for the gamma spectrometer acceptance corresponding to θ_p =39° — 49°.

5.2 The γ Ray Beam Flux

At LEGS the γ-ray flux is monitored on line for each run. The flux is measured by the flux monitor, called CG3. The CG3 monitor is placed in the γ-ray beam just in front of the beam profile monitor. The absolute flux is known to a high accuracy, of $\pm 1\%$.

The CG3 monitor consists of two square plastic scintillators with a copper convertor in between, with a thickness about 6% of a radiation length. The upstream scintillator, called PCV, with dimensions $10.5'' \times 12''$ and $\frac{1}{2}''$ thick, is used to veto charged particles entering the monitor. A fraction of γ-rays are converted into $e^{\pm}$ pairs in the convertor and the pairs enter the scintillator behind, called PCC, with dimensions of $6'' \times 6''$ and $0.25''$ thick. The coincidence of the PCC and the tag signals, with anti-coincidence with the PCV signal, is the monitor scaler event trigger. This event is only counted by a scaler.

In the measurement of the CG3 monitor efficiency the total number of photons, N_{NaI}, in the gamma beam is measured with a NaI detector, $10''$ in diameter and $14''$ long, in the beam. The flux of the beam is reduced to about 20 kHz during this measurement. The efficiency of the NaI detector is 100% for photons in the tagging range. The number of events in CG3, N_{cg3}, is measured after moving the NaI detector out of the beam. After accidental subtraction the number of CG3 and NaI events are normalized to the same amount of TAG triggers, denoted as N'_{NaI} and N'_{cg3}, respectively. The ratio of N'_{cg3} and N'_{NaI} gives the CG3 monitor efficiency,

$$\eta_{cg3} = \frac{N'_{cg3} * TAG}{N'_{NaI} * TAG}, \tag{5.3}$$

where TAG denotes the events with photon tagger fired. The efficiency of the monitor was measured several times during the experiment at different energies. The efficiency differs slightly at different energies. The average efficiency is $\eta_{cg3} = 6.4\%$. The total number of photons in the beam F_{tot} is given by: $F_{tot} = N_{slr}/\eta_{cg3}$, where N_{slr} is the number of scaler events.

During a normal data run, the rate of the monitor scaler events is high, of the order of

100 kHz. To reduce the computer dead time only a small fraction of these events, called monitor events, are analysed on line. A monitor event is triggered every one out of 4096 monitor scaler events. The 64 tag TDC's, the ADCs for PCC and PCV are recorded for each monitor event. The spectra of the PCC and PCV ADC's are shown in Figure 5-2. The PCV spectrum has two peaks. The peak with high channel number corresponds to the case when both the electron and positron in the beam enter the PCV. The other peak corresponds to the case when either the electron or positron enters the PCV but the other is missed. In the PCC spectrum, the peak corresponds to the events when both $e^{\pm}$ enter PCC, which has greater probability since the convertor is right in front of the PCC. The peaks in PCC and PCV spectra change slowly when the γ-ray rate decreases in a electron beam fill. These peaks were adjusted to fixed positions several times during each run in order to stablize the veto and acceptance thresholds.

The monitor events show a sample of the γ-ray beam. Figure 5-3 shows the gamma ray spectrum as a function of tag channels, in which low tag channels correspond to high γ-ray energies. There are three overlaping Compton edges at the left end of the spectrum, corresponding to the three laser lines (Section 2-8). The relative flux at each γ-ray energy, $F'(E^{in})$, is obtained from the spectrum. The absolute flux at each energy, $F(E^{in})$, is obtained by:

$$F(E^{in}) = F_{tot}\frac{F'(E^{in})}{\sum_{E^{in}} F'(E^{in})} = \frac{N_{slr}}{\eta_{cg3}}\frac{F'(E^{in})}{\sum_{E^{in}} F'(E^{in})} \; . \tag{5.4}$$

The position of the Compton edge changes from run to run by a maximum of 1 tag channel, about 2 MeV. In order to reduce the error resulting from the edge shifting, the Compton edge positions were obtained for each run and then shifted to the same position in the calculation of the flux . For the normal slits runs the γ-ray total flux in 10 MeV bins for the two polarization is given in Table 5-1. This flux includes single or multiple photons created in a bucket. The ratio of the number of events with only one photon in the true peak and that with one or more photons in the true peak was obtained for each of the 10 MeV bins (Table 5-1). The flux for the case with only one photon in the true peak was obtained as a

product of the ratio and the total photon flux.

5.3 The Corrections of Finite ϕ Acceptance and γ Ray Polarization

The polarization of the incident γ-ray beam at the target is not exactly the same as from the backscattering given in Chapter 2. It needs to be corrected in accordance with the experimental conditions. The corrected polarizations of the two states are given by:

$$P_1^{cor} = \Lambda\, P_b\, (P_{l1}\, P_1^{calc} - \tfrac{1}{2}(1 - P_{l1})(P_2^{calc} - P_1^{calc}))\ , \tag{5.5}$$

$$P_2^{cor} = \Lambda\, P_b\, (P_{l2}\, P_2^{calc} - \tfrac{1}{2}(1 - P_{l2})(P_2^{calc} - P_1^{calc}))\ , \tag{5.6}$$

where P_1^{cor} and P_2^{cor} are the corrected polarizations. The corrections are described as below.

Λ is the correction due to the finite azimuthal acceptance of the detectors. This is not a beam polarization correction, but has the equivalent effect upon a polarization observable. The cross section measured in the experiment is an integration over the finite azimuthal acceptance. In the calculation of the cross sections parallel and perpendicular to the reaction plane, the finite azimuthal correction Λ is needed, which is given by:

$$\Lambda = \frac{\sin(2\phi_0)}{2\phi_0}\ . \tag{5.7}$$

And ϕ_0 is given by:

$$\phi_0 = tan^{-1}\frac{\tan\frac{\psi}{2}}{\sin\theta_{lab}^{\gamma}}\ , \tag{5.8}$$

where ψ is the detector azimuthal acceptance and θ_{lab}^{γ} =76° is the scattered γ-ray lab angle. In the present experiment the azimuthal acceptance is determined by the collimator of the γ-ray spectrometer, which has a circular opening of diameter 20.76 cm. Since an extended target was used, the maximum azimuthal acceptance angle varies for events from different parts of the target. An average azimuthal acceptance angle ϕ_{acc} =24° was used, which gives Λ = 0.9693.

Table 5-1: The Gamma Ray Flux of Two Polarizations

Energy Bin ($\pm 5\ MeV$)	Single Hit Ratio	Total Flux (Parallel)	Total Flux (Perpendicular)
225	0.9675297	3.3305893E+10	3.2527651E+10
235	0.9603162	3.5055022E+10	3.4524656E+10
245	0.9610429	3.7052944E+10	3.6270424E+10
255	0.9537558	3.9757107E+10	3.8970085E+10
265	0.9469699	4.2451522E+10	4.1802027E+10
275	0.9394787	4.5449384E+10	4.4630725E+10
285	0.9285277	4.8161493E+10	4.7751315E+10
295	0.9228374	5.0745463E+10	4.9975067E+10
305	0.9140466	5.0492551E+10	4.9625154E+10
315	0.9024189	3.4624791E+10	3.2060004E+10
325	0.8877873	1.4263355E+10	1.1409561E+10
331	0.8724529	5.0143852E+09	3.9058954E+09

P_b is the correction from the Bremsstrahlung background in the beam. The Bremsstrahlung component is un-polarized and dilutes the beam polarization. Since the residual molecules in the electron ring are very few, the portion of this component F_b is very small. The corrections were measured from the Bremsstrahlung data as: $P_b = 1 - F_b = 0.998$, averaged for both polarizations.

P_{l1} and P_{l2} are the laser polarizations at the straight section for Pol 1 and Pol 2. Since the optical lenses and quartz window decrease the laser polarization, the laser polarization is not linear at the interaction section. The degree of polarizations were measured several times during the experiment and they were very stable: $P_{l1} = P_{l2} = 0.96 \pm 0.02$.

P_1^{calc} and P_2^{calc} are the calculated beam polarizations assuming the laser polarization is 1 at the straight section. P^{calc} is 1 at the Compton edge and decreases at lower γ-ray energies. The results of the calculation were fitted with a polynomial: $P^{calc} = a + bE^{in} + cE^{in^2} + dE^{in^3}$, where $a = -1.128615$, $b = 1.223324 \times 10^{-2}$, $c = -1.275596 \times 10^{-5}$, and $d = -1.47799 \times 10^{-8}$ for P_1^{calc}; and $a = -2.0092$, $b = 2.21336 \times 10^{-2}$, $c = -4.94817 \times 10^{-5}$, and $d = 3.01794 \times 10^{-8}$ for P_2^{calc}.

5.4 The Calculation of the Cross Sections and Asymmetries

The differential cross section, by definition, is written as:

$$\frac{d\sigma}{d\Omega}(\theta) = \frac{dN}{F\ N_t\ d\Omega} \tag{5.9}$$

where dN is the number of particles scattered into $d\Omega$ per unit time, F is the number of incident particles per unit time per unit area, and N_t is the number of scattering centers. This equation can be re-written in a way convenient for experimental calculation. Assuming the data collecting time is t, the total yield is ΔN, the beam spot has an area of a, the target length is L_{tgt} and the number of scattering centers per unit volume is n_{tgt}, then

Table 5-2: The Polarized Cross Sections At 90° CM.

Energy Bin (± 5 MeV)	Jacobian	Cross section in nb (Parallel)	Standard Deviation	Cross section in nb (Perpendicular)	Standard Deviation
225.	0.9676	39.423	6.754	42.857	6.842
235.	0.9651	65.039	8.126	60.106	7.804
245.	0.9617	67.990	5.233	67.740	5.212
255.	0.9583	92.469	5.763	81.298	5.478
265.	0.9569	112.360	6.064	89.009	5.520
275.	0.9525	155.758	6.839	94.125	5.611
285.	0.9495	178.055	7.189	123.672	6.217
295.	0.9447	224.419	7.897	129.077	6.396
305.	0.9415	266.259	8.743	150.118	7.065
315.	0.9382	283.747	10.745	134.421	8.207
325.	0.9330	307.899	17.177	127.449	12.805

$N_t = a\, L_{tgt}\, n_{tgt}$ and the cross section in the lab system can be written as:

$$\frac{d\sigma}{d\Omega}(\theta) = \frac{t\, dN}{t\, F\, a\, L_{tgt}\, n_{tgt}\, \Delta\Omega} = \frac{A}{N_0}\frac{\Delta N}{F_{tot}\, \rho\, L_{tgt}\, \Delta\Omega}, \tag{5.10}$$

since $F_{tot} = t\, F\, a$, $n = N_0 \frac{\rho}{A}$, where $N_0 = 6.0222 \times 1023$ is the Avogadro's number, A is the mole weight and ρ is the target density. The CM cross section, in unit of *barn*, is expressed as:

$$\frac{d\sigma}{d\Omega}(\theta) = 1.66113\, A\, \frac{\Delta N}{F_{tot}\, \rho\, L_{tgt}\, \Delta\Omega}\frac{d\Omega_{lab}}{d\Omega_{cm}}\ (barn) \tag{5.11}$$

when for a proton target, $A = 1.00837$, and $\rho = 0.0708 g/cm^3$. The Jacobian of the transformation from lab to CM frame,

$$\frac{d\Omega_{lab}}{d\Omega_{cm}},$$

is given in Table 5-2 for different energies. If the yield for the energy bin E^{in} is $Y(E^{in})$, then

$$\Delta N(E^{in}) = \frac{Y(E^{in})}{\eta_{bar}\, \eta_{dc}\, \eta_\gamma}. \tag{5.12}$$

The acceptance folded with the target length and gamma spectrometer efficiency is given in Section 5-1. From the above equations the differential cross sections for Pol 1 and Pol 2 were calculated, denoted as $\frac{d\sigma_1}{d\Omega}$ and $\frac{d\sigma_2}{d\Omega}$, respectively. For the incident energy bins at 225 and 235 MeV, since the recoil protons at large angle were lost in the flight, the recoil angular bin of 41° to 45° was used, instead of 39° to 49° for the other energy bins.

The polarized differential cross sections of interest are $\frac{d\sigma_\parallel}{d\Omega}$ and $\frac{d\sigma_\perp}{d\Omega}$, which are the components parallel and perpendicular to the reaction plane, respectively. With the azimuthal angle and polarization corrections given in the previous section, they are deduced from $\frac{d\sigma_1}{d\Omega}$ and $\frac{d\sigma_2}{d\Omega}$ by the expressions:

$$\frac{d\sigma_\parallel}{d\Omega} = \frac{1}{P_2^{cor} + P_1^{cor}}((P_1^{cor} + 1)\frac{d\sigma_1}{d\Omega} + (P_2^{cor} - 1)\frac{d\sigma_2}{d\Omega})\ , \tag{5.13}$$

$$\frac{d\sigma_\perp}{d\Omega} = \frac{1}{P_2^{cor} + P_1^{cor}}((P_1^{cor} - 1)\frac{d\sigma_1}{d\Omega} + (P_2^{cor} + 1)\frac{d\sigma_2}{d\Omega})\ . \tag{5.14}$$

The results are listed in Table 5-2. At the highest gamma energy, 331 MeV, the gamma flux is small and the absolute flux has large error. So differential cross sections were calculated up to 325 MeV. The polarized cross sections are shown in Figure 5-4.

Table 5-3: Unpolarized Cross Section and Asymmetry

γ Energy ($\pm 5\ MeV$)	Cross section (Un-polarized)	Standard Deviation	Asymmetry	Standard Deviation
225.0	41.140	4.807	-0.068	0.113
235.0	62.575	5.633	0.056	0.077
245.0	67.865	3.693	0.002	0.062
255.0	86.891	3.975	0.064	0.050
265.0	100.692	4.100	0.116	0.044
275.0	124.932	4.423	0.247	0.036
285.0	150.832	4.752	0.180	0.032
295.0	176.669	5.081	0.270	0.028
305.0	208.095	5.620	0.279	0.026
315.0	209.028	6.760	0.357	0.032
325.0	217.777	10.713	0.414	0.053

The unpolarized differential cross section, $\frac{d\sigma^{unp}}{d\Omega}$, can be calculated with $\frac{d\sigma_1}{d\Omega}$ and $\frac{d\sigma_2}{d\Omega}$ using the equation:

$$\frac{d\sigma^{unp}}{d\Omega} = \frac{1}{P_2^{cor} + P_1^{cor}}\left(P_1^{cor}\frac{d\sigma_1}{d\Omega} + P_2^{cor}\frac{d\sigma_2}{d\Omega}\right) . \tag{5.15}$$

The unpolarized differential cross sections are listed in Table 5-3 and shown in Figure 5-4.

The cross section polarization asymmetries are obtained in terms of $\frac{d\sigma_1}{d\Omega}$ and $\frac{d\sigma_2}{d\Omega}$ by the following equation:

$$\Sigma = \frac{\frac{d\sigma_1}{d\Omega} - \frac{d\sigma_2}{d\Omega}}{P_1^{cor}\frac{d\sigma_2}{d\Omega} + P_2^{cor}\frac{d\sigma_1}{d\Omega}}. \tag{5.16}$$

The asymmetries at incident gamma energy from 225 to 325 MeV are listed in Table 5-3. These are the first results of proton Compton scattering asymmetry as a function of gamma energy. The only other datum available was measured a long time ago and with large error [11]. The present results have considerably smaller errors in the Δ region. Since the asymmetry depends only on the ratio of cross sections of the two polarizations, most of the systematic error in this measurement is canceled out. The asymmetries are shown in Figure 5-5.

In the normal data collection runs the polarization was randomly flipped between $\Phi = 0°$ and $\Phi = 90°$. A portion of the data was also collected with the polarization flipping between $\Phi = 43°$ and $\Phi = 133°$. This set of data is called 'X-pol' data. This set of data can be used to cross check the data analysis procedures. From the definition of the polarized cross section, equation (1.2) the asymmetry of two cross sections can be written as:

$$\Sigma' = \frac{\frac{d\sigma}{d\Omega}(\theta,\Phi_1) - \frac{d\sigma}{d\Omega}(\theta,\Phi_2)}{\frac{d\sigma}{d\Omega}(\theta,\Phi_1) + \frac{d\sigma}{d\Omega}(\theta,\Phi_2)} = \frac{P\,I_1(\theta)(\cos 2\Phi_1 - \cos 2\Phi_2)}{2I_0 + P\,I_1(\theta)(\cos 2\Phi_1 + \cos 2\Phi_2)} , \tag{5.17}$$

for Φ_1 =43°, Φ_2 =133° and $P = 1$, this equation reduces to

$$\Sigma' = 0.0698\,\frac{I_1}{I_0} = 0.0698\,\Sigma . \tag{5.18}$$

Since the asymmetry is less than 0.5 for all the energies, this cross section asymmetry from the 'X-pol' runs should be close to zero for all energies. This data set was analysed in the same way as normal data runs and the asymmetries were calculated. The results, shown in

Figure 5-6, are consistent with zero. Therefore, this provides a good cross check of the data analysis.

5.5 Systematic Uncertainties in the Absolute Cross Section

A number of the parameters that enter the calculation of the cross section have uncertainties associated with them. These have been kept separate from the errors listed in Table 5-2 and Table 5-3 since they constitute a 'systematic' scale error in the cross section. The errors listed in Table 5-2 and Table 5-3 include statistical error and polarization uncertainty. The polarization independent systematic errors are listed in Table 5-4. Since they are independent of one another, they can be combined in quadrature to yield a net systematic error of 8.3%. All but the gamma ray polarization uncertainty cancels out of the asymmetry in Table 5-3.

Table 5-4: Components of Systematic Uncertainty

Source	Uncertainty
Simulation of Target thickness	
solid angle	
multiple scattering	
γ-spectrometer efficiency	6%
π^0 background separation	5%
Flux normalization	1%
Random correction	1%
Drift chamber efficiency	1%
P-bars efficiency	1%
Gamma ray polarization	2%
Combined	8.3%

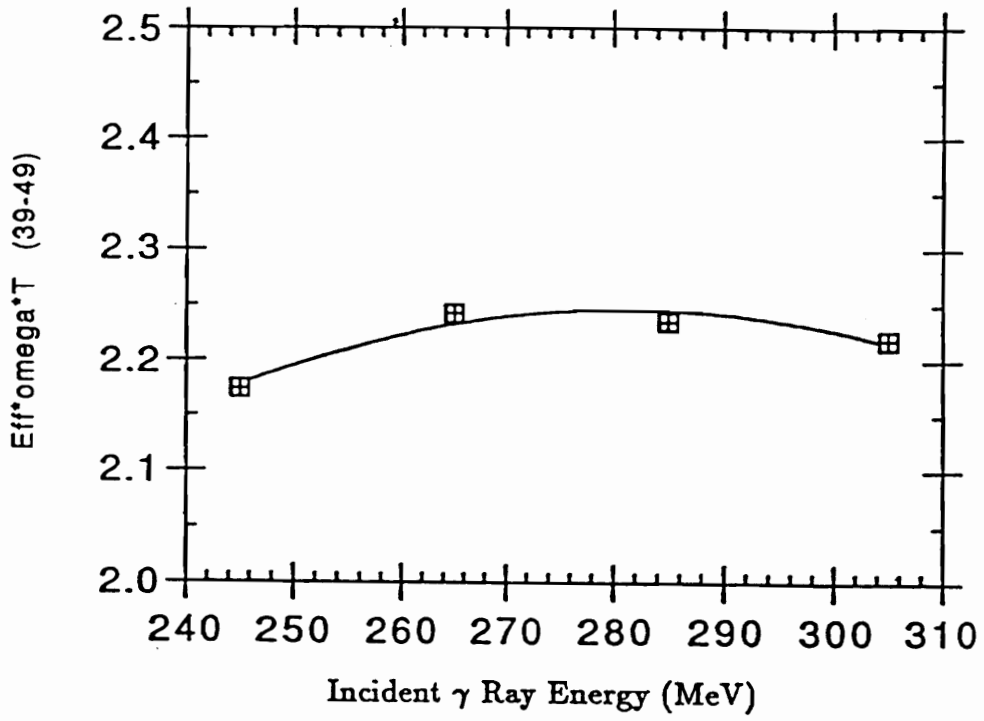

Figure 5-1: The effective gamma spectrometer acceptance from Monte Carlo simulation, folded with the detector efficiency and the target thickness (in $sr \times mm$), for θ_p =39° —49°, is shown as a function of incident gamma energy.

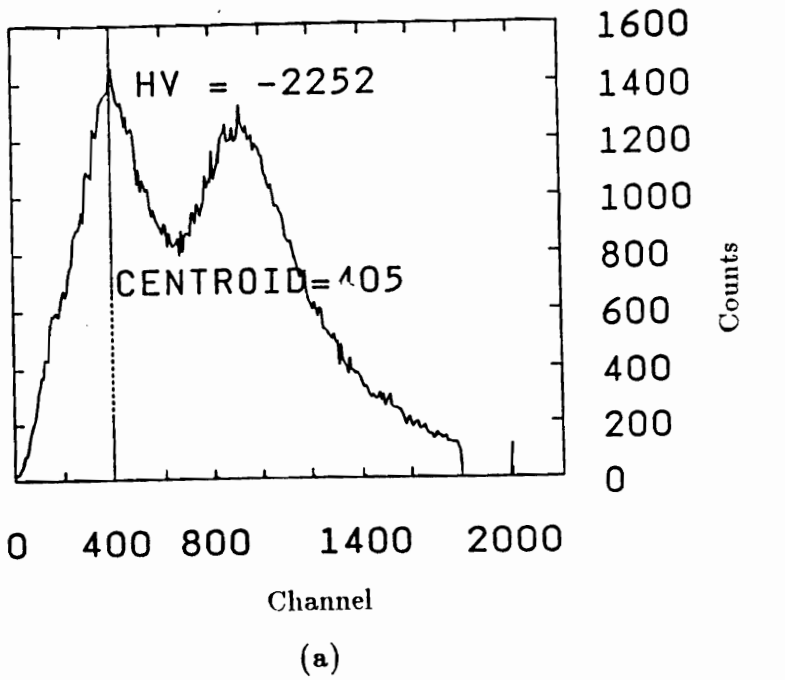

(a)

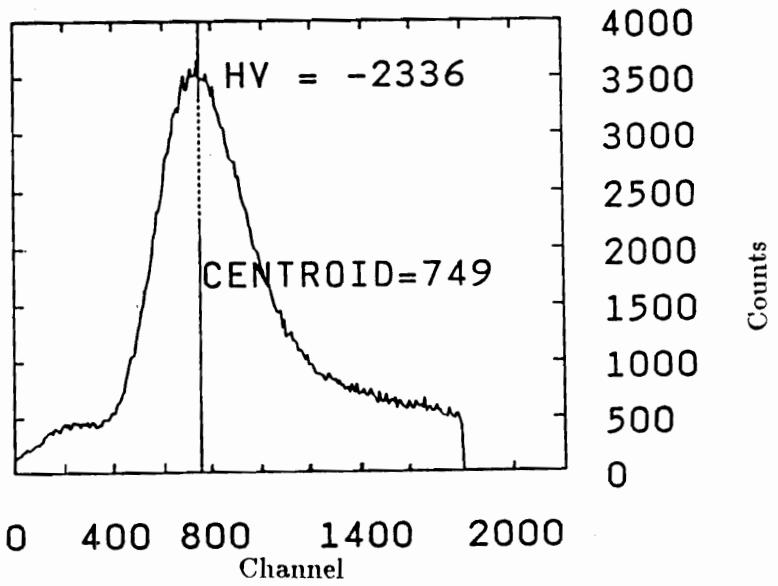

(b)

Figure 5-2: Spectra of the CG3 gamma beam flux monitor. (a): The spectrum of the charged particle veto scintillator (PCV). On the left is the single charged particle peak. On the right are the two charged particle peaks. The marked channel is number 400. (b): The spectrum of the charged particle accepting scintillator. The peak is from the pairs created by γ-rays in the convertor. The marked channel is number 750.

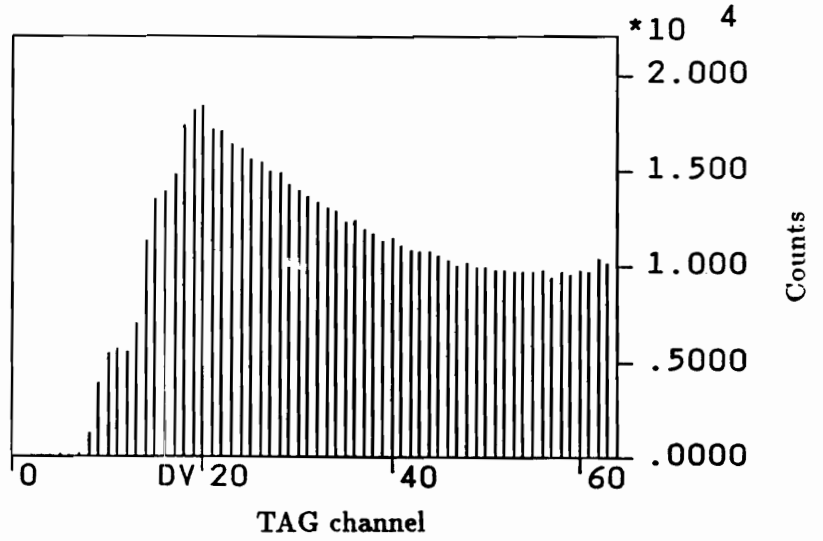

(a)

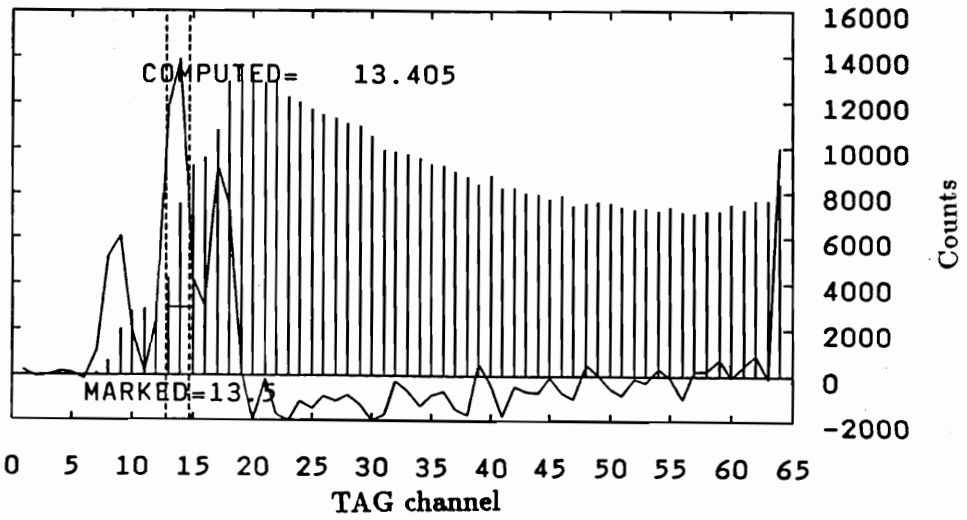

(b)

Figure 5-3: The LEGS γ-ray spectrum as a function of TAG channel. Lower TAG channel corresponds to higher γ-ray energy. The left edge is the Compton backscattering edge, which is a superposition of three slightly different edges. (b): The position of the Compton edge is obtained by differentiating the spectrum. The middle edge is used to get the edge position.

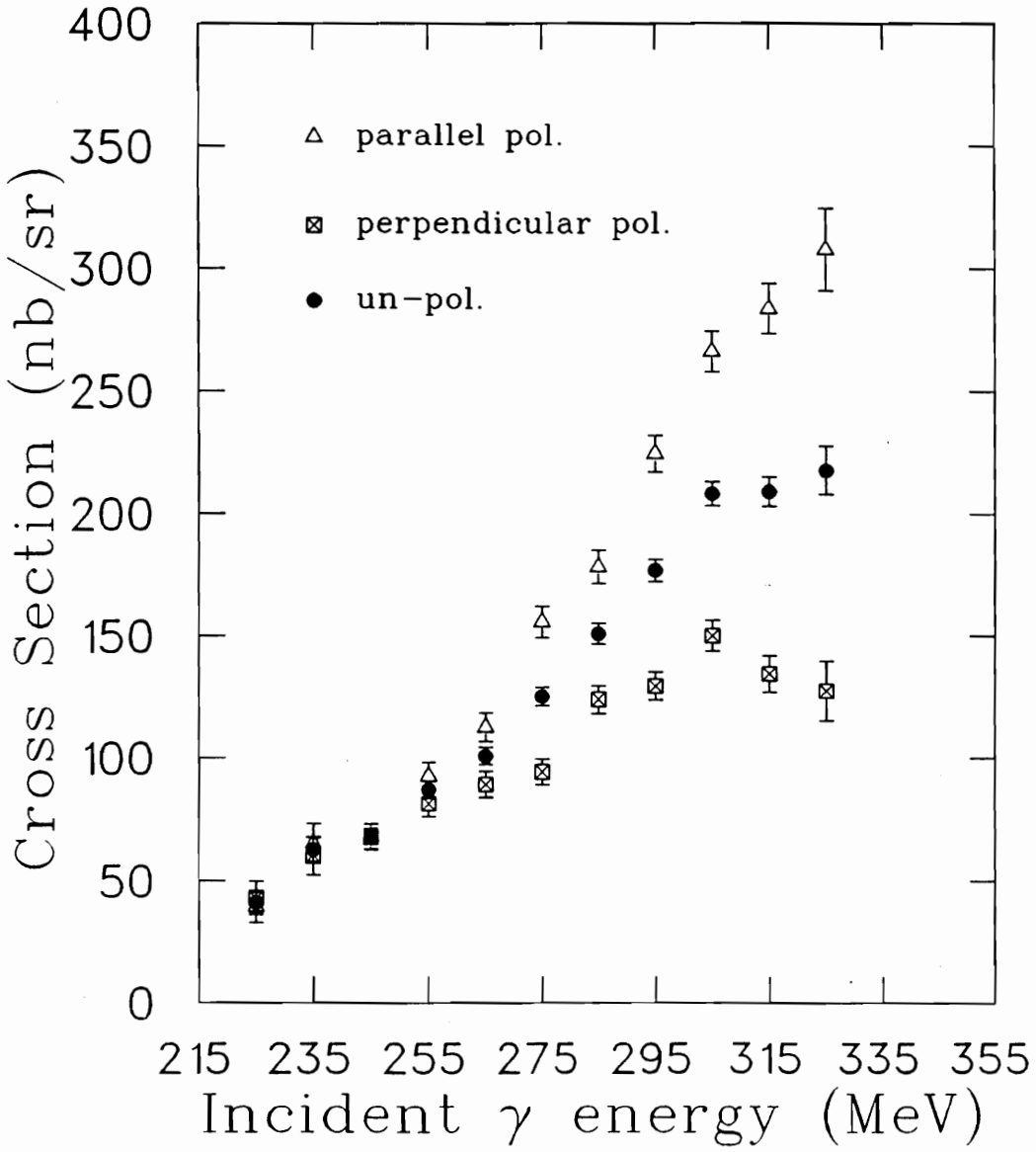

Figure 5-4: Polarized and unpolarized proton Compton scattering differential cross section at 90° CM as a function of the incident gamma energy. The open triangles are for photon polarization parallel to the reaction plane. The squares are for photon polarization perpendicular to the reaction plane.

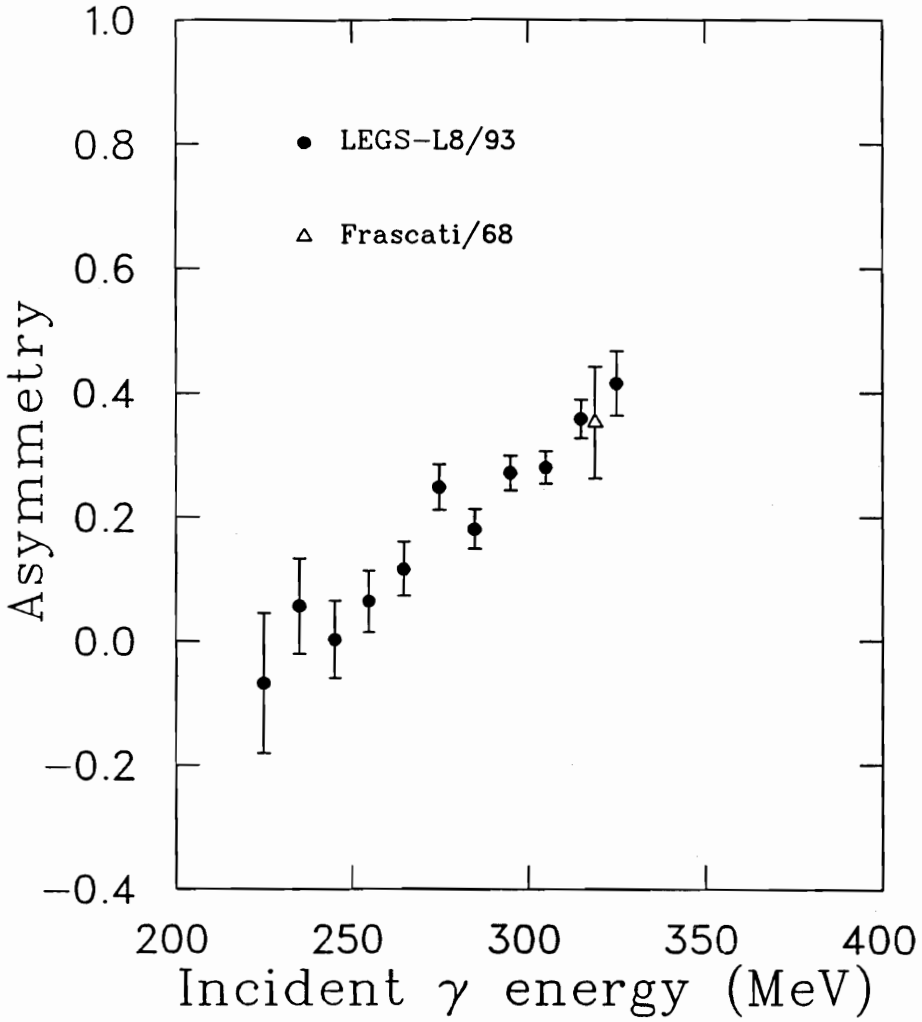

Figure 5-5: Proton Compton scattering polarization asymmetry as a function of incident photon energy at 90° CM. The only other datum is also shown as a triangle [11].

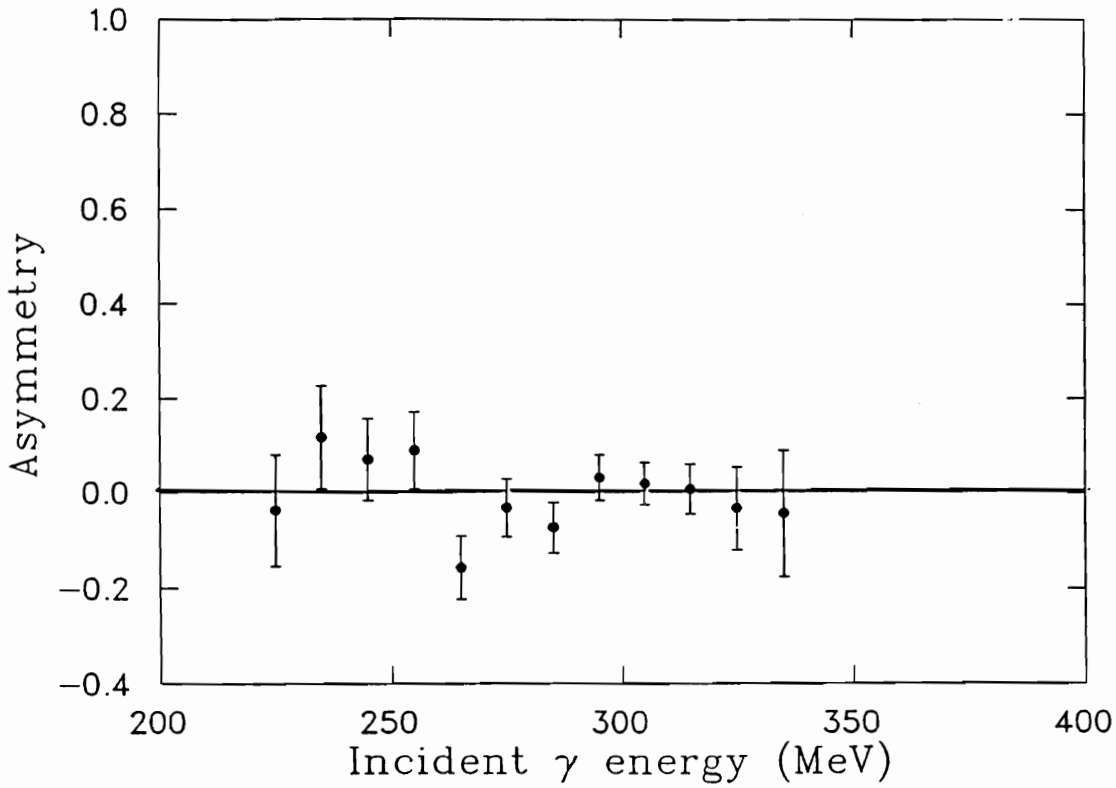

Figure 5-6: The asymmetry from the X-pol data as a function of incident γ-ray energy. The X-pol data are analysed in the same manner as the normal data. The X-pol asymmetries are zero within statistical fluctuation, which is consistent with predictions from the polarized cross section. This provides a cross check of the analysis.

Chapter 6

Comparision of Results with Theory and Previous Data

6.1 Comparison with Previous Data

The present data are compared with previous data at 90° CM around the Δ resonance in this section. Three sets of data from the 1960's, the data from a group at University of Bonn (Bonn data) [9], and the recently published data from the Saskatchewan Accelerator Laboratory group (SAL data) [10] are shown in Figure 6-1 along with present results.

The old data from De Wire *et al.* [6], Nagashima and Gray *et al.* have large statistical errors and poor energy resolution. Each data set covered only one or two energies. These data are considerably lower than the present data at the Δ resonance. Before the newly published SAL data, the Bonn data were the best available data for many years. However, the Bonn data still had relatively poor energy resolution. The Bonn data agree with the LEGS data below 280 MeV, but at the Δ peak it is smaller than the present data. As pointed out by Pfeil *et al.* [40], the Bonn data around 320 MeV exhaust the unitary bound, leaving no room for real parts of the scattering amplitudes (Section 3).

The SAL data have much improved energy resolution but the statistical errors are larger than the LEGS data. The incident photon energy of the SAL data goes up to 290 MeV, just below the Δ resonance. The present experiment measured cross sections up to 325 MeV, the peak of the Δ resonance. The present results are in agreement within statistical error with the SAL data. The energy binning of LEGS data, ± 5 MeV for all experimental points, is considerably better than previous data (except for the SAL data).

All the previous cross sections are unpolarized and the measured polarized cross sections have no previous data to compare with. The asymmetries from the present experiment can be compared with the only datum from Frascati [11], shown in Figure 6-5. This datum agrees with LEGS data but has large errors. The present experiment measured the energy dependence of the photon asymmetry for the first time. The unpolarized cross sections are not sensitive to the details of different theories, but photon asymmetry is sensitive to the details of different theories.

6.2 Proton Compton Scattering Formalism

In the Δ resonance region the Feynman diagrams for proton Compton scattering include the Born terms, the resonance terms, the tails of higher energy N^* resonances and the Low amplitude term (Figure 6-2). The Born and Low terms can be calculated explicitly from the Feynman diagram. But the Δ and higher resonance terms cannot be evaluated directly because of the lack of knowledge about the coupling constants of these terms. However, there are a number of phenomenological theories that can calculate the proton Compton scattering cross section and other observables. The basic formalism of partial-wave decomposition is briefly described in this section.

A convenient way to describe proton Compton scattering is to use the helicity amplitudes. The partial-wave amplitudes can then be expressed in terms of helicity amplitudes. Let the helicity of the initial and final photon be λ_1 and λ_2, and let μ_1 and μ_2 be the spin projection

for initial and final proton, respectively. A photon has helicity ± 1 and proton has spin projection $\pm\frac{1}{2}$. Initial and final systems can be distinguished by the helicity differences: $\lambda = \lambda_1 - \mu_1$ and $\mu = \lambda_2 - \mu_2$, respectively. Both initial and final system have four different helicity states, $\lambda, \mu = \pm\frac{3}{2}, \pm\frac{1}{2}$. Thus there are sixteen helicity amplitudes. eight of them are not independent due to parity conservation. In the remaining eight amplitudes, two are not independent from time-reversal invariance. So the number of independent helicity amplitudes reduces to six. They are defined by the following equations [40]:

$$\phi_1 = \frac{1}{8\pi W} < 1, \tfrac{1}{2}|T|1, \tfrac{1}{2} > \equiv \phi_{\frac{1}{2},\frac{1}{2}} \ , \quad \phi_2 = \frac{1}{8\pi W} < -1, -\tfrac{1}{2}|T|1, \tfrac{1}{2} > \equiv \phi_{\frac{1}{2},-\frac{1}{2}} \ ,$$

$$\phi_3 = \frac{1}{8\pi W} < -1, \tfrac{1}{2}|T|1, \tfrac{1}{2} > \equiv \phi_{\frac{1}{2},-\frac{3}{2}} \ , \ \phi_4 = \frac{1}{8\pi W} < 1, -\tfrac{1}{2}|T|1, \tfrac{1}{2} > \equiv \phi_{\frac{1}{2},\frac{3}{2}} \ , \tag{6.1}$$

$$\phi_5 = \frac{1}{8\pi W} < 1, -\tfrac{1}{2}|T|1, -\tfrac{1}{2} > \equiv \phi_{\frac{3}{2},\frac{3}{2}} \ , \ \phi_6 = \frac{1}{8\pi W} < -1, \tfrac{1}{2}|T|1, -\tfrac{1}{2} > \equiv \phi_{\frac{3}{2},-\frac{3}{2}} \ .$$

where W is the total CM energy of the system.

The helicity amplitudes can be expressed in terms of partial-wave Compton amplitudes $f_{EE}^{L\pm}, f_{EM}^{L\pm}, f_{ME}^{L\pm}, f_{MM}^{L\pm}$. Here $f_{EM}^{L\pm}$ denotes the amplitude for the photon angular momentum L and the total γN angular momentum $J = L \pm \frac{1}{2}$, where in the initial state the photon is in an electrical mode and the photon in the final state is in a magnetic mode. Other amplitudes have analogous meanings. The expansions of the helicity amplitudes are given by:

$$\begin{aligned}
\phi_{1,2} \ = \ & \tfrac{1}{2}\sum_{L=0}^{\infty}(L+1)((L+2)^2(f_{EE}^{(L+1)-} \pm f_{MM}^{(L+1)-}) \\
& \pm L^2(f_{EE}^{L+} \pm f_{MM}^{L+}) \mp 2L(L+2)(f_{EM}^{(L+)} \pm f_{ME}^{(L+)}))d_{\frac{1}{2},\pm\frac{1}{2}}^{L+\frac{1}{2}}
\end{aligned}$$

$$\begin{aligned}
\phi_{3,4} \ = \ & \tfrac{1}{2}\sum_{L=1}^{\infty}(L+1)\sqrt{L(L+2)}((L+2)(f_{EE}^{(L+1)-} \mp f_{MM}^{(L+1)-}) \\
& \pm L(f_{EE}^{L+} \mp f_{MM}^{L+}) \mp 2(f_{EM}^{(L+)} \mp f_{ME}^{(L+)}))d_{\frac{1}{2},\mp\frac{3}{2}}^{L+\frac{1}{2}}
\end{aligned} \tag{6.2}$$

$$\phi_{5,6} = \frac{1}{2}\sum_{L=1}^{\infty}(L+1)L(L+2)((f_{EE}^{(L+1)-} \pm f_{MM}^{(L+1)-}) \pm (f_{EE}^{L+} \pm f_{MM}^{L+}) \pm 2(f_{EM}^{(L+)} \pm f_{ME}^{(L+)}))d^{L+\frac{1}{2}}_{\frac{1}{2},\pm\frac{1}{2}} ,$$

where $\phi_{1,3,5}$ correspond to the upper lines and $\phi_{2,4,6}$ correspond to the lower lines.

In the helicity formalism the proton Compton scattering differential cross section $\frac{d\sigma}{d\Omega}$ and photon polarization asymmetry Σ in the CM system, can be expressed in simple forms as follows:

$$\frac{d\sigma}{d\Omega} = \frac{1}{2}(|\phi_1|^2 + |\phi_2|^2 + 2|\phi_3|^2 + 2|\phi_4|^2 + |\phi_5|^2 + |\phi_6|^2) , \tag{6.3}$$

$$\Sigma = \frac{Re((\phi_1 + \phi_5)\phi_3^* + (\phi_2 - \phi_6)\phi_4^*)}{\frac{d\sigma}{d\Omega}} \tag{6.4}$$

In the differential cross section the helicity amplitudes add up incoherently and there are no interference terms between them.

Proton Compton scattering is related to π^0 and π^+ photoproduction by unitarity. In the Δ region below 400 MeV, two pion intermediate states are quite small and only the πN intermediate state is usually taken into account. The unitarity relation for the partial-wave Compton amplitudes is given by the following equations [39, 40]:

$$Im(f_{MM,EE}^{L+}) = q\sum_c \left\{ \begin{array}{c} |M_{L+}^c|^2 \\ |E_{(L+1)-}^c|^2 \end{array} \right\} + k(L+1)\{L|f_{MM,EE}^{L+}|^2 + (L+2)|f_{ME,EM}^{L+}|^2\}$$

$$Im(f_{MM,EE}^{L+1}) = q\sum_c \left\{ \begin{array}{c} |M_{(L+1)-}^c|^2 \\ |E_{L+}^c|^2 \end{array} \right\} + k(L+1)\{(L+2)|f_{MM,EE}^{(L+1)-}|^2 + L|f_{ME,EM}^{(L+1)-}|^2\} \tag{6.5}$$

$$Im(f^{L+}_{ME,EM}) = \mp q \sum_c Re \left\{ \begin{array}{c} M^c_{L+} E^{c\,*}_{L+} \\ M^c_{(L+1)-} E^{c\,*}_{(L+1)-} \end{array} \right\}$$
$$+k(L+1)Re\left\{L(f^{L+}_{MM,EE} + (L+2)f^{(L+1)-}_{EE,MM})f^{L+\,*}_{ME,EM}\right\}$$

where $E_{L\pm}(M_{L\pm})$ are the single pion photoproduction amplitudes where the initial photon is in the electrical (magnetic) mode, and the orbital angular momentum for the πN system is L, while the total angular momentum for the system is $J = L \pm \frac{1}{2}$. The upper (lower) line corresponds to the first (second) amplitude on the left hand side. The summation on c is over the π^+ and π^0 photoproduction channels. For the Δ resonance region, the second terms in equation (6.5) are very small, about 0.6% [39], and are negligible. Therefore the imaginary parts of the Compton amplitudes are completely determined only by the photoproduction amplitudes through unitarity.

6.3 Unitary Bound

The unitary bound was first introduced in reference [40]. The dominant multipoles of pion photoproduction are relatively well known and these determine the imaginary parts of Compton scattering amplitudes. Since the helicity amplitudes add incoherently in the unpolarized cross section, a lower bound for the cross section is deduced by putting the real parts of the helicity amplitudes to zero.

Pfeil *et al.* found that, at energies lower than 300 MeV and higher than 380 MeV, previous Compton scattering data are above the unitary bound. But near 320 MeV and at 90° CM, previous data are smaller than the bound, as calculated from the most probable values for the pion multipoles, and the more recent Bonn data are lower still. In fact, they are at the lower limit constructed from the extreme values allowed by the errors associated with the multipoles. This leaves little room for the real parts of Compton multipoles [40].

The unitary bound as a function of incident energy calculated with the Pfeil multipoles [36, 40], PRS bound, is shown in Figure 6-3. The LEGS data are above the bound at all

energies. In a recent paper, ref.[39], Benmerrouche and Mukhopadhyay re-calculated the unitary bound (BM bound) with new pion photoproduction multipoles. At around 320 MeV, the Bonn data still overlaps with the lower error limit of the BM unitary bound, even considering the poor energy resolution of the data (Figure 6-3). The newly published data from the Saskatchewan group [10] are larger than the bound, but the incident photon energy only goes up to 290 MeV. The present data cover the peak of Δ resonance and are larger than the unitary bound at all energies. The closeness to the bound at 325 MeV (comparing the stars with solid circles in Figure 6-3) suggests very small contributions from real parts of the Compton amplitudes near the peak of the resonance. The differences are larger at lower energies, thus allowing room for larger real parts of the Compton amplitudes.

6.4 Approches to Calculate Compton Amplitudes

6.4.1 Fixed-t Dispersion Relation Model and Simultaneous Fit

While the imaginary parts of Compton amplitudes can be calculated from existing pion photoproduction data, the determination of the real parts proved to be more difficult. In principle, the real parts can be determined by dispersion relations if the imaginary parts are known. However, subtraction functions are needed to reproduce the correct low-energy limit and asymptotic behaviour, but proper subtraction functions are difficult to obtain. In the work of Pfeil, Rollnik and Stankowski [40], fixed-t dispersion relations for the Hearn-Leader(HL) amplitudes A_i are used. There are six HL amplitudes. The dispersion relations for A_1, A_2, A_3, A_6 are given by ([40]):

$$A_i(s,t) = A_i^{(Born)} + A_i^{(Low)} + F_i(t) + \frac{1}{\pi}\int_{(M+\mu_\pi)^2}^{\infty} ds' \frac{Im\, A_i(s',t)}{s'-M^2}\left(\frac{s-M^2}{s'-s} + \frac{u-M^2}{s'-u}\right), \quad (6.6)$$

where $A_i^{(Born)}$ and $A_i^{(Low)}$ are from the Born and Low terms in Figure 6-2, and they can be calculated explicitly. $F_i(t)$ is the subtraction function; s, u, t are the usual Mandelstam

variables, and M is proton mass. A_4 and A_5 satisfy the un-subtracted dispersion relations. The HL amplitudes are connected with the helicity amplitudes by the following relations:

$$\begin{aligned}
8\pi W\phi_1 &= \cos\tfrac{1}{2}\theta\,(M(A_2 - A_1) - k_0 W(A_5 - A_4) - 2k_0 W A_6)\ , \\
8\pi W\phi_2 &= -\sin\tfrac{1}{2}\theta\,(E(A_2 + A_1) - k_0 M(A_5 + A_4) - 2k_0 A_3)\ , \\
8\pi W\phi_3 &= \cos\tfrac{1}{2}\theta\,(M(A_2 + A_1) - k_0 W(A_5 + A_4))\ , \\
8\pi W\phi_4 &= -\sin\tfrac{1}{2}\theta\,(E(A_2 - A_1) - k_0 M(A_5 - A_4))\ , \\
8\pi W\phi_5 &= \cos\tfrac{1}{2}\theta\,(M(A_2 - A_1) - k_0 W(A_5 - A_4) + 2k_0 W A_6)\ , \\
8\pi W\phi_6 &= \sin\tfrac{1}{2}\theta\,(E(A_2 + A_1) - k_0 M(A_5 + A_4) + 2k_0 A_3)\ ,
\end{aligned} \tag{6.7}$$

where θ is the CM scattering angle and k_0 the 3-momentum of initial proton in the CM frame. In the treatment of [40], the $F_i(t)$ term is set to zero for all A_i. From the imaginary Compton amplitude obtained from (6.5), the imaginary parts of ϕ_i and A_i can be obtained from equations (6.2) and (6.7). The real parts are obtained by (6.6). The unpolarized cross sections and asymmetries calculated with the Pfeil multipoles by Sandorfi [36, 40, 42], labeled as PRS fixed-t, are shown in Figure 6-4 and Figure 6-5.

Another approach by Pfeil *et al.* to obtain the Compton amplitudes is by simultaneously fitting both the photoproduction and Compton scattering data. In the fit the partial-wave amplitudes E_{0+}, M_{1+}, etc. and f^{1-}_{EE}, f^{1+}_{MM} etc. were allowed to vary freely up to the unitarity constraint. For Compton scattering interpolated values of the differential cross section data from the Bonn group [9] and the Frascati asymmetry datum [11] are used. The calculated unpolarized cross sections and asymmetries using the fitted multipoles [36, 42], labeled as PRS Sim. fit, are shown in Figure 6-4 and Figure 6-5.

6.4.2 Finite-Energy Dispersion Relation Model

In the approach of L'vov [38], dispersion relations of the finite-energy type are used. In this approach the subtraction functions are not used. Instead, sum-rules are used to express

the amplitudes in terms of a sum of contributions from the low energy region and from the asymtotic region. For the two amplitudes involving a photon helicity flip, the amplitudes do not fall off rapidly with energy and are estimated with Regge theory. In the end two parameters that come from the sum rules remain, which are the electric polarizability α and magnetic polarizability β of the proton. The sum of α and β are fixed by the sum rule: $\alpha + \beta = 14.2 \times 10^{-43}\ cm^3$. So the only free parameter in this approach is the difference: $\alpha - \beta$.

In the finite-energy dispersion relation the real part of amplitude is expressed as the sum of three terms. The first term is from the Born diagrams. The second term is an integration of the imaginary part in the energy region from pion threshold to 1.5 GeV. The third term is the asymptotic contribution expressed in terms of the parameters of the asymptotic region. The imaginary parts of the amplitudes are determined by the unitarity relations given above. The polarizability difference, $\alpha - \beta$,is determined by a fit to experimental data, which is $5—16 \times 10^{-43} cm^3$ as given in [38]. But the unpolarized cross section and asymmetry are not sensitive to $\alpha - \beta$ at 90° CM. The unpolarized cross section, corresponding to $\alpha - \beta = 6 \times 10^{-43}\ cm^3$, is shown with present results in Figure 6-4.

6.4.3 Isobar Model

Another approach of determining the Compton amplitude, by Ishii *et al.* [41], is different from the approaches mentioned above. In this model each Compton amplitude is decomposed into two components as follows:

$$A = A^R + A^B\, e^{-C(1-\cos\theta)}, \tag{6.8}$$

where A^R is the contribution from the resonance and A^B is the contribution from the Born terms. The factor $e^{-C(1-\cos\theta)}$ is used to damp the Born terms, since its contribution to the differential cross section appeared to be too large at the backward angles in the work of [41]. The parameter C was obtained by fitting experimental data. The Born contribution

A^B was directly calculated from Feynman diagrams. The resonance contribution A^R is obtained by a Breit-Wigner type relation. The results based on this model [36, 42] are shown in Figure 6-4 and Figure 6-5 along with present results.

From Figure 6-4 it can be seen that the theoretical calculations from the above models all agree with the unpolarized cross section data to some extent. The model from L'vov appears to agree best in this energy region. The results from the isobar model and the simultaneous fit are slightly lower than the data above 300 MeV, but agree well below 300 MeV. The results from the fixed-t dispersion model agree well at the resonance peak, but are higher than the data below the peak.

Comparing the photon polarization asymmetries with theories in Figure 6-5, it can be seen that both calculations from the L'vov model and fixed-t dispersion relation agree well with the data. The energy dependence of the asymmetry from these two models is slightly different. The results from the isobar model are qualitatively different from the present data, although its unpolarized cross section agrees relatively well. The data suggests that some assumptions used in the isobar model are at fault. The results from the simultaneous fits do not agree with the data at some energies, which suggests that the input pion photoproduction data or the early Compton data that were used in the fits are not accurate. The asymmetry data shows more sensitivity to the details of models than the unpolarized cross sections, as expected.

6.5 The cross section ratio: $\frac{d\sigma_\parallel}{d\sigma_\perp}$

In the Δ region it is believed that the dominant multipole is the magnetic dipole amplitude. One of the important model-independent results of Compton scattering using polarized cross sections is given in ref. [3, 39]. It states that in the limit of all Compton amplitudes, other than f^{1+}_{MM} tending to zero, the ratio of parallel and perpendicular cross sections is only a

function of the scattering angle θ:

$$\frac{d\sigma_{\parallel}}{d\sigma_{\perp}} \simeq \frac{5}{3\cos\theta^2 + 2} \tag{6.9}$$

For θ =90°, this relation simplifies to

$$\frac{d\sigma_{\parallel}}{d\sigma_{\perp}}(\theta = 90°) \simeq 2.5 \; . \tag{6.10}$$

The present experiment gives the first measurement of the ratio $\frac{d\sigma_{\parallel}}{d\sigma_{\perp}}$ as a function of incident energy, shown in Figure 6-6(a). At the resonant energy around 325 MeV the data are very close to 2.5. But slightly below the peak, at 305 MeV, the ratio drops considerably. This fact suggests that other multipoles have some contributions at the resonance, but are accidentally cancelled out at the peak.

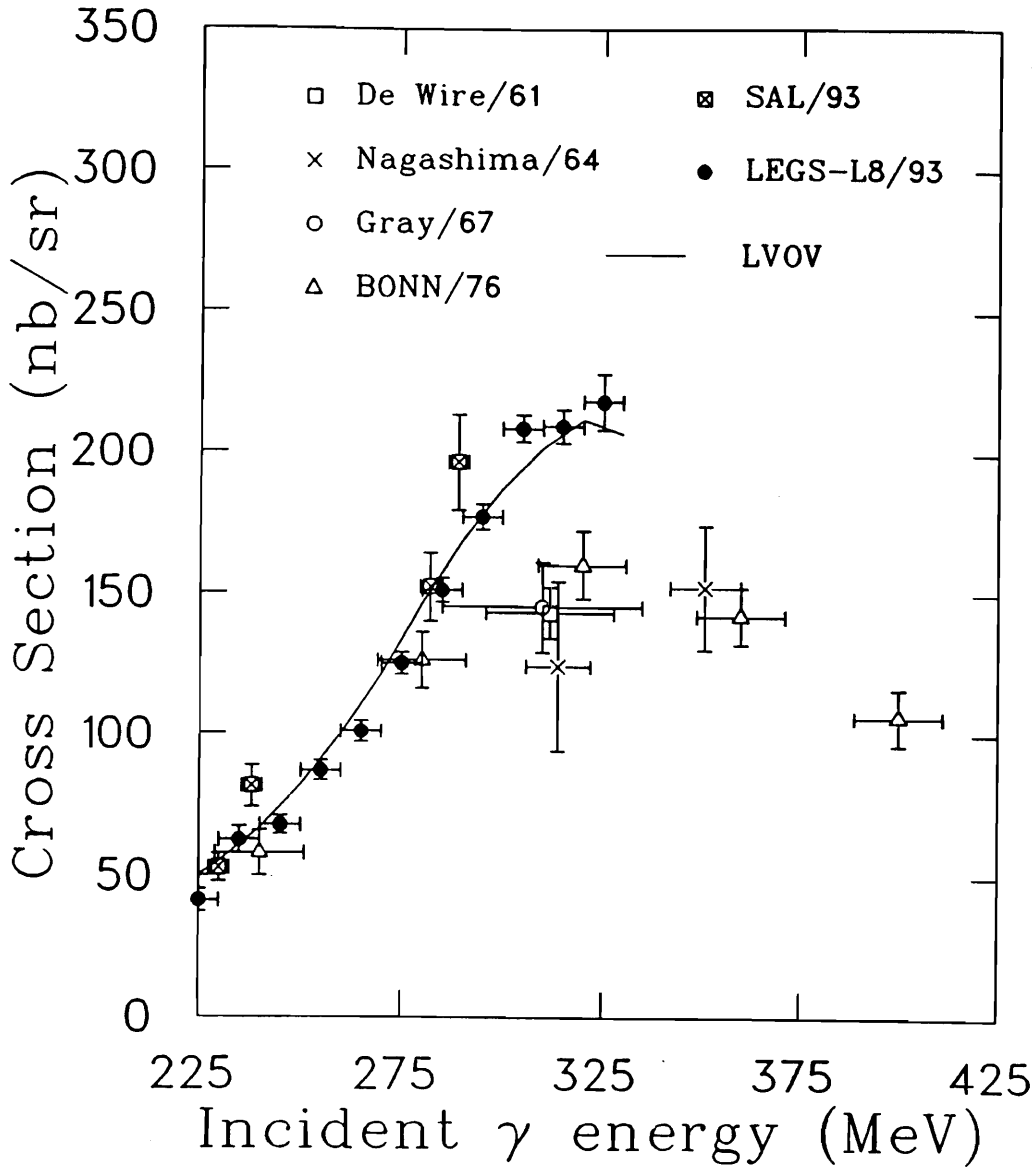

Figure 6-1: Comparison of the unpolarized differential cross section at CM 90° with previous data. The present data have better statistics and energy resolution (except for SAL data), with energy up to the resonance peak. The sources of these data are: De Wire *et al.* [6]; Nagashima, [7]; Gray *et al.* [8]; Bonn data, [9]; SAL data, [10].

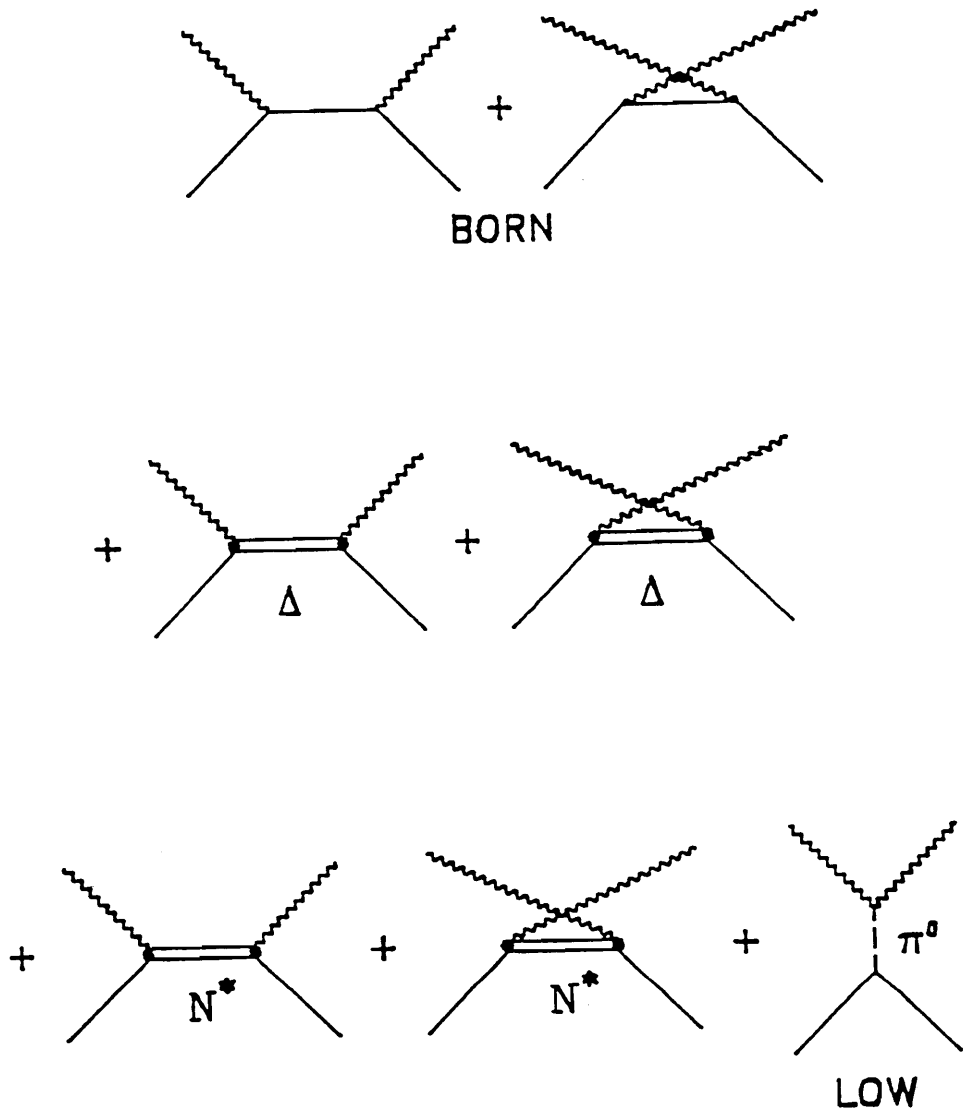

Figure 6-2: Feynman diagrams for proton Compton scattering around the Δ resonance. In the Low term only the π^0 exchange term is included here.

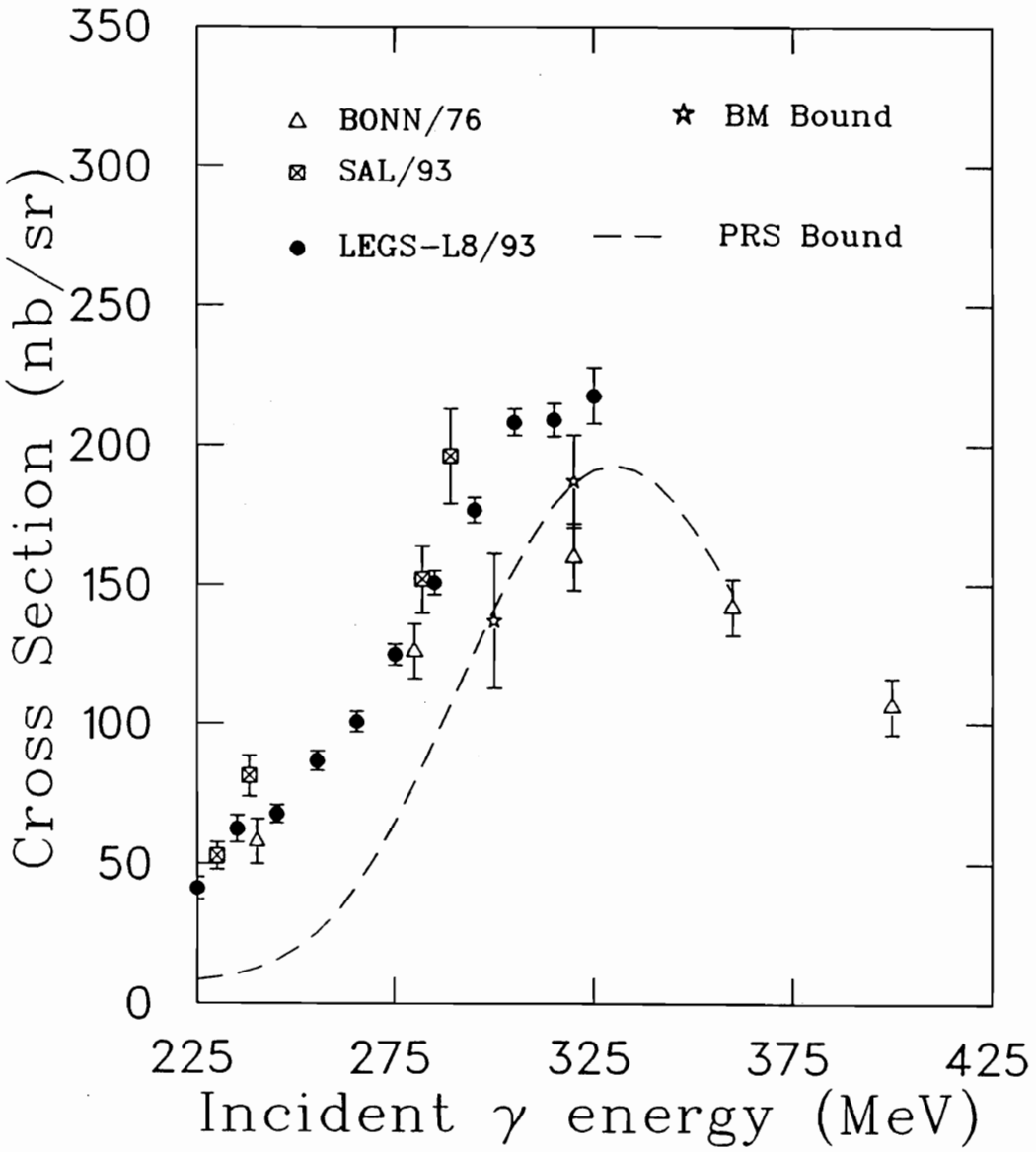

Figure 6-3: The unitary bound for Compton scattering around the Δ resonance at 90° CM. Below 300 MeV all three sets of data are above the unitary bound. Around 320 MeV the Bonn data is smaller but the LEGS data is larger than the bound.

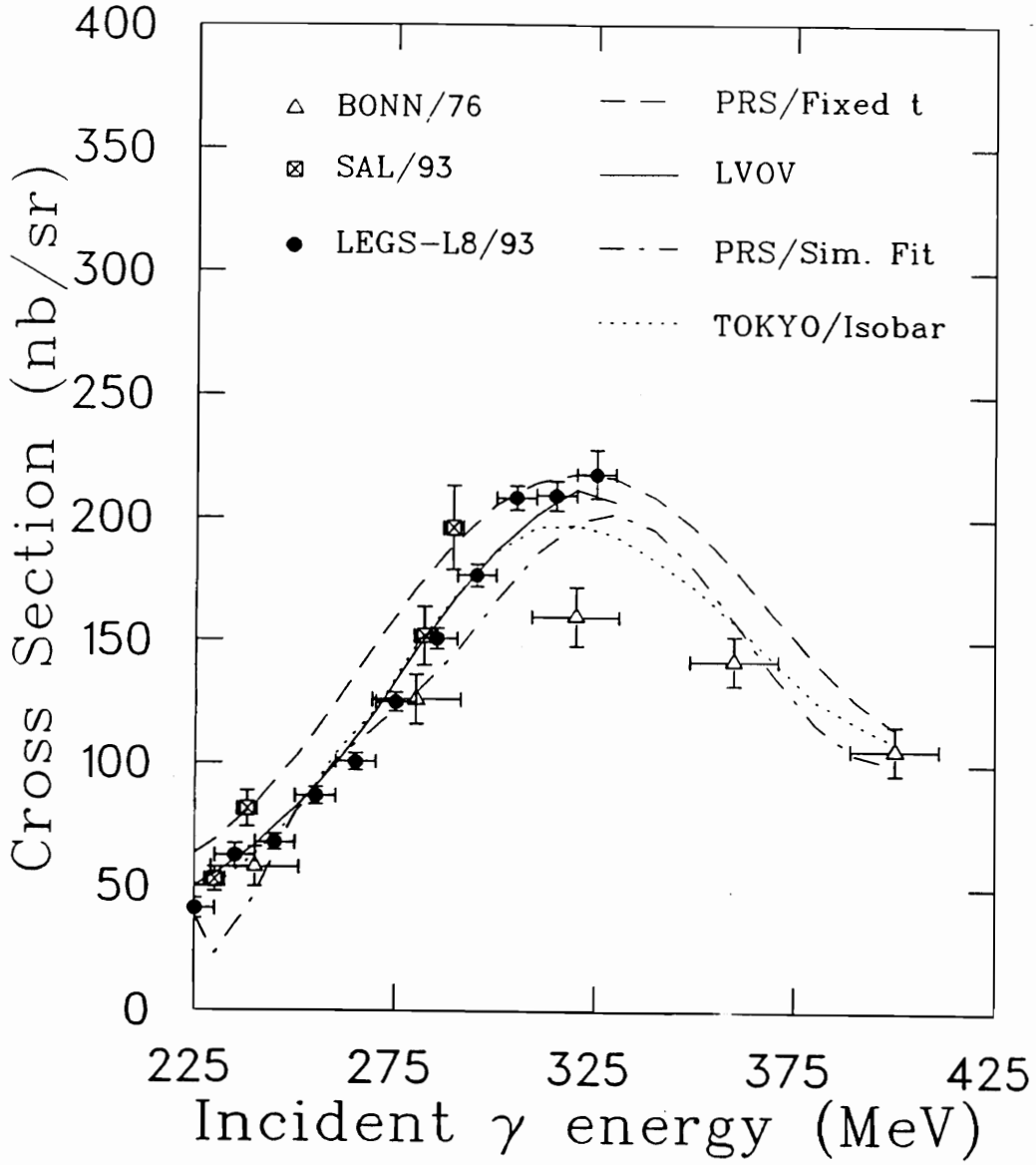

Figure 6-4: Comparison of the unpolarized differential cross section at CM 90° with theoretical calculations. The fixed-t dispersion calculation [36, 40] agrees well with the LEGS data at the Δ peak but is higher at lower energies. The simultaneous fits [36, 40] and the isobar model [36, 41] calculation agree reasonably well but are slightly lower at lower energies. The L'vov calculation [38] has excellent agreement with LEGS data at all energies.

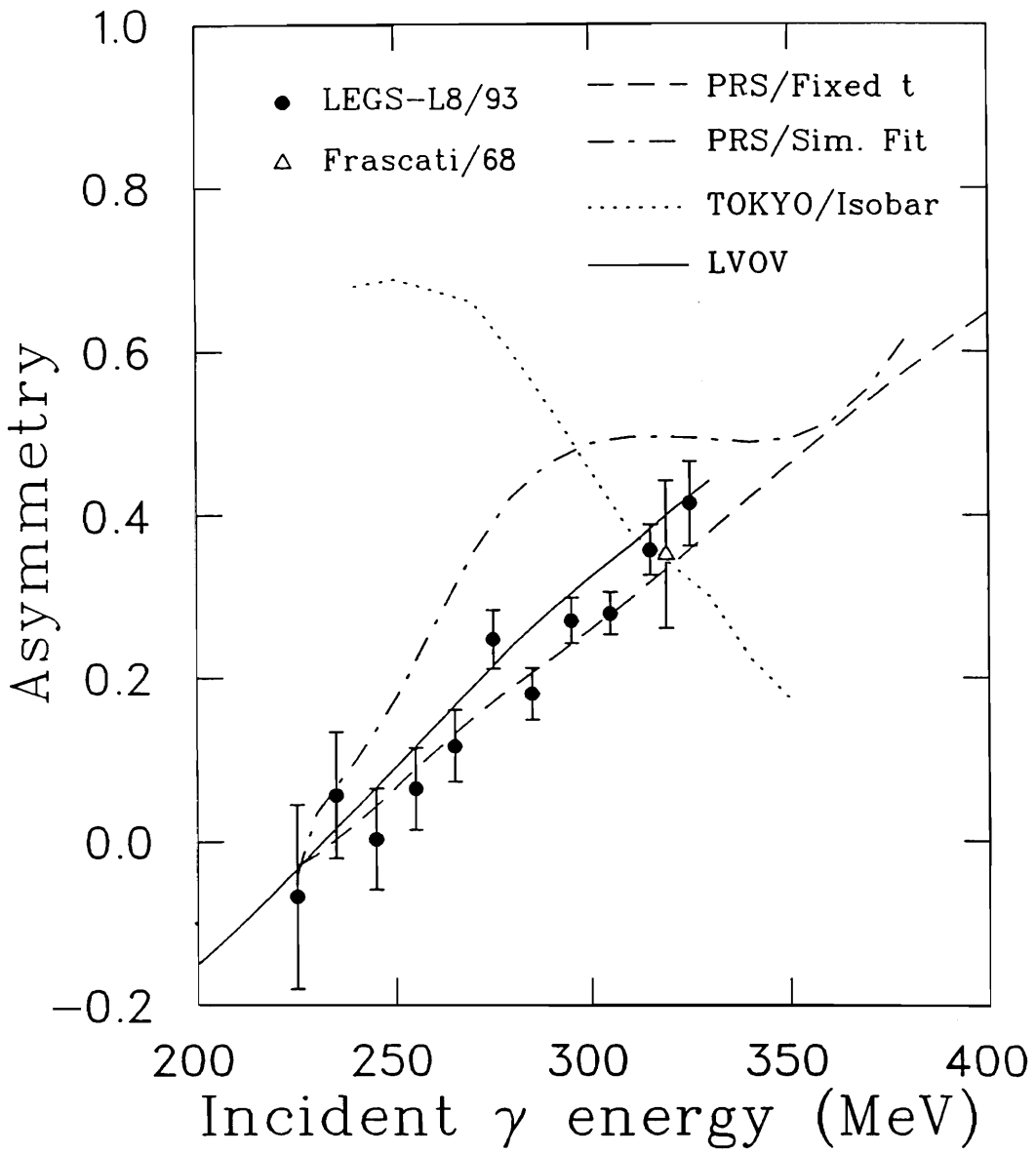

Figure 6-5: Proton Compton scattering polarization asymmetries as a function of incident photon energies at CM 90° compared with various theoretical calculations and the Frascati datum [11]. The LEGS data agree very well with the L'vov and fixed-t dispersion calculations and disagree with the Isobar calculation. The simultaneous fit calculation does not agree with the data.

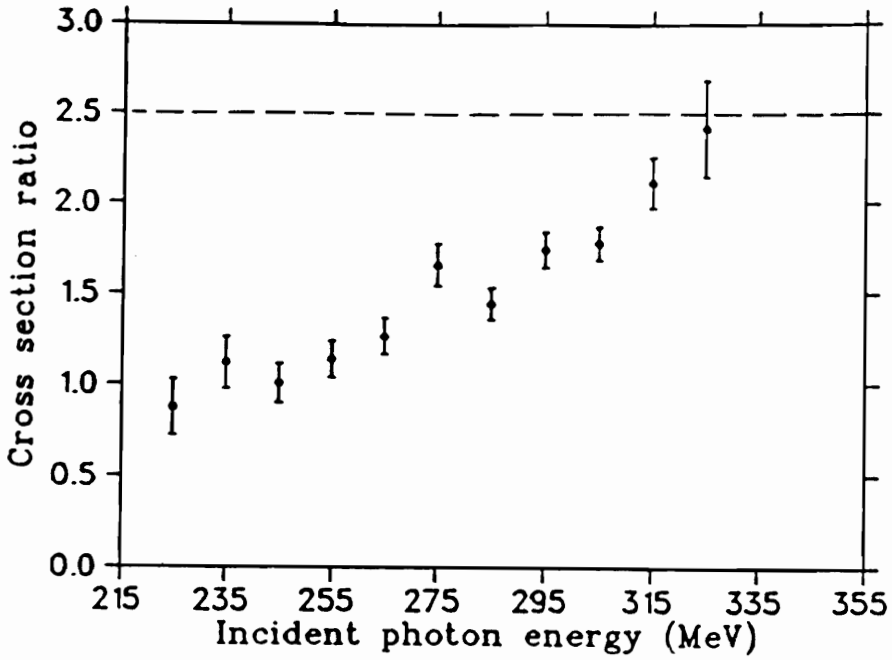

Figure 6-6: The ratio of the polarized cross sections $\frac{d\sigma_{\parallel}}{d\sigma_{\perp}}$ as a function of the incident photon energy. The dashed line shows the case when only f^{1+}_{MM} contributes. The ratio falls down considerably at about 20 MeV off the peak.

Chapter 7

Conclusions

The present experiment studied proton Compton stattering, the most elementary nuclear system examined by the most elementary probe, with the new generation gamma source obtained at LEGS. Polarized cross sections are now available for the first time from 225 MeV up to the Δ resonance peak, 325 MeV, at 90° in the CM system.

Comparing with previous unpolarized cross section data, the LEGS data have considerably better statistics. Except for the SAL data the small energy binning of LEGS data is superior. The present data agree with the SAL and Bonn data below 290 MeV. At the resonace peak the LEGS cross section is greater than all prevous measurements and is above the unitary bound, thus resolving the longstanding conflict between experimental data and theory at the resonance peak.

Semi-phenomenological dispersion models have been used to study Compton scattering for a long time. Although the imaginary parts of the Compton amplitudes used in these models are relatively well determined by unitarity relations with the existing pion photoproduction data, the real parts are difficult to obtain due to the substraction functions needed in some dispersion relations. The L'vov calculation agrees extremely well with the LEGS

data. For the unpolarized cross section the calculation from the isobar model and the PRS simultaneous fit agree with the data fairly well, but the results from the fixed-t dispersion model are too high except at the resonance energy.

Because the polarized photons can probe more details of Compton scattering, the photon asymmetry can distinguish between different models. Both $\frac{d\sigma_\parallel}{d\Omega}$ and $\frac{d\sigma_\perp}{d\Omega}$ were measured simultaneously in this experiment, so that the systematic errors in the cross section ratio and polarization asymmetry is supressed. Although the results of the isobar model agree fairly well with the unpolarized cross section, it is clear from the asymmetry data that some assumptions in the model are incorrect. Similarly, the simultanueous fit calculations agree with the unpolarized data reasonably well, but deviate from the asymmetry data. This suggests that the input data used for the fit are not accurate. On the contrary, the results from the fixed-t disspersion model agree with the asymmetry very well, but the unpolarized cross sections do not agree well. This disagreement suggests that this model should be modified.

The finite-energy dispersion model agrees with both unpolarized cross section and asymmetry data very well. This suggests that even the details of the model are quite resonable. However, this model is still semi-phenomenological and needs to obtain its free parameter, $\alpha - \beta$, from fitting experimental data. Moreover, because of the complexity of this theory, it is difficult to get the E2 excitation of the Δ from the 90° Compton scattering data alone. Therefore, the E2/M1 ratio, which relates to the D-state component or the deformation of the nucleon, is difficult to obtain from this model.

The model independent result of Compton scattering, which states that the ratio of the polarized cross sections, $\frac{d\sigma_\parallel}{d\sigma_\perp}$, is $\frac{5}{2}$ at 90° CM in the limit that only the f^{1+}_{MM} contributes, is compared with the data. It is found that below the resonance peak the ratio falls with energy considerably, suggesting significant cancellations from several multipoles other than f^{1+}_{MM} in the Δ region.

The measurement of the $E2/M1$ ratio in the Δ — N transition, resulting from the prediction

of the existence of tensor interaction between quarks, requires the measurement of the Compton cross section at other angles. Analysis for Compton scattering experiments for a much larger angular range is presently underway. When completed they will be used to determine the Compton multipoles, which in turn will provide important new information on $E2/M1$.

Compton scattering of the proton with polarized photons can potentially shed light on nucleon structure and the quark interaction in the non-perturbative domain. More theoretical work is called for in order to expolit the measured polarized cross sections and asymmetries. It is hoped that eventually a theory that can explain the Compton scattering observables from the underlying quark-gluon structure will emerge.

Bibliography

[1] F. Halzen,A.D. Martin *Quarks and Leptons* (1984).

[2] Gordon Kane, *Modern Elementary Particle Physics* (1987).

[3] A.M.Sandorfi *et al*, Scattering of Polarized Photon at Legs, *Invited Lecture at the International School on Intermediate Energy Nuclear Physics*, BNL Report No. 42331.

[4] J. Sakuri, *Modern Quantum Mechanics*

[5] T. Ericson and W. Weise, *Pion and Nuclei*, 1988

[6] J. W. De Wire *et al.* , Physics Review, **174**, 1665(1968).

[7] Y. Nagashima, Institute for Nuclear Study, Tokyo, Report No. INSJ-81, 1964(unpublished), quoted in Ref. [39].

[8] E. R. Gray and A.O. Hansen, Z. Phys. Rev., **160**, 1212(1967).

[9] Genzel, Jung, Wedemeyer,and Weyer, Z. Physik, **A279**, 399(1976).

[10] E. Hallin, *et al*, E.L. Hallin, *et al.* Phys. Rev. C, **48** 1497(1993)

[11] Barbiellini, G, *et al.* , Physical Review, **174**, 1665(1968).

[12] S.L.Glashow, *Physica* **A96**, 27(1979).

[13] Metcalf, Walker, Nuclear Physics, **B76**, 253(1974).

[14] Omelaenko, Sorokin, Sov. J. Nuc. Phys., **38**, 398(1983).

[15] Crawford and Morton, Nuclear Physics, **B211**, 1(1983).

[16] Tanabe, Ohta, Physical Review, **C31**, 1876(1985).

[17] Yang, J. of Phys., **G11**, L205(1985).

[18] Davison, Mukhopadhyay, Wittman, Physical Review Letter, **56**, 804(1986).

[19] Cenni, Dillon, Christillin, Nuovo Cim., **97A**, 1(1987).

[20] Li, Physical Review D, **D37**, 1226(1988).

[21] Laget, Nuclear Physics, **A481** , 765(1988).

[22] Davison, Mukhopadhyay, Physical Review , **D42**, 20(1990).

[23] Nozawa, Blankleider, Lee, Nuclear Physics, **A513**, 459(1990).

[24] Davison, Mukhopadhyay, Wittman, Physical Review, **D43**, 71(1991).

[25] R. Arutyunian *et al*, Phy. Rev. Lett. **4**, 3, (1963).

[26] R. H. Milburn, Phy. Rev. Lett. **10**, 75, (1963).

[27] C.E. Thorn *et al*, Nucl. Inst. Meth. **A285**, 447, (1989).

[28] A. Sandorfi,*et al*, BNL Report, BNL-32717

[29] R. D. Evans , The Atomic Nucleus, pp 677-682

[30] O. Klein *et al.*, Z. Physik, **52**, 853, (1928).

[31] LEGS collaboration, G.S. Blanpied *et al*, Physics Review Letter **67**, 1206(1991).

[32] W.K. Mize, Ph.D thesis, University of South Carolina(1992).

[33] National Synchrotron Light Source Annual Report, (1992)

[34] D. H. Dowell, *et al*, Nucl. Inst. Meth., **A286** 183(1990)

[35] W. R. Leo, *Techniques for Nuclear and Particle Physics Experiments*, Sec. 7.3

[36] A. Sandorfi, to be published

[37] H. Frauenfelder, E. M. Henley, *Subatomic Physics*, pp 37

[38] A. I. L'vov Sov. J. Nucl. Phys. **34**, 597(1981).

[39] M. Benmerrouche, N. C. Mukhopadhyay, Physical Review D, **46**, 101(1992).

[40] W. Pfeil, H. Rollnik, S. Stankowski, Nuclear Physics **B73**, 166(1974).

[41] Ishii, T. *et al.* Nuclear Physics **B165**, 189(1980).

[42] A. M. Sandorfi, *et al.* Proceedings of PANIC-XIII, Perugia, Italy

[43] Bicron Corp., 12345 Kinsman Road, Newbury, Ohio, 44065, USA

Vita

Xi-jun Zhao was born on September 1, 1963, in Guiyang, People's Republic of China. In 1984, he received his Bachelor of Engineering degree in Power Mechanical Engineering from Xi-an Jiaotong University in Xi-an, People's Republic of China. He worked in the Institute of Agricultural Mechanization in Guiyang from 1984 to 1988, doing research on renewable fuels. In the fall of 1988, he entered Virginia Polytechnic Institute and State University and received his M.S. degree in physics in December, 1990. He has been a research assistant and working on polarized photon nucleon scattering at LEGS, Brookhaven National Laboratory from June, 1990. He received his Ph.D. degree in physics from Virginia Polytechnic Institute and State University in December, 1993.